

Thermographical analysis of interface heat transfer mechanisms, with high temporal resolution

Pedro Daniel Fernandes Pontes

Thesis to obtain the Master of Science Degree in
Mechanical Engineering

Supervisors: Prof. Antonio Luís Nobre Moreira
Dr. Ana Sofia Oliveira Henriques Moita

Examination Committee

Chairperson: Prof. Viriato Sérgio de Almeida Semião
Supervisor: Dr. Ana Sofia Oliveira Henriques Moita
Member of the Committe: Prof. Edgar Caetano Fernandes

November 2016

Acknowledgments

First would like to thank IST for being my home and teaching me everything I needed to get this far. It has been truly amazing studying here and knowing so many inspiring teachers and so many brilliant colleagues.

A huge thank you goes to my supervisor and teacher Doctor Ana Moita, for introducing me to the experimental world as well as all the patience, support and time that she put into my work. I'd also like to thank Emanuele Teodori for answering to all my questions and guiding me through every decision, even when far away. I'd also like to thank my professor and co-supervisor Doctor António Moreira for having me in his laboratory team.

A big acknowledgment goes also to my laboratory mates who helped me in countless occasions and kept me motivated. I'd like to give a special thank you to all the boiling team that gave great input into my work.

I'd like to give a special thank you to Henrique Carvalho, for being my electronics consultant and Vasco Rodrigues for the mechanical piece he made for me. Without them this thesis would be a lot harder. To all my other friends that helped me and motivated me I'd also like to say thank you.

This work couldn't also be done without workshop professor Manuel Venes and his colleague welding professor, for helping me welding the blackbody. For the device's box I need to thank my good friend Paulo Belga. Also, for all the support and help, I need to thank João and Pedro from LTO.

Finally for the constant patience and support, I'd like to thank my family. And last but not least I'd like to thank my girlfriend, Tânia for keeping me company during my writing sessions but mostly for all the love and support.

Abstract

Interfacial heat transfer problems are present in various practical situations, including cooling applications. The accurate description of the observed phenomena, required to improve interfacial heat transfer requires accurate diagnostic techniques with high temporal and spatial resolution.

Time resolved Thermography has shown high potential to be used but requires a proper camera calibration. Care must be also taken in the post-processing procedure.

The present work explores time resolved infrared thermography, combined with high-speed imaging to describe the interface heat phenomena occurring during droplet impacts on heated surfaces, addressing the effect of different parameters such as wettability, impact velocity and liquid properties (surface tension). To comply with the demanded resolution a calibration was designed to improve the camera's precision. Several data processing techniques were also applied to extract the results and improve their quality.

Infrared thermography has allowed identifying and describing in detail particular phenomena reported in the literature. The proposed calibration improved the complaisance of the results with the expected heat transfer events. The results show that higher impact velocity, good wettability and low surface tension increase the heat flux between the surface and the impacting droplet. This was also related with the wetted area. The heat flux and cooling effectiveness calculated showed satisfactory values in accordance to the results previously reported in the literature.

Keywords

Infrared Thermography, Droplet Impact, Wettability, High-speed Imaging, Interfacial Phenomena, Heat Transfer.

Resumo

Podemos encontrar, em várias aplicações práticas incluindo o arrefecimento, problemas de transferência de calor. É necessário uma caracterização precisa dos fenómenos observados para se melhorar a transferência de calor em interfaces, que requer técnicas de diagnóstico com elevada resolução temporal e espacial.

A Termografia tem mostrado um grande potencial, mas necessita de uma calibração decente. Deve-se também dar especial atenção aos procedimentos de pós-processamento.

O trabalho aqui apresentado explora a combinação entre termografia de infravermelhos com elevada resolução temporal e imagiologia de alta velocidade para descrever os fenómenos de transferência de calor que ocorrem na interface durante impactos de gotas em superfícies aquecidas, analisando o efeito de diferentes parâmetros como a molhabilidade, velocidade de impacto e as propriedades dos líquidos (tensão superficial). Para satisfazer a necessidade de uma boa resolução, uma técnica de calibração foi desenhada para melhorar a precisão da câmara. Várias técnicas de pós-processamento foram também usadas para extrair resultados e melhorar a sua qualidade.

A Termografia de Infravermelhos permitiu identificar e descrever em detalhe acontecimentos particulares que foram mencionados na literatura. A calibração proposta melhorou a complacência dos resultados extraído com os fenómenos de transferência de calor. Os resultados mostram que elevada velocidade de impacto, boa molhabilidade e baixa tensão superficial aumentam o fluxo de calor entre a superfície e a gota. Estas conclusões foram também relacionadas com a área molhada pela gota. O fluxo de calor e a eficácia de arrefecimento calculados mostram resultados que estão de acordo com o esperado na literatura.

Palavras Chave

Termografia de Infra Vermelhos, Impacto de Gotas, Molhabilidade, Câmara de Alta Velocidade, Transferência de calor na Interface

Contents

1	Introduction	1
1.1	Motivation	1
1.2	State of The Art	2
1.2.1	Infrared Thermography Techniques	2
1.2.2	Numerical Studies	5
1.3	Objectives	6
1.4	Thesis Outline	6
2	Theoretical Background	7
2.1	Infrared Thermography	7
2.1.1	Radiation Intensity to Temperature Conversion	7
2.1.1.A	Blackbody Equations	7
2.1.1.B	Atmosphere Attenuation	8
2.1.1.C	Total Radiation	9
2.2	Wettability	10
2.3	Droplet Impact	11
2.4	Heat Transfer	12
3	Experimental Setups	17
3.1	Introduction	17
3.2	The Infrared (IR) Camera	17
3.2.1	Camera properties	18
3.2.2	The Software	18
3.2.2.A	Selecting a Calibration Pack	18
3.2.2.B	Main Window	19
3.2.2.C	Offset Calibration	20
3.3	Experimental set up to obtain profile views of the droplet	21
3.3.1	Procedure	21
3.4	Bottom View of the metal foil	22
3.5	Surface preparation and Characterization	24

4 Calibration and Data Processing Methods	25
4.1 Blackbody Calibration Sources	25
4.1.1 Design details	27
4.1.2 Building Process	28
4.2 Calibration process	29
4.2.1 Software Calibration	33
4.2.2 Proposed Calibration	35
4.2.3 Calibration Process Details	35
4.3 Data Processing Methods	38
4.3.1 Patterned Noise	38
4.3.2 Median Filter	39
4.3.3 Background Filter	39
4.3.4 Heat Flux computation	40
5 Experimental Results	41
5.1 Indroduction	41
5.2 Side View	41
5.3 Bottom View	42
5.3.1 Result of applying the custom made calibration method	43
5.3.2 Simultaneous analysis of droplet dynamics and thermal processes	44
5.3.3 Influence of the impact velocity	47
5.3.4 Influence of the initial foil temperature	50
5.3.5 Effect of liquid surface tension	52
5.3.6 Effect of extreme wetting scenarios: Hydrophilic and Super-Hydrophobic surfaces	55
6 Conclusions and Future Work	61
6.1 Future Work	62
Bibliography	65
Appendix A MATLAB function: calibration.mat	A-1
Appendix B MATLAB function: pbkgremove.mat	B-1
Appendix C MATLAB function: fluxo.mat	C-1
Appendix D MATLAB function: fluxo.mat	D-1

List of Figures

1.1 Calibration of an IR Camera with polynomial fit	3
2.1 Atmospheric Windows	8
2.2 Total radiation sources scheme	10
2.3 Tension Balance	10
2.4 Wetting Regimes	11
2.5 Contact Angle approaches: (a) Wenzel, (b) Cassie-Baxter	11
2.6 Droplet impact stages, for an hydrophilic surface	13
2.7 Droplet impact stages, for an hydrophobic surface	13
2.8 Heat Flux at the surface for different timesteps	13
2.9 Evolution of the calculated cooling effectiveness during the impact of a droplet on a surface initially at 120°C	15
2.10 Scheme of the surface temperature variation along the droplet radius, during spreading	16
3.1 Xenics' Onca-MWIR-InSb	17
3.2 Xeneth: Connection Setup Menu	18
3.3 Xeneth: Main Window Scheme	19
3.4 Xeneth: Selection Panel	20
3.5 Offset Calibration: Before and After	20
3.6 Silicon Wafer setup: (1) Thermocouple, (2) Silicon Wafer	21
3.7 Horizontal setup: (1) Needle, (2) IR Camera, (3) HS Camera, (4) Heated Surface, (5) Lamp, (6) Black Background	22
3.8 Bottom Setup Scheme	23
3.9 Stainless Steel Support: (1) Before calibration setup, (2) After calibration setup	23
3.10 Bottom Setup: (1) Power Source, (2) HS Camera, (3) IR Camera, (4) Needle, (5) Foil Support, (6) Harvard Apparatus	24
4.1 Pratical Cavity Blackbody Source scheme	26
4.2 Cavity and light trapping effect scheme	27
4.3 Final design scheme for the Blackbody Calibration Source	28
4.4 SolidWorks render of a cut device view	29
4.5 Thermal Resistance used	29

4.6 Thermocouple placement scheme	30
4.7 PENA30FR Adhesive Insulation	30
4.8 Completed Blackbody	31
4.9 Completed Blackbody Calibration Source: (1) Blackbody cavity; (2) Data Aquisition Board; (3) PID controller; (4) IR Camera; (5) Thermocouples (one connected to the PID, the others to the Data Aquisition Board)	31
4.10 Calibration Instalation in Function	32
4.11 Blackbody thermal image and its respective histogram	32
4.12 Calibration example: initial temperature field, and uniform temperature field (after ≈ 5 min)	33
4.13 Xeneth's software - Temperature Calibration (Plank)	33
4.14 Complete Temperature Calibration (Plank)	34
4.15 Comparison of the two calibrations at $it=450\mu s$	36
4.16 Comparison of the two calibrations at $it=450\mu s$	37
4.17 The effect of the filter in both the image and a line of point temperature values	38
4.18 Median filter effect	39
4.19 Background filter effect	39
 5.1 Side view of the water droplets impacting the hydrophilic foil at 2 m/s: spreading and receding phases	41
5.2 Side view Results for 60°C during the spreading and receding phases	42
5.3 Example of the results representation	42
5.4 Repeatability of the experiments	43
5.5 Comparison between results with and without the proposed calibration	44
5.6 Comparison between High Speed camera images and Infra Red images for 0.8m/s and 80°C at 0, 2, 6, 12 and 22 ms after the first contact on a hydrophilic surface	45
5.7 Heat Flux along the radius of a water droplet, $u_i = 2m/s$, Surface temperature=100°C . .	46
5.8 Cooling effectiveness along t^* for a water droplet impacting on an hydrophilic surface .	47
5.9 Comparison of droplet impact at 0.8m/s and 2m/s. The water droplet impacts the surface at an initial temperature of 100°C	47
5.10 Comparison between the spreading factor of each velocity	48
5.11 Average temperature along the radius between the 5 experiments of both velocity values at 100°C	48
5.12 Comparison of the heat flux computed for different impact velocities. The water droplets impact the surface which is at an initial temperature of 120°C	49
5.13 Computed cooling effectiveness comparison between two different impact velocity values for the initial foil temperature of 120°C	50
5.14 Average adimensional temperature along the radius for 4 different initial temperatures at 0.8 m/s	51

5.15 Cooling effectiveness for various initial foil temperatures with an impact speed of 0.8 m/s	52
5.16 Cooling effectiveness for various initial foil temperatures with an impact speed of 2 m/s .	52
5.17 Spreading Factor along time for a water and ethanol droplet with an impact velocity of 0.8 m/s at $\Delta T = 20^{\circ}C$ from saturation	53
5.18 High speed images for a water and ethanol droplet impact at the velocity of 0.8 m/s . . .	53
5.19 Average temperature along the radius for Ethanol and Water for a droplet impacting at 0.8m/s on a foil initially with $\Delta T = 20^{\circ}C$ under saturation	54
5.20 Heat Flux along the radius for Ethanol and Water for a droplet impacting at 0.8m/s on a foil initially with $\Delta T = 20^{\circ}C$ under saturation	55
5.21 Cooling Effectiveness comparison between water and ethanol for a droplet impacting at 0.8m/s on a foil initially with $\Delta T = 20^{\circ}C$ under saturation	56
5.22 HS Images for Hydrophilic and Super-Hydrophobic surfaces droplet impact at 0.8 m/s impact speed	56
5.23 Spreading Factor along the radius for an Hydrophilic and Super-Hydrophobic	57
5.24 Temperature along the radius for Ethanol and Water	57
5.25 IR Images for a Super-Hydrophobic surface droplet impact at 0.8 m/s impact speed (foil initial temperature at 100°C)	59
5.26 IR Images for a Super-Hydrophobic surface droplet impact at 0.8 m/s impact speed (foil initial temperature at 100°C)	59
5.27 Heat Flux comparison along the radius for a droplet impact in surfaces with different wettability	60
5.28 Cooling Effectiveness comparison along the radius for a droplet impact in surfaces with different wettability	60

List of Tables

3.1 Camera Properties	18
3.2 Thermophysical Properties of the Studied Liquids	22
4.1 Calibration Results	36

Abbreviations

IR	Infra-red
PIV	Particle Image Velocimetry
PID	Potential-Integrative-Derivative
MW	Mid Wavelength
LW	Low Wavelength
MWIR	Mid Wavelength Infrared
ADU	Analog to Digital Units
fps	Frames per second

List of Symbols

Roman symbols

W	Radiated Energy	W/m^2
T	Temperature	K
A	Area	m^2
R_f	Relation between the surface area and its flat projected area	-
f	Fraction	-
t	Time	s
r	Radius of the droplet	m
u	Velocity	m/s
k	Conductivity	$W/(mK)$
q''	Heat Flux	W/m^2
c_p	Thermal capacity	$J/(kgK)$
P	Power	W
Q	Heat Energy	J
m	Mass	kg
$avTemp$	Average Temperature	$^\circ C$
vid	Pixel/Frames video matrix	kg
x	Cartesian coordinate	m
y	Cartesian coordinate	m

Greek symbols

α	Absorptivity	-
ρ	Reflectivity	-
τ	Transmissivity	-
ε	Emissivity	-
λ	Wavelength	m
δ	Thickness of the foil	m
ϵ	Cooling Effectiveness	-
σ_{SB}	Stefan-Boltzmann constant	$5.67 \times 10^{-8} W/(m^2 K^4)$
θ	Contact Angle	degree
σ	Surface Tension	N/m
ϕ	Cylindrical coordinate	degree
β	Spreading Factor	-

1 | Introduction

1.1 Motivation

Heat transfer in fluid-solid interfaces, with fluid phase change is a common phenomenon observed in the nature and relevant for a wide number of industrial applications, namely in cooling systems, based for instance in droplet/spray impact, or pool boiling. The heat transfer mechanisms occurring in such applications are complex and there are still several processes which remain unexplained, despite the numerous studies that have been reported in the literature.

The accurate description of such phenomena requires the use of diagnostic techniques with high spatial and temporal resolution as they occur in characteristic spatial scales which can be of the order of the micrometers and temporal scales of the order of milliseconds. Within this scope, several diagnostic techniques have been explored although many of them are intrusive and do not comply with the required spatial and temporal resolutions. For instance, the use of a thermocouples is a really common method, but is intrusive to the measured process, can only measure the surface temperature at one specific location (one point) and cannot be in contact with electrically conductive means. With this in mind, infra-red (IR) thermography has been recently explored as a high potential alternative to some of the existing intrusive temperature measuring methods. A thermographic camera with a proper calibration can give high precision temperature results at high frame rates, which can provide high definition qualitatively and, more importantly, quantitatively accurate thermal images. The IR camera also outputs two dimensional images, a great advantage when trying to understand this kinds of processes, which are usually not restricted to a one dimensional analysis.

However, care must be taken when developing the calibration process and post-processing procedures, as there are many issues that must be considered, related to the dependence of the read temperature values with many parameters (e.g. ambient temperature, effect of the surroundings, surface emissivity, among others). Hence, custom made calibration and post-processing procedures must be developed and explored, to infer, based on a critical analysis, on the accuracy of the provided information and how useful it is to determine additional important features such as accurate temperature distributions, heat fluxes or cooling effectiveness.

In this context, the present work explores the use of time resolved infrared thermography to describe the heat transfer processes occurring at droplet impacts onto thin metal foils. Although the IR

camera use will be centered in the boiling process, the heat transfer mechanisms in droplet surface impact will also be studied.

While this work was being developed, a complementary computational study is being performed by Emanuele Teodori, so the results produced in the present work will also be used to validate the computational model that is being devised.

1.2 State of The Art

1.2.1 Infrared Thermography Techniques

Starting by its discovery, infrared radiation was first reported by Hershel's famous experiment with a prism that would decompose the solar light. Frederick William Hershel noticed that when he placed a thermometer outside the visible spectrum, its temperature would still increase and deducted the existence of invisible radiation. The first patent of a radiation based thermometer was emitted in the end of the 19th century [8]. Only after World War II a single point laser thermometer used in medicine, started being commercialized. Thermal cameras started being developed after the second World War, mainly for military purposes. A few years later IR systems would be used in various types of supersonic wind tunnels to detect aerodynamic heating.

In 1969, Czysz and Dixon [6] proposed a thermographic method to gather quantitative results. They applied a Phosphors coating to the surface. This coating is very sensitive to temperature. They placed heat sensors in key spots. The next step would be to use an Isodensitracer, a device that would read the density of the coating, make a density map (with iso-lines) and attribute a measured heat flux to each density level. They concluded stating that the key to gathering good quantitative results was to perform a good calibration.

Inspired by Czysz and Dixon's work, in 1998, Sargent *et al.* [21] followed the same approach and decided to use an IR camera to measure heat transfer in complex flows. Their calibration consisted in placing several thermocouples in their target surface. This calibration is often called *in situ* calibration, for being made in the measured body. After collecting the video tape from the camera and post-processing it in the computer these authors correlated the grey scale values of the image with the temperatures measured by the sensors. The result can be seen in Figure 1.1. This figure also shows the fitting curves, usually polynomials of second and third order. Czysz and Dixon [6] concluded that IR Cameras had a strong potential to be used in fluid dynamics measurements. They also concluded that *in situ* calibrations can be very useful as they eliminate the need to calculate emissivity.

In 2003, Schwabe *et al.* [22] pioneered the study of interfacial phenomena with an IR Camera. The experiments consisted on a cold surface where water would condensate, then flow back into a gap through a channel, where it would evaporate again. This was a closed cycle, covered by heated walls

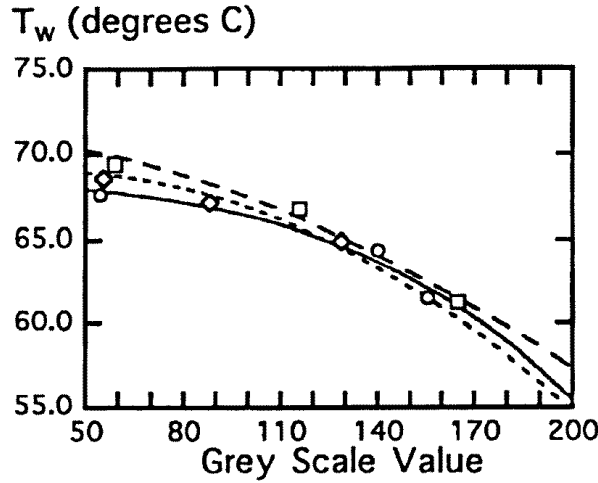


Figure 1.1: Calibration of an IR Camera with polynomial fit

Source: Sargent, 1998 [21]

and a window made of Zinc Sulfide, a material transparent to IR radiation. To avoid condensation on the glass, a heater was placed on its center. However, this heater was a big obstruction to the camera's top view.

In 2008, Shen *et al.* [23] studied simultaneous droplet impact and its influence on heat transfer from different heated surfaces. The used technique consisted in placing a high-speed camera horizontally to the droplet impact area and a infrared camera bellow the studied surface. They addressed the influence of surface topography on the heat transfer processes and observed that nano-structured surfaces had a significant lower heat removal by the droplets, when compared to smooth surfaces. It was also observed that the spreading diameter would increase with the surface heating for the nano-structured surface, while evaporation time was reduced.

In 2008, Gerardi *et al.* [10] started using thermographic cameras to study heat transfer through the macro- and micro-layer boiling applications. They wanted to observe bubble formation and study heat transfer in the interface between the bubble and the heated surface. Bubble formation is a phenomena that occurs between a small time window. To achieve this a IR Camera with high temporal resolution was used alongside with a high speed camera. The bubble formation was observed from the bottom of the experimental setup. This could only be done with a dichroic beamsplitter, that transmits IR radiation to the IR camera and is transparent to the visible light. To allow the radiation to pass from the bubble, the heated surface had to be transparent to both visible and infrared spectra, so it was made of sapphire. The sapphire thin plate had also a deposited film so it could be heated by Joule effect. With this setup it was possible to observe heat removal from a bubble from a constant heat flux source as it departs, with elevated time precision. The fact that Gerardi *et al.* [10] were able to synchronize the frames of both the IR and the high speed cameras enabled them to put side by side the images of both cameras. Correspondence of temperature maps and the phases of bubble departure was made so that thermal and physical phenomena could be matched.

In 2009, Tartarini *et al.* [26] crossed the study of droplet cooling with infrared thermography. While previous studies focused mainly on stable isothermal conditions, Tartarini *et al.* decided to focus on the study of transient conditions. To do this, the authors chose to use a IR transparent slab, heated by two radiators. Again, the IR camera would be put under the droplet, that would collect data, which would be processed in MATLAB to remove noise and apply an emissivity map. Tartarini *et al.* coated the surface with a high emissivity paint on its upper side. This procedure aimed at minimizing errors associated to emissivity and study more accurately the solid-fluid interface. The experimental data allowed these authors validating a numerical model to predict transient temperatures. It was also possible to observe temperature drop at the center of the droplet using a time-frame of a minute.

In 2010, Girard *et al.* [11] used thermography in order to study droplet evaporation. In this experiment, like the one of Tartarini *et al.* made, the author used an elevated time-frame, but with a more fine temporal resolution. In this setup a droplet fell on a heated copper surface. The IR camera was placed on top of the droplet on this setup. The authors observed the evaporation time using different surface temperatures. They focused on the interface between the water droplet and copper surface that due to their different emissivity was pretty noticeable. Based on this, Girard *et. al.* reported the interface temperature and droplet radius along the time.

In 2011, Kim and Buongiorno [15] proceeded with the work started in 2008 by Gerardi *et al.* and used thermography to detect the triple interface between solid-liquid-vapour in pool boiling with a similar setup. To detect this interface they used an optical silicon wafer (transparent to IR) in contrast with [10] which used coated sapphire. The camera detected the bubbles as dark spots and the liquid as bright spots. In this work the different absorptivity and temperatures of the distinct phases were used to detect the triple contact-line. Kim and Buongiorno observed the formation of a microlayer, where the radiation from the vapor would cross the water, and an area where the radiation would come from the bubble. The frontier between was concluded to be the limit between these 2 regions.

In 2013 Duan *et al.* [9] synchronized not only the high-speed camera with the IR camera, but also used Particle Image Velocimetry (PIV) data. The objective was studying bubble formation and departure in pool boiling. The approach to use the IR camera was similar to [10] but the high speed camera was placed horizontally to the boiling cell. Glass windows were mounted all around the wall to enable side view. The PIV laser was placed in the window frontal to the high speed camera's window. These authors could observe a dependence of the interval between bubble departure and formation with temperature, a strong cooling underneath the bubble, due to the microlayer. The observation of micro scale phenomena was only possible only by combining the high-speed camera, the IR camera and PIV.

More recently (2014), Sielaf [24] used a different technique to gather interface data from pool boil-

ing. Sielaf used a thin stainless steel foil under a heater. Given the small thickness of the foil, the interface temperature on top of the foil would be very close to that of the bottom surface. Sielaf also used a calibration technique close to the *in situ* approach. With a thermocouple inside is pool boiling cell, near the foil and with the very close assumption that the foil would be at the same temperature, each pixel was calibrated for that temperature. Additional noise filters were applied in the post processing. As many of previously mentioned authors, Sielaf used the high-speed camera horizontally to his boiling cell. Another characteristic of his technique was that the foils enabled him to identify the transition from the contact line to a microlayer. Sielaf identified that this transition occurs during the receding phase of the bubble.

Additional studies using a thin foil have been performed in the past year. For instance, in 2015 Zupancic *et al.* used this approach while also applying different coatings to study different wettability regimes. In this study, the heating of the foil is made directly by Joule effect with copper contacts on the foil. In 2016 Petkovsek *et al.* observed, with a similar setup the hot spot phenomena. In this hot spot, measured temperature would be higher than the surroundings.

1.2.2 Numerical Studies

In this section some relevant numerical work about heat transfer in droplet impact will be discussed. This work contributed aswell to better understanding droplet related phenomena and heat transfer.

Numerous numerical droplet simulations have been performed in the last century, but the assumptions made to simplify them were questioned by several authors such as Healy *et al.* [13] in 2001. Heat transfer during the spreading phase had been neglected, for representing a small fraction of the evaporation time. Although it seems a reasonable assumption, Healy *et al.* found that in the spreading phase, the droplet temperature raise caused an alteration of its properties which resulted in significant errors. Still in 2001, Pasandideh-Fard *et al.* [19] tested a numerical model that studied heat extraction, comparing it between impact velocities. Besides validating the model, impact velocity had a weak effect on the calculated temperature variation and heat flux. The principal effect of the increase of this parameter is that more area is wetted which means that extracts heat from a greater area. Later in 2010, Strotos *et al.* [25] was able to identify, in his numerical work, various phenomena such as the bubble trapping effect and the neck in the droplet's lamela, and the heat transfer effects that these phenomena cause. In the case of the bubble trapping effect, an increase of the temperature in the droplet center, in the first moments after the impact was noted. In the case of the lamela neck a relation was made between its formation and position and an increase of temperature in that area.

1.3 Objectives

The main objective of this work is to explore the potential of the use of an high speed infrared camera to study in detail the heat transfer processes occurring at liquid-solid interfaces.

Here, the proper calibration and post-processing procedures must be developed and tested on a case study. Which was chosen to be the impact of droplets onto heated thin foil surfaces.

The IR images are analyzed together with high speed images, to relate droplet dynamics with heat transfer processes.

The calibration and post-processing procedures developed are evaluated based on a critical analysis to infer on how good the data collected by the IR camera can be used to describe in detail the phenomena reported in the literature and provide complementary information on the temperature distributions, heat flux and cooling effectiveness. Finally, the validated data is also used to explore the physics governing the observed phenomena and discuss the effect of droplet impact velocity, wettability, liquid surface tension and temperature.

The heat transfer processes occur at single phase and when the liquid droplet is boiling.

1.4 Thesis Outline

The present dissertation is organized in 6 main chapters including this introductory section that provides the motivation of the work, a state of art to contextualize the work and the main objectives to achieve.

The main concepts and theoretical background required to better understand the procedures developed in Chapter 4 and the results discussed in Chapter 5 are presented in Chapter 2.

Chapter 3 describes the experimental setups and measured procedures followed. The functioning of the IR camera and the software calibration methods are discussed here.

One of the most important parts of the work is the calibration and post process methods that are proposed in the work. These methods are explained in detail in Chapter 4, against the methods available in the camera software.

The results are presented and discussed in chapter 5.

Finally, chapter 6 draws the main conclusions and provides several recommendations to be considered in future work.

2 | Theoretical Background

2.1 Infrared Thermography

Heat transfer through radiation is the way, in thermography, most often used to gather quantitative information on surface temperature. One of the main objectives of this work is to correctly convert the measured radiation intensity plus the information on the body emissivity and surrounding conditions in an accurate temperature estimate. To do so, some theoretical notions must be introduced.

2.1.1 Radiation Intensity to Temperature Conversion

Radiation is emitted by all bodies at $T > 0K$. The intensity of this radiation largely depends on the direction, wavelength and of course temperatures. For example, above $500^\circ C$, a body's radiation is almost entirely in the IR wavelength [1]. Besides emitting radiation a body can also absorb (α), reflect (ρ) and radiation can even pass through it (τ). Adding all this elements we get the Total Radiation Law:

$$W = W\alpha + W\rho + W\tau \quad (2.1)$$

in which W represents the total energy transmitted through radiation. Equation 2.1 can be simplified as:

$$1 = \alpha + \rho + \tau \quad (2.2)$$

Note that in the equation 2.2, α , ρ and τ represent the respective absorbed, reflected and transmitted fractions of the incident radiation energy, and have values between 0 and 1.

2.1.1.A Blackbody Equations

One of the most important concepts that is used in this work is the concept of *blackbody*. A *blackbody* is characterized for absorbing all energy transmitted through radiation. In the ideal case of a *blackbody* the coefficients assume the following values: $\alpha = 1$, $\rho = 0$, $\tau = 0$. The blackbody is also a perfect emitter. The emissivity (ε) of a body characterizes the efficiency of a body for emitting energy, so it's the ratio between the energy emitted and the energy emitted if the body was a *blackbody*. With this in mind one can use the equation 2.3 for a *blackbody*. This equation is called Kirchhoff Law. Kirchhoff Law is also applied for the same wavelength (λ) so one can also use equation 2.4.

$$\alpha = \varepsilon \quad (2.3)$$

$$\alpha(\lambda) = \varepsilon(\lambda) \quad (2.4)$$

For the specific case of a *blackbody* one can also apply equation 2.5. This equation is called Stefan-Boltzmann law and it states the relation between energy emitted through radiation and the temperature of the body. If the body is not perfectly black, but its absorption/reflection/transparency properties don't vary with the wavelength, it's called as *greybody* and in this case one should use Equation 2.6.

$$W = \sigma_{SB} T^4 \quad (2.5)$$

$$W = \varepsilon \sigma_{SB} T^4 \quad (2.6)$$

where $\sigma_{SB} = 5.670373 \times 10^{-8} W m^{-2} K^{-4}$ is the Stefan-Boltzmann constant.

It's fairly obvious these are concepts that illustrate ideal situations, and even though in most experiments shown further ahead the materials are chosen to be as close to *black* or *greybodies*, those aren't perfect. Of course this is attenuated by the fact that thermography measures in small intervals of wavelength. The next subsection will relate how a wavelength interval is selected, and its relation with the atmosphere.

2.1.1.B Atmosphere Attenuation

Almost every thermographical camera is separated from its target by the atmosphere, which has good or bad transmittance in different wavelengths. The atmosphere attenuation depends on the complexity of its composition. For example, each of the following molecules: H_2O , O_2 , CO_2 have certain wavelength values for which $\tau = 0$. This means that in these wavelengths IR radiation will not pass through the atmosphere and its intensity cannot be measured.

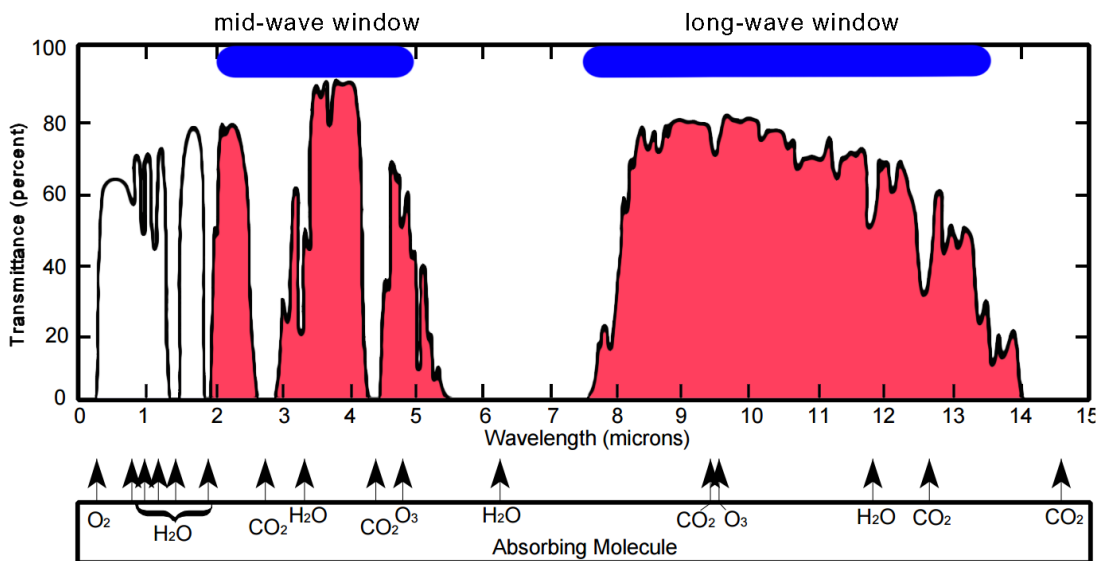


Figure 2.1: Atmospheric Windows

Source: Adaptation from chapter 7's Figure 10 of [7]

This issue calls requires of choosing a wavelength *window* for which the transmittance is close to 1. These *windows* can be seen in Figure 2.1. It is possible to identify 2 main regions: the medium-wave *window* (from 2-5 $m\mu$), or MW, and the long-wave *window* (from 7.5-13.5 $m\mu$), or LW. The used camera works in the MW range so a selective range of wavelength inside it had to be chosen to avoid "bad atmosphere transmittance".

2.1.1.C Total Radiation

When measuring a body's temperature with the IR Camera, there are other radiation sources that have to be accounted for. In total one can divide these radiation sources in 3 categories, shown below:

- The radiation emitted by the object/objects of study

$$W_{obj} = \varepsilon_{obj} \sigma_{SB} T_{obj}^4 \quad (2.7)$$

- The radiation emitted by the atmosphere (where $\varepsilon_{atm} = 1 - \tau_{atm}$ because $\rho_{atm} = 0$)

$$W_{atm} = (1 - \tau_{atm}) \sigma_{SB} T_{atm}^4 \quad (2.8)$$

- The radiation from the surroundings reflected by the object/objects.

$$W_{refl} = (1 - \varepsilon_{obj}) \sigma_{SB} T_{refl}^4 \quad (2.9)$$

where T_{refl} refers to the apparent temperature of the surroundings radiating to the measured body.

Figure 2.2 identifies these sources and their origin. Note all the expressions in the figure represent energy radiated. In it it's possible to observe that 2 sources of radiation come from the studied body and represent the emitted and reflected components. When these components cross the atmosphere, they are affected by its transmissivity, τ_{atm} (this value in common atmospheric conditions is close to 1). The atmosphere itself can emit radiation, but because τ_{atm} is so close to 1, this is mostly negligible.

With these equations it is possible to relate the radiated energy received W and the body temperature. This relation is seen in equations 2.10 and 2.11.

$$W_{tot} = W_{obj} + W_{refl} + W_{atm} = (\varepsilon_{obj} \sigma_{SB} T_{obj}^4) + ((1 - \varepsilon_{obj}) \sigma_{SB} T_{refl}^4) + ((1 - \tau_{atm}) \sigma_{SB} T_{atm}^4) \quad (2.10)$$

$$T_{obj} = \sqrt[4]{\frac{W_{tot} - (1 - \varepsilon_{obj}) \sigma_{SB} T_{refl}^4 - (1 - \tau_{atm}) \sigma_{SB} T_{atm}^4}{\sigma_{SB} \varepsilon_{obj}}} \quad (2.11)$$

The camera receives the total radiation W_{tot} , and the user has to input the emissivity and both the ambient and reflection temperatures in the camera software.

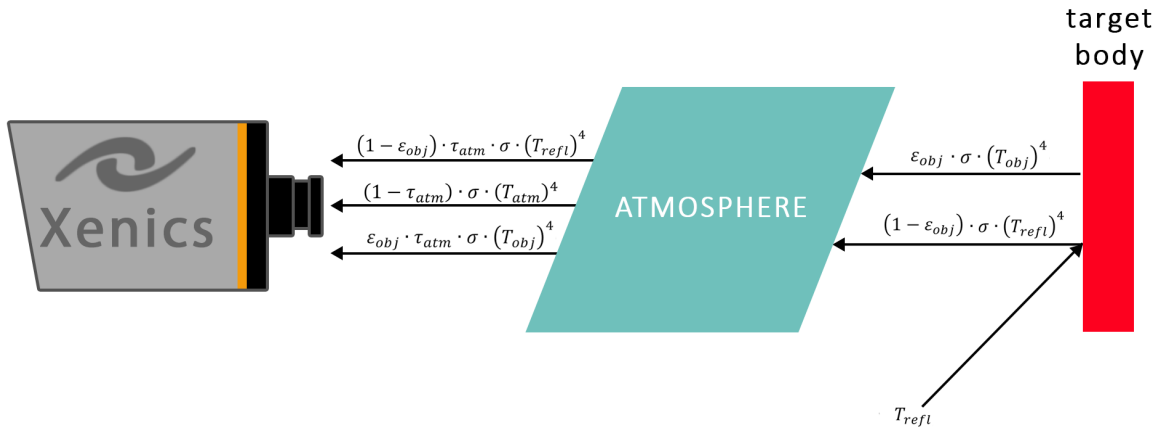


Figure 2.2: Total radiation sources scheme

2.2 Wettability

Wettability is quantified by how well the surface is wetted by a liquid. This property is often characterized based on the equilibrium contact angle of a droplet deposited on a solid surface. This angle is given by the balance of the interface tensions acting between the surface, liquid and the vapor surroundings. The balance between these tensions is represented in Figure 2.3

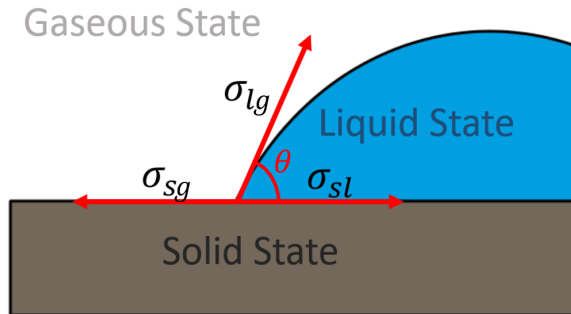


Figure 2.3: Tension Balance

From a thermodynamics perspective, the equilibrium condition of a liquid droplet are calculated by the minimization of the Gibbs energy of the system, G . When one considers constant temperature and pressure conditions it is possible to derive the well known Young's equation [28] from this minimization ($dG = 0$), which is simply the aforementioned balance of the interface tensions in the horizontal axis:

$$\sigma_{sg} = \sigma_{sl} + \sigma_{lg} \cos(\theta_e) \quad (2.12)$$

where σ represents the interface tension at the solid-liquid (sl), solid-gaseous (sg) and liquid-gaseous (lg) boundaries and θ_e represents the equilibrium contact angle. High wettability droplet-surface-surrounding systems have $0^\circ < \theta_e < 90^\circ$ and low wettability have $90^\circ < \theta_e < 180^\circ$. The perfect wetted system has $\theta = 0^\circ$ and the perfect non-wetted system has $\theta = 180^\circ$ [5]. If the liquid in study is water, the well wetted surfaces are called hydrophilic, while poor wetted surfaces are hydrophobic. Since ideal wetting/non-wetting situations do not exist, several authors (e.g. Koch *et. al.* [16]) consider

the concept of superhydrophilic in $\theta_e < 10^\circ$ and superhydrophobic surfaces $\theta_e > 150^\circ$ the latter must also depict low hysteresis. These regimes are depicted in Figure 2.4.

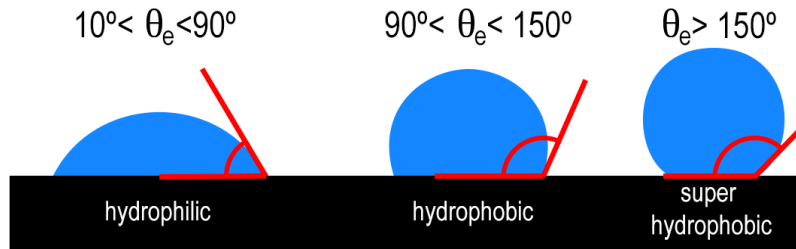


Figure 2.4: Wetting Regimes

While Young equation assumes that the surface is ideally smooth, in reality one has to take in account the roughness of the surface. Considering an rough homogeneous interface, one can convert the smooth surface contact angle (θ_e) to the actual contact angle (θ) using a formula based on the force balance and empirical correlations, presented in Equation 2.13.

$$\cos\theta = R_f \cos\theta_e \quad (2.13)$$

where $R_f = \frac{A_{SL}}{A_F}$ is the relation between the surface area, to its flat projected area. This equation is called the Wenzel equation [27]. Cassie took a different approach and considered an heterogeneous interface, where air would be trapped between the liquid and the surface, in pockets formed by the surface roughness. So having an interface with a fraction f_1 at one contact angle θ_1 and another at f_2 and θ_2 , the contact angle would be given by Cassie's Equation [4] :

$$\cos\theta = f_1 \cos\theta_1 + f_2 \cos\theta_2 \quad (2.14)$$

The difference between these two approaches can be seen in Figure 2.5

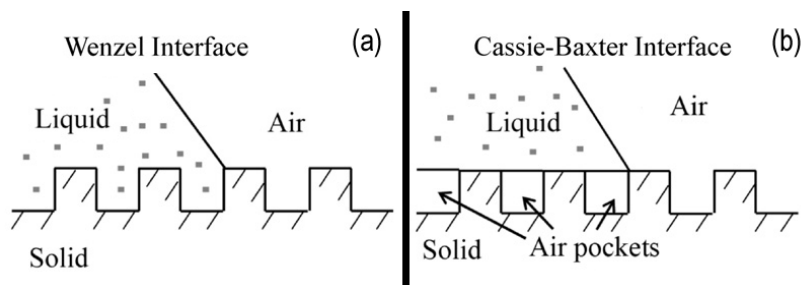


Figure 2.5: Contact Angle approaches: (a) Wenzel, (b) Cassie-Baxter

Source: Adapted from Bhushan, 2011 [3]

2.3 Droplet Impact

Several outcomes arrive from droplet impact, which depends on the impact conditions (size of the droplet and impact velocity), liquid properties and the boundary conditions established by the surface temperature and wettability:

- Rebound: after the impact the droplet bounces off the surface partially or fully. Partial rebound happens when the surface is hydrophobic, while full rebound usually requires the surface to be super-hydrophobic.
- Stick and Spread: the droplet sticks to the surface after the impact, spreading in the radial direction on the thin liquid film lamella. This is characteristic of hydrophilic surfaces.
- Disintegration: the droplet sticks to the surface but smaller droplets are released in the spreading phase. Different disintegration mechanisms can be identified depending on the wettability, surface topography and impact conditions (Moita *et. al.* [17]).

As the droplet hits the surface it deforms and spreads as a radial liquid film on the surface. The different outcomes arrive after this initial impact stage called as the kinematic phase. As the liquid film (lamella) starts to form, the spreading velocity is dictated by the velocity of the contact edge of the film that instantly forms (u_{ce}). This parameter can be related with the droplet impact velocity(u_i) and with the contact angle using 2.15.

$$u_{ce} = \frac{u_i}{\tan\theta} \quad (2.15)$$

The lamella continues to spread governed by inertial effects until reaching its maximum diameter. Afterwards the lamella starts to recoil until reaching an equilibrium state.

While the earlier stages of spreading until reaching the maximum spreading diameter are governed by inertia, at the maximum spreading and at the recoiling phases viscous dissipation and wettability gain relative importance. Hence, spreading followed by recoiling is usually observed for impacts on hydrophilic surfaces, while rebound often occurs on hydrophobic surfaces, as the wettability precludes the contact between the lamella and the surface, lessening the viscous dissipation. Consequently, at the end of the recoiling phase the excess of surface energy is high enough to promote the droplet rebond from the surfaces. These phenomena are illustrated in figures 2.6 and 2.7.

To characterize the spreading and the recoiling phases many authors usually consider the spreading ratio $\beta(f) = \frac{D(t)}{d_0}$, which provides the temporal variation of the spreading diameter made non dimensional by the initial droplet diameter [20]. The time is also often made non dimensional as:

$$t^* = \frac{tu_i}{r} \quad (2.16)$$

where r is the droplet radius at that time.

2.4 Heat Transfer

During droplet impact, the most important heat flux to evaluate is the change of heat between the droplet and the heater. According to [24], the heat flux from the droplet can be written as:

$$q'' = q_0'' + k_h \delta \left(\frac{\partial^2 T}{\partial x^2} + \frac{\partial^2 T}{\partial y^2} \right) - \rho_h c_{p,h} \delta \frac{\partial T}{\partial t} \quad [W/m^2] \quad (2.17)$$

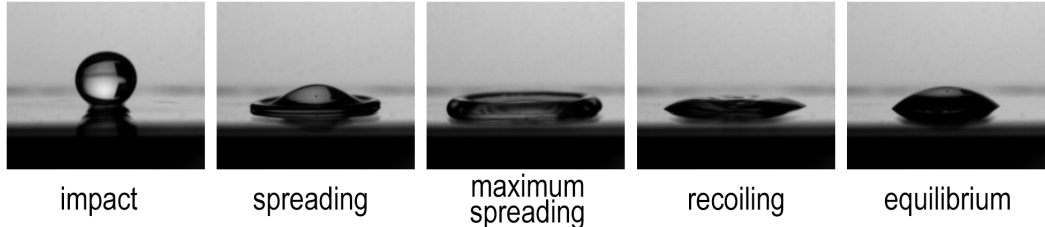


Figure 2.6: Droplet impact stages, for an hydrophilic surface

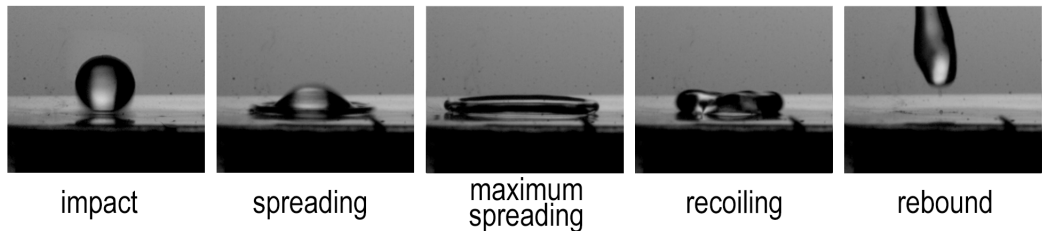


Figure 2.7: Droplet impact stages, for an hydrophobic surface

where q_0 is the heat flux from the heater, k_h , ρ_h and $c_{p,h}$ are the conductivity, density and specific heat capacity of the heater's material and δ is the thickness of the heater. Across the radius of the droplet, the heat flux curves are similar to those reported by [19] and represented in Figure 2.8. High heat transfer occurs in the first instants after impact ($t < 2$ ms). As the droplet spreads a peak in the heat flux is observed at the edge of the lamella. This is due to "new" cold liquid reaching the hot surface. The heat flux is reduced substantially in time at later stages of spreading ($t > 4$ ms), mainly because the droplet is heating and the liquid speed is decelerating, thus reducing convective and conductive heat transfer.

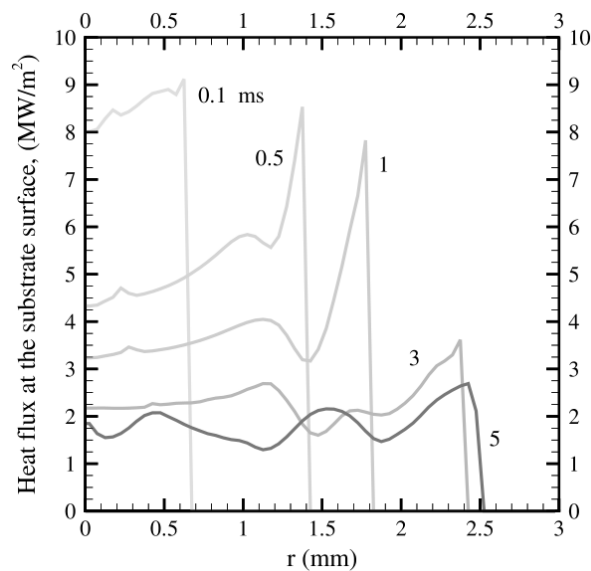


Figure 2.8: Heat Flux at the surface for different timesteps

Source: M. Pasandideh-Fard, 2001 [19]

In the droplet case, the flux for various points along the radius is being analyzed, and this calcu-

lation is made using cylindrical coordinates and considering the temperature distribution to be axysimmetrical. To convert the coordinate system, one should first consider the following transformation of the second derivative:

$$\frac{\partial^2}{\partial x^2} = (\cos\phi \frac{\partial}{\partial r} - \frac{\sin\phi}{r} \frac{\partial}{\partial\phi})(\cos\phi \frac{\partial}{\partial r} - \frac{\sin\phi}{r} \frac{\partial}{\partial\phi}) \quad (2.18)$$

$$\frac{\partial^2}{\partial y^2} = (\sin\phi \frac{\partial}{\partial r} - \frac{\cos\phi}{r} \frac{\partial}{\partial\phi})(\sin\phi \frac{\partial}{\partial r} - \frac{\cos\phi}{r} \frac{\partial}{\partial\phi}) \quad (2.19)$$

Considering now the condition of axyssimmetry ($\frac{\partial}{\partial\phi} = 0$), and applying the expression to the temperature field, one can write the sum of the second derivatives as:

$$\frac{\partial^2 T}{\partial x^2} + \frac{\partial^2 T}{\partial y^2} = (\cos^2\phi \frac{\partial^2 T}{\partial r^2}) + (\sin^2\phi \frac{\partial^2 T}{\partial r^2}) = (\cos^2\phi + \sin^2\phi) \frac{\partial^2 T}{\partial r^2} = \frac{\partial^2 T}{\partial r^2} \quad (2.20)$$

Thus, the equation for the heat flux removed by the droplet, considering the axyssimmetry condition, can be written as:

$$q'' = q_0'' + k_h \delta \left(\frac{\partial^2 T}{\partial r^2} \right) - \rho_h c_{p,h} \delta \frac{\partial T}{\partial t} \quad [W/m^2] \quad (2.21)$$

The power dissipated (P_{diss}) by the droplet is the integral of this expression in the droplet area, and it's given by:

$$P_{diss} = \int_A q'' dA \quad [W] \quad (2.22)$$

Since the droplet, ideally, is always axisymmetric, it is necessary to decompose dA in cylindrical coordinates. Equation 2.22 is expressed in cylindrical coordinates in Equation 2.23. Integrating the power in time one ends up with the total heat extracted. This is expressed in Equation 2.24.

$$P_{diss} = \int_\theta \int_r r q'' dr d\phi \quad [W] \quad (2.23)$$

$$Q_{tot} = \int_t P_{diss} dt [J] \quad (2.24)$$

Pasandideh-Fard [19] proposed a way to quantify the "cooling effectiveness" (ϵ) of the droplet. This effectiveness is described by the actual heat removed by the droplet divided by the maximum heat transfer possible be removed in theory (assuming no phase change). This coefficient is described by Equation 2.25.

$$\epsilon = \frac{\int_t \int_A q'' dA dt}{(mc_p \Delta T)_{water}} \quad (2.25)$$

The relation between the cooling effectiveness and the time adimensionalized for different impact velocities has been computed by [19] and is shown in Figure 2.9. The cooling effectiveness grows with the impact velocity because, as shown in Equation 2.16, the spreading factor is larger, meaning that the area covered by the droplet also grows.

The heat transfer occurring during droplet spreading has particular complex characteristics as described in the literature (e.g. [25]). Figure 2.10 illustrates approximately how the temperature of the

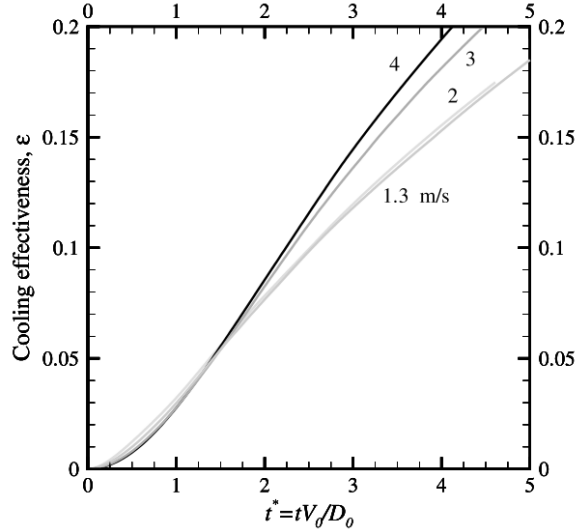


Figure 2.9: Evolution of the calculated cooling effectiveness during the impact of a droplet on a surface initially at 120°C

Source: M. Pasandideh-Fard, 2001 [19]

surface evolves along the radius during droplet spreading. In the center of the droplet a bubble trapping effect creates a barrier for heat transfer, causing the temperature to have a slightly higher value. Also in the minimum thickness area the temperature is higher because the layer of liquid is thinner, removing less heat. In the contact edge, called rim, the liquid flowing from the lamella arrives and recirculates, so the temperature decreases again in this regime. The temperature raise at the end of the droplet, after the rim is naturally due to heat conduction from the heater within a region that is no longer wetted by the fluid.

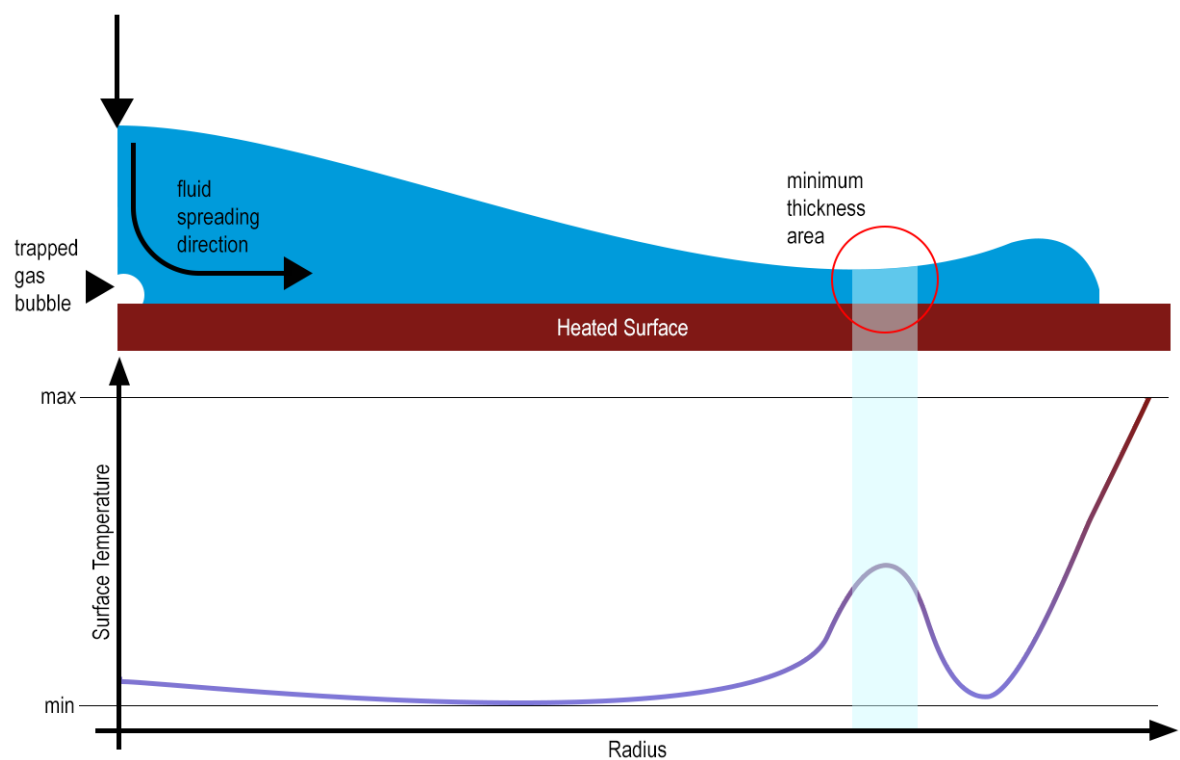


Figure 2.10: Scheme of the surface temperature variation along the droplet radius, during spreading

3 | Experimental Setups

3.1 Introduction

This Chapter describes the experimental setups used in the present work, together with the respective procedures. Two setups are used to obtain side views of the droplet (to understand its dynamics) and bottom view of the surface, to obtain temperature maps of the surface region cooled by the impact of the droplet.

3.2 The Infrared (IR) Camera

The IR Camera, an Onca-MWIR-InSb from Xenics, is the main device used in this dissertation provides "images" of the analyzed object's temperature field. Its 2D array of sensors reads the incident IR radiation. Its signal is then converted to temperature in the camera's software. The user will end up with a bi-dimensional field of temperatures with a +/- 0.5°C precision. This camera can be seen in Figure 3.1.



Figure 3.1: Xenics' Onca-MWIR-InSb

Source: <http://www.xenics.com/en/onca-mwir-insb>

3.2.1 Camera properties

The relevant properties of the Onca-MWIR-InSb can be seen in Table 3.1.

Table 3.1: Camera Properties

Camera Characteristics		Optical System		Image Characteristics	
Sensor	InSb (MWIR)	Focal lens	13 mm	Video Rate	60Hz
Spectral Sensibility	3.5-5 μ m	Optics Material	Germanium	Max framerate	3000 fps
Spatial Resolution	320 \times 256 px	-	-	Min pixels (ROI)	15 \times 5 px
Thermal Sensibility	<17mk	-	-	Exposition	>1 μ s

3.2.2 The Software

This camera has its own specific software, Xeneth, which will be very important throughout this work. It's relevant to explain its functioning, which will be referenced various times in this dissertation. The correct use of the camera also depends on an appropriate configuration of several parameters on the software which therefor are worth to be explored with more detail.

3.2.2.A Selecting a Calibration Pack

When the program is executed a menu will appear. In this menu it's possible to select not only the used camera (there is also an option to select a virtual camera, used to play previously recorded videos) but also to select a calibration pack as it is shown in Figure 3.2.

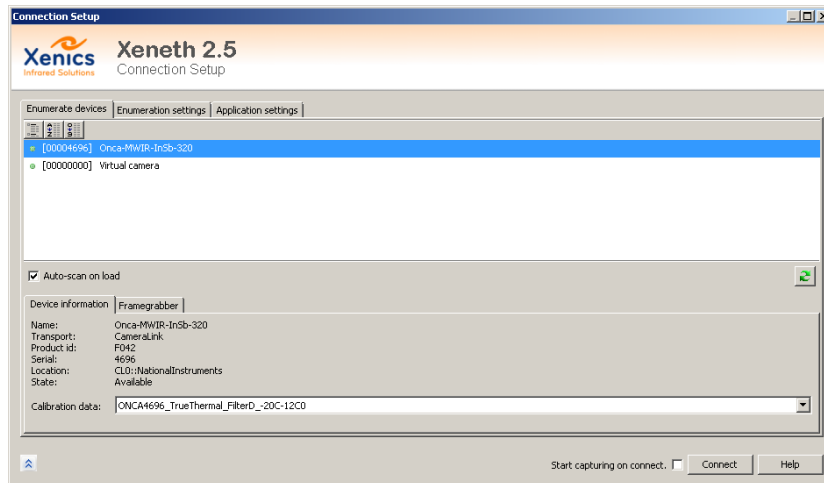


Figure 3.2: Xeneth: Connection Setup Menu

In the Calibration data drop menu are available several calibration packs. The main packs are:

- TRUE NUC: This pack is the one chosen if one wants to get data without temperature conversion. It presents results in Analogue to Digital Units (ADU) (received signal intensity) and it's adaptable to any integration time
- TRUE THERMAL: This pack comes with a calibration made by the camera manufacturer, so the results are presented in Celsius. This is used if the user just needs a low thermal resolution

measure or a qualitative result. It allows temperature measurements from -20 to 120°C in any integration time (the integration time will be described in the following subsection).

- User Calibration Packs: The user may want to create his own custom made pack adapted to his own temperature interval, to use in a more specific application.

3.2.2.B Main Window

After choosing the appropriate calibration for the desired application and before starting the measurements, one should adjust several parameters in the main software window. The displayed panels are shown in Figure 3.3. There is a panel for the Camera Image, where one can see the thermal image and select an area or dot to take its read value and other statistics; a User Interaction Panel, where one can change settings, view and set the selection properties, record and save videos and choose image filters; a panel that shows the plotted measured data. In the right side we can also see a colour bar. This bar is adjustable so that we can adapt the colour gradient to the desired temperature interval to better observe the phenomena.

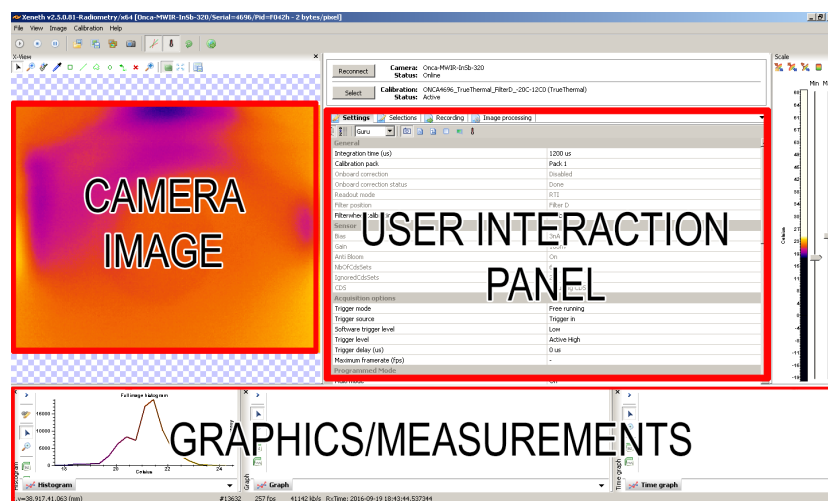


Figure 3.3: Xeneth: Main Window Scheme

Before starting there are some important settings to review to assure the best image possible. These parameters can be altered in the User Interaction Panel. The first and one of most important parameters is the integration time. The integration time can be easily explained as the equivalent to a common camera's exposure. If we increase the integration time we increase the sensitivity and reduce the noise. On the other side the image will saturate easier, which means that the temperature range highly decreases. So if a higher temperature range is needed, one should decrease the integration time until the desired range is obtained. Increasing the integration time will also decrease the acquisition rate (fps) which may not be relevant for static measurements, but the phenomena studied in this dissertation requires high temporal resolution because their characteristic time is of the order of milliseconds. The next important parameter to get is the Ambient Temperature and the Atmospheric Temperature, which can also be altered this in the User Interaction Panel. To determine the Ambient

Temperature a highly reflective object is put in front of the camera and its temperature measured considering the body to be black.

The measurements can be made using the Selection Panel, shown in Figure 3.4. In this panel it is possible to select a shape (a circle in the case presented) and gather the statistics about the temperature data, including the average temperature of the selected area both in space and time and also the standard deviation. This procedure is also used to select the area of interest. Finally the Zoom function is very important to restrict the measured area as much as it is possible to increase the acquisition rate of the camera.

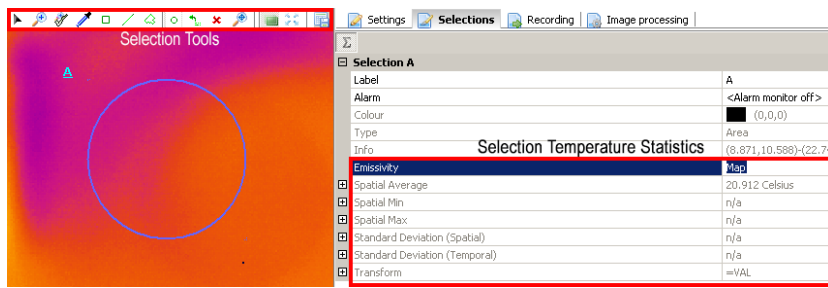


Figure 3.4: Xeneth: Selection Panel

3.2.2.C Offset Calibration

The offset calibration is required to decrease the Narcissus effect, which is basically the reflection of the lens on itself, being an error source which must be eliminated. An example of this effect is illustrated in Figure 3.5 where a blackbody with constant temperature may happen to have temperature variations (Figure 3.5.a).

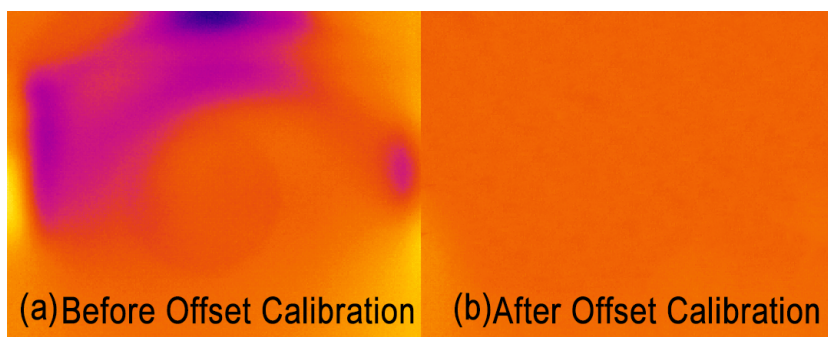


Figure 3.5: Offset Calibration: Before and After

A good way to eliminate this error is to use a software tool: the Offset Calibration. This can be found in the Calibration Wizard (a menu of calibration options for the camera) and has a simple function: it averages the temperature in space and time and sets every pixel to that temperature. This eliminates the camera's reflection and also part of the noise and bad pixels. A disadvantage of this method is that it may create lesser periodic noise, which can be a problem to the measurements. The code behind this function is unknown, so the noise source could not be detected and could only

be attenuated later in the post-processing stage. The result of the Offset Calibration can be seen in Figure 3.5.b.

3.3 Experimental set up to obtain profile views of the droplet

To create a heater, cartridge resistance heaters were put under an aluminum plate, radiating to its surface. The experiment was made for water droplets impacts on a hydrophilic silicon wafer surface

In the interface of the silicon wafer and the aluminum plate a thermal paste was used to improve heat transfer. On top of the silicon wafer there is a thermocouple that monitors the surface temperature. This setup can be seen in detail in Figure 3.6. The thermocouple value is used by a PID controller to control the heat released by the cartridge heater.

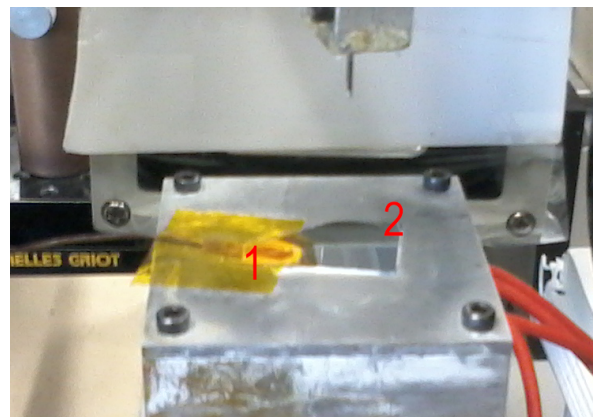


Figure 3.6: Silicon Wafer setup: (1) Thermocouple, (2) Silicon Wafer

An Harvard Apparatus controls a syringe's water discharge, that then falls from the needle to the wafer. This forms a droplet with 2.6 to 3 mm diameter spherical droplet. This experiment is recorded by 2 cameras: IR camera and high-speed camera. In order for the high-speed camera to work, a high intensity lamp is also needed. The described setting can be seen in Figure 3.7. This setting was used to gather qualitative results only. Good quantitative results are impossible due to the implications of droplet geometry in thermography. The images taken by the high speed camera were recorded at 2200 fps. The calibration factor used was 26 px/mm. The calibration factor for the IR camera was 6 px/mm.

3.3.1 Procedure

- Adjust IR Camera's settings on the software.
- Perform an offset calibration (described in Section 3.2).
- Adjust PID controller to the desired temperature and water flow in the Harvard Apparatus.
- Set the cameras recording.

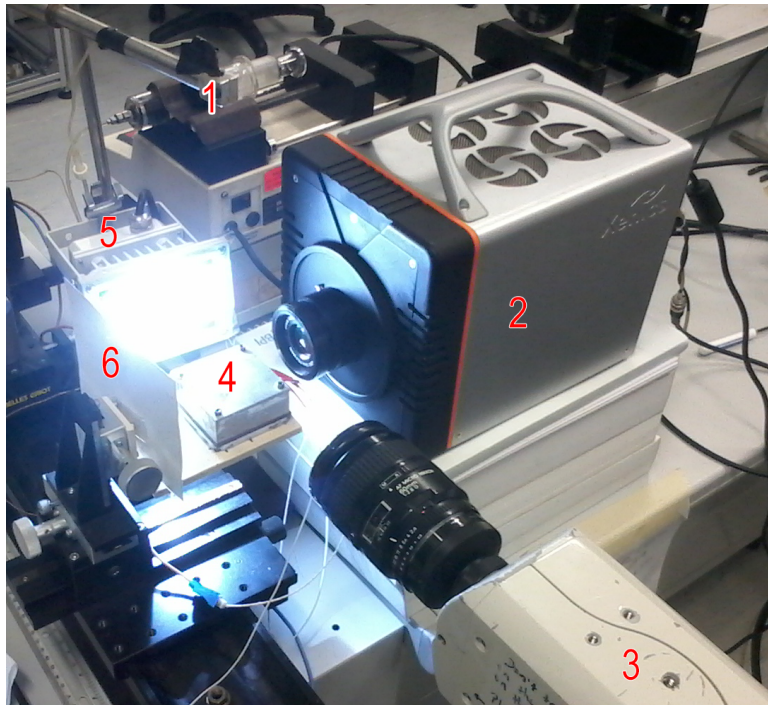


Figure 3.7: Horizontal setup: (1) Needle, (2) IR Camera, (3) HS Camera, (4) Heated Surface, (5) Lamp, (6) Black Background

- Let a droplet fall on the wafer.
- Clean the wafer with acetone and distilled water before proceeding to a new test.

3.4 Bottom View of the metal foil

In this setup, the IR Camera is placed underneath the surface on which the droplet impacts. The droplet impacts on a $20 \mu\text{m}$ thick stainless steel foil. This was done similarly to [24], as the objective was to read the interface temperatures. Due to the small thickness of the foil, the temperature of the interface is very similar to the read temperature in the bottom of the foil. The HS camera was placed horizontally to the foil to observe the impact. A lamp was placed in the opposite side. The setup scheme can be seen in Figure 3.8.

Table 3.2: Thermophysical Properties of the Studied Liquids

Characteristics	Water	Ethanol
Saturation Temperature ($T_{sat}[^{\circ}\text{C}]$)	100	78.3
Density ($\rho[\text{kg}/\text{m}^3]$)	1000	757
Kinematic Viscosity ($\mu[10^{-3} \text{Ns}/\text{m}^2]$)	1.05	1.19
Surface Tension ($\sigma[10^{-3} \text{N}/\text{m}]$)	72.88	22.8

The experiments performed using this setup were made using hydrophilic (using distilled water and ethanol) and super-hydrophobic (using just water) surfaces. A preliminary experiment with water and an hydrophilic surface was made, using the software calibration. From the first, raw results were

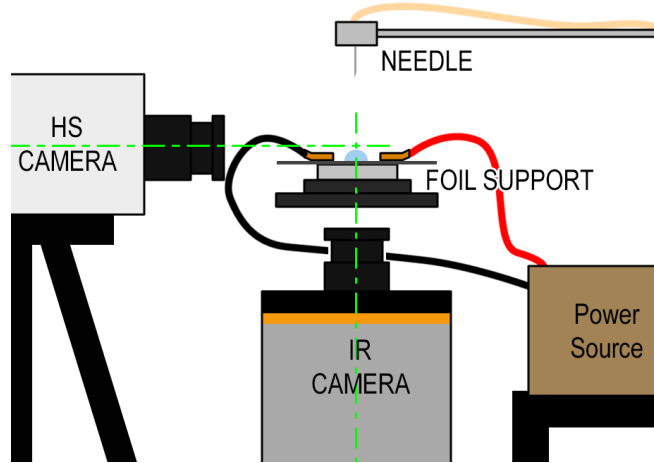


Figure 3.8: Bottom Setup Scheme

taken for posterior calibration and processing. The calibrations and their differences are explained in Chapter 4. Table 3.2 summarizes the main physical properties of the working fluids [2].

The foil is fed by an electric current, so it can heat up to the desired temperature. This is done by two electrical contacts, wired to a power source. The foil has to be placed on top of a bad heat conductor to minimize heat losses. A heat glass was chosen for the purpose. The foil must be stretched so that possible wrinkles don't affect the droplet motion. A detail of the setup, on the foil support can be seen in Figure 3.9. In this figure two supports are shown. The second was made after the calibration.

To prepare the super-hydrophobic surfaces, the surfaces needed to be cleaned with an ultra-sound bath and coated with *Glaco®* [14]. This coating took several layers to ensure effective coating that can endure high temperature and droplet impacts.

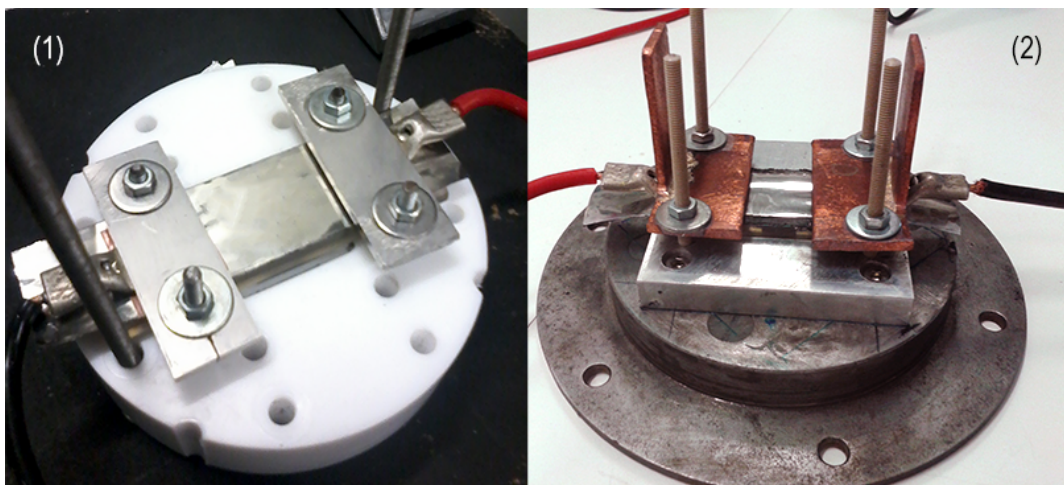


Figure 3.9: Stainless Steel Support: (1) Before calibration setup, (2) After calibration setup

This setup also was the Harvard Apparatus and the needle to generate the droplet. A metal

structure holds the support, needle and the camera. The complete setup can be seen in Figure 3.10. Although one have a different calibration, the procedure is similar to the previously described in 3.3.1. The big difference is that the foil temperature is controlled with the power source and not with the PID. To adjust the current correctly one needs to read the temperature on the IR Camera's software. In the case that raw images are needed, an additional step should be to convert the desired temperatures in ADU. Only this procedure allows knowing if the foil is at the desired temperature.

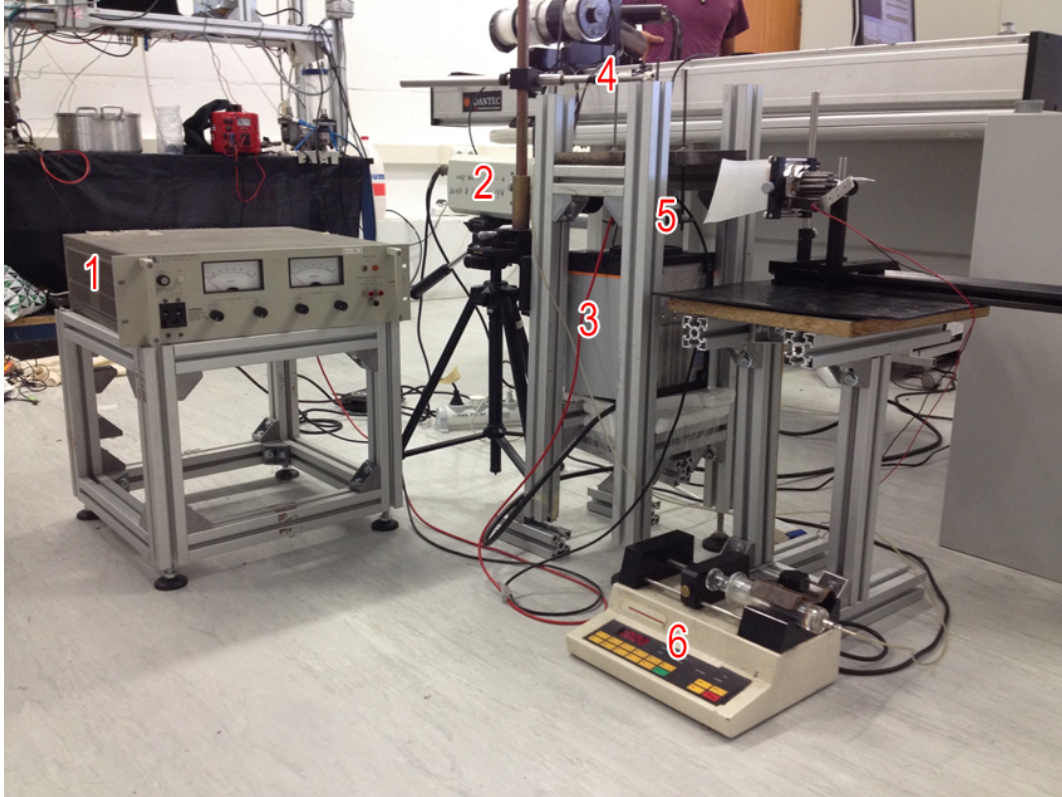


Figure 3.10: Bottom Setup: (1) Power Source, (2) HS Camera, (3) IR Camera, (4) Needle, (5) Foil Support, (6) Harvard Apparatus

3.5 Surface preparation and Characterization

The stainless steel foils (coated and uncoated) were characterized in terms of surface topography and wettability. Surface topography was measured a profile meter (Dektak 3 - Veeco) with a vertical resolution of 20 nm. The foil was found to be smooth within this resolution. The wettability was characterized measuring the contact angle with an optical profile meter (THETA from Attention) using the droplet method, as described for instance in Moita *et. al.* (2016) [18]. The contact angle values are taken as an average of 5 measurements performed at different regimes of the surfaces. The contact angle is $\theta = 87.05^\circ$ for the hydrophilic surface and $\theta = 162.47^\circ$ for the super-hydrophobic surface.

Hysteresis, evaluated also as in Moita *et. al.* (2016) [18] was found to be lower than 10° for the surface with the highest contact angle (coated with *Glaco®*) thus confirming its super-hydrophobic nature.

4 | Calibration and Data Processing Methods

4.1 Blackbody Calibration Sources

Black Body Calibration sources are recommended by the camera manual to calibrate the camera correctly. They are simply blackbodies with controllable temperature. The temperature controlled blackbody is to be filmed by the IR Camera and the camera's raw data (signal intensity received by the sensors) extracted. With a known temperature and high emissivity it is easy to correlate the signal intensity with the correspondent temperature. Establishing this relation can be done directly in the software but for the aforementioned reasons this was the procedure established and developed in this work.

The Blackbody Calibration Source is the name given to these devices, that are commercialized to calibrate infrared sensors. Given the high costs of these devices (over 7000 euros) a simple but functional Blackbody Calibration Source was projected and assembled in the present work.

There are several types of blackbody calibration sources, which are included in these main categories [12]:

- Fixed-Point Blackbody Radiators: used at really high temperatures ($>1000^{\circ}\text{C}$), these are characterized by having a metal (eg. Au, Ag or Cu) at freezing point and a graphite made cavity (high emissivity). The quality of the measure is defined by the quality of the graphite, metal ingot and shape of the cavity.
- Heat Pipe Cavities: used for applications with temperatures from -60°C to 1000°C , depending on the working fluid, these are characterized by having the best precision and being the most sophisticated devices. The cavity is surrounded by a multistate heated fluid at a controlled pressure. This cavity has special geometric properties to enhance the emissivity of the body. They are usually used in high precision applications for instance in meteorology institutes.
- Practical Cavities: used in more practical applications, they are used for a range of temperatures between -45°C and 450°C . Unlike the Heat Pipe, the working fluid rarely changes its physical state (eg. one could only go up until 100°C with water). Practical cavities are easy to build and

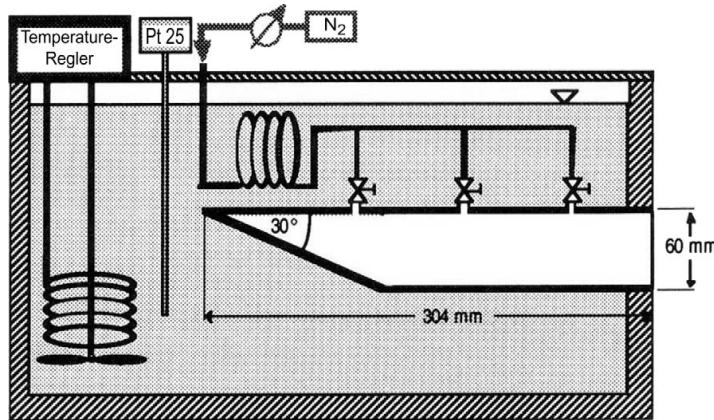


Figure 4.1: Pratical Cavity Blackbody Source scheme

Source: Chapter 3.2 from [12]

are often used for tests by radiation thermometers manufacturers. Similarly to the Heat Pipe Cavities also rely on specific geometric conditions to enhance the cavity's emissivity.

- Flat Plate: these devices are used as an alternative to the practical cavities because they do not require small cavities. As counterpart of in these devices, the heated plate must have a high emissivity, usually obtained using a high emissivity paint, so they may lead o large uncertainties. This method is usually used for large applications which do not require very accurate measurements.
- Others: Cryogenic/Vaccum Blackbodies are used for extreme values of temperature such as negative temperatures (as low as -100°C) and Furnaces used in this case as a Flat plate for temperatures above 1000°C.

For this work, the Pratical Cavity Radiator is the best choice, not only because it's often used for similar applications, within the same temperature range, but also because it is the simplest solution to build. The final design of the chamber was based on the scheme presented in Hartmann's work [12], and it's illustrated in Figure 4.1. The cavity shape is based on the design proposed in Figure 4.2. Since the camera had to be calibrated to work between 0 and 130°C, the working fluid selected here was oil, with high saturation temperatures (300°C at atmospheric temperature).

The effect of the cavity shape show in Figure 4.2 is used in many cavity based Blackbody Radiator Devices and is used to enhance the emissivity, by trapping the light, thus reducing the light reflected from the outside. This effect is enhanced by an angle of 30° as referenced in the literature [12]. A working scheme of the final design of the created device, with a mixture of these 2 concepts is presented in Figure 4.3.

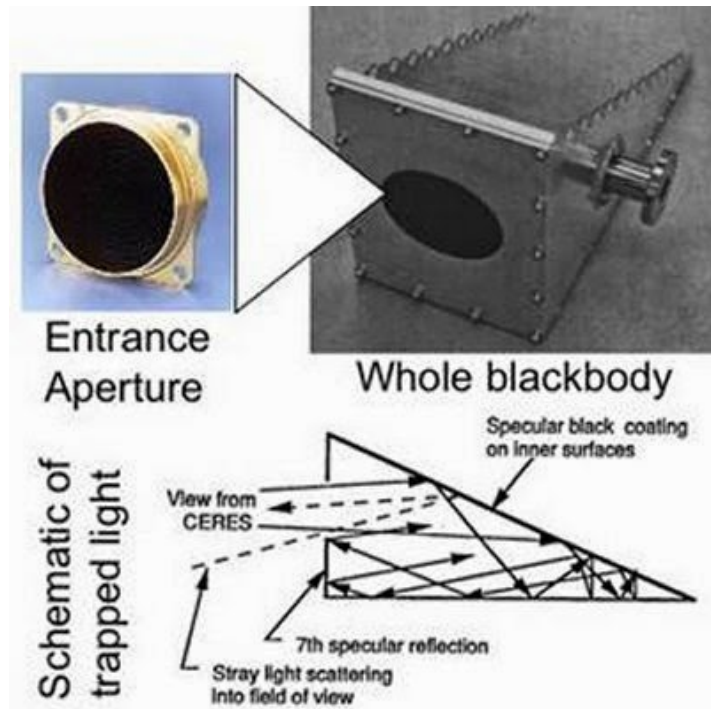


Figure 4.2: Cavity and light trapping effect scheme

Source: NASA

4.1.1 Design details

The final design render, made in SolidWorks, is depicted in Figure 4.4. One may notice, both from the render and the scheme, that the box is too long compared to the blackbody. The reason for this is that the whole device had to be made to fit the thermal resistances which were commercially available. This resistance is presented in Figure 4.5. The working fluid must have good conductive properties, so the type of oil used was car oil, which is stable under heating conditions.

In both the scheme and render, the sensors, peripherals of the device and its insulation are omitted. Five type K thermocouples were used: 2 submerge thermocouples by each side of the blackbody to check if there were high temperature variations in different regions of the device; 3 surface thermocouples to monitor when the temperature stabilizes in the face of the device that is recorded by the IR camera (for the calibration procedure), and to provide enough temperature measurements from which one could take a good average of the real cavity temperature. The positioning of the thermocouples is schematically depicted in Figure 4.6.

A KS 20-1 PID controller, that controls the resistance based on the temperature monitored by the middle surface thermocouple and a DT9828 Data Acquisition Board from Data Translation to connect the thermocouples to the computer were the data is processed.

Finally, the insulation consists of a 5mm PENA30FR adhesive, that is composed by sponge with

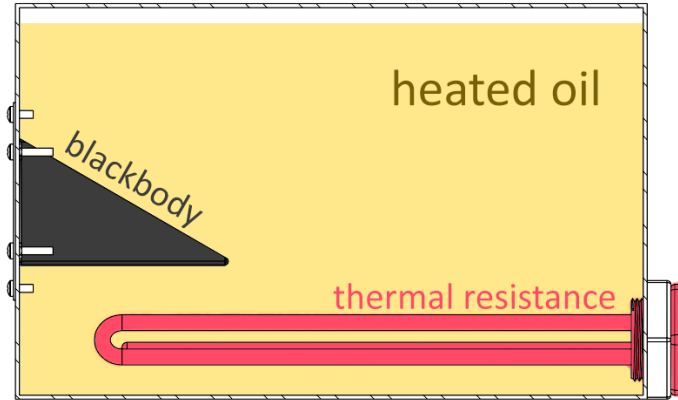


Figure 4.3: Final design scheme for the Blackbody Calibration Source

aluminum coating. This material can be seen in Figure 4.7. The insulation is used all around the device and the only hole in it is the opening for the blackbody.

4.1.2 Building Process

The building process of this device can be divided in 4 parts:

- The box: made in stainless steel, this box had to be ordered from a company specialized in metal work. The size of this box is 200x200x320 mm, with 2mm thickness. It already has 2 orifices to assemble the resistance and the blackbody. Thermal insulation was made to fit the box measures. The box is insulated only when both the blackbody and resistance are already installed.
- The resistance: bought from Mecafil, has a power of 1500W and was attached to the box with the help of a nut (glued to the back with cold weld). The hole used to accommodate the electrical resistance is also used to fill in and drain the device with the oil. The junction between the nut and the bolt was also reinforced with high temperature silicone, and the screw of the resistance was covered with a Teflon tape to avoid leakages.
- The blackbody: is made by laser cut from a 1mm stainless steel plate, painted with a black matte paint, then bent and finally welded. After the weld, the blackbody had to be re-painted and its insulation reinforced with high temperature silicone. Finally it had to be screwed to its support plate so it could be placed in the box. The end result can be seen in Figure 4.8. This piece was made removable so that new shapes could be made, giving room to the future improvements of the device. When placed on the device it is important to put some high temperature silicon to fully prevent any leakages.
- The peripherals: starting with the sensors, holes were made on the top of the box so that every sensor could pass through it. The scheme for the holes and the sensors display was already shown in Figure 4.6. The Data Acquisition Board and the PID controller need to be placed near

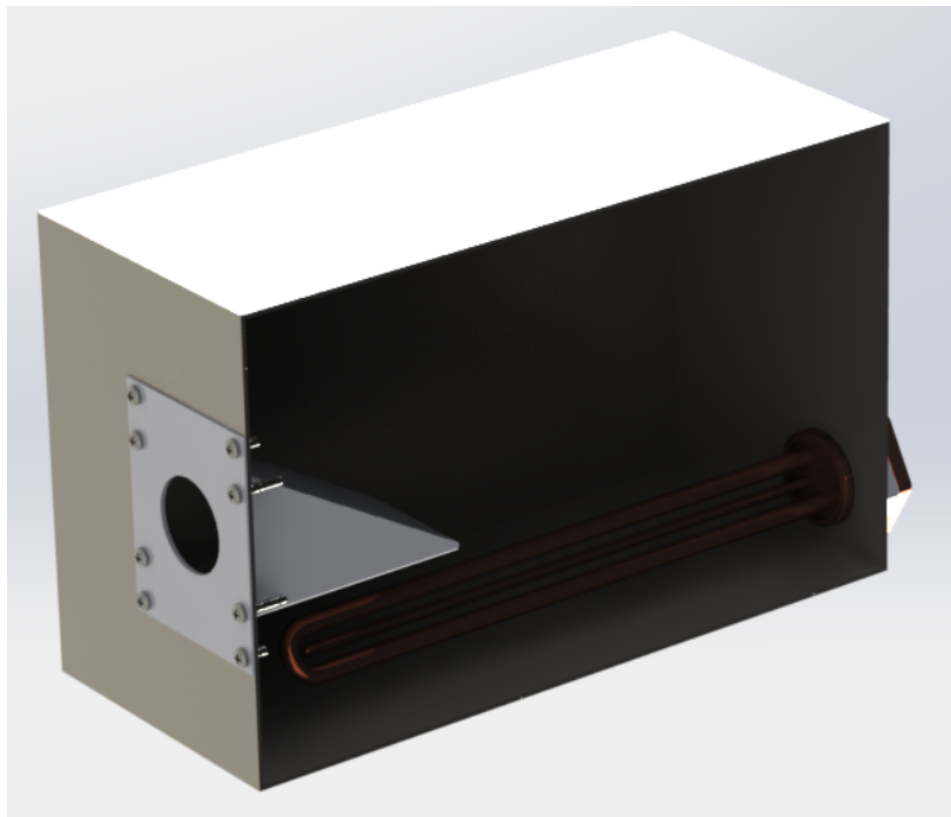


Figure 4.4: SolidWorks render of a cut device view



Figure 4.5: Thermal Resistance used

the box because of the sensor wire length restraint, so a support was made to accommodate everything.

The final setup, after all parts were mounted can be seen in Figure 4.9. With this setup, it is possible to collect and control temperature values, and correlate them with the camera data. This device was used to perform 2 different calibrations, that will be explained further ahead in this chapter.

4.2 Calibration process

A number of steps must be followed before starting the actual calibration process:

- Fill the device with oil.

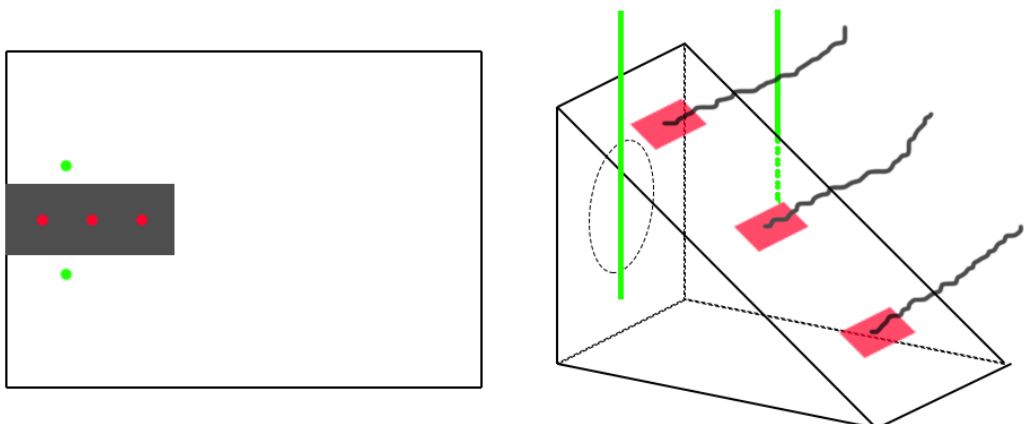


Figure 4.6: Thermocouple placement scheme

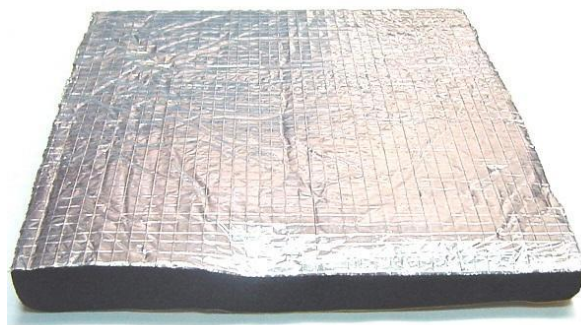


Figure 4.7: PENA30FR Adhesive Insulation

- Connect the thermocouples to the Data Aquisition Board and to the PID Controller.
- Turn on the IR Camera and start both its software (Xeneth) and the board software (QuickDAQ).
- Define an adequate integration time to the desired temperature interval.
- Perform an offset calibration with the camera software.

Now the camera can be calibrated using the software's calibration feature or the custom made process proposed here. While in the software calibration is automatic, in the custom made calibration the average ADU of the selected region needs to be registered along with the average temperature read by the sensors on an Excel sheet.

The overall setup for the custom made calibration is assembled in Figure 4.10. The desired temperature is set and is gradually increased in $10^{\circ}\text{C}/20^{\circ}\text{C}$ increments to have a wide range of tempera-

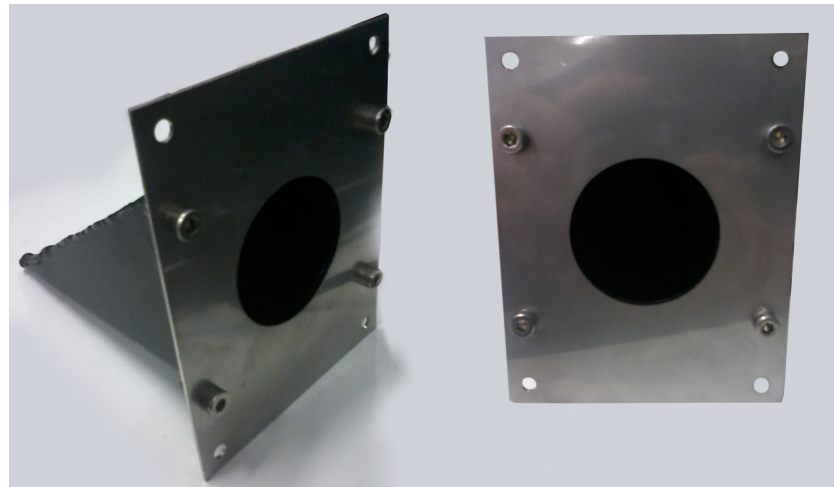


Figure 4.8: Completed Blackbody

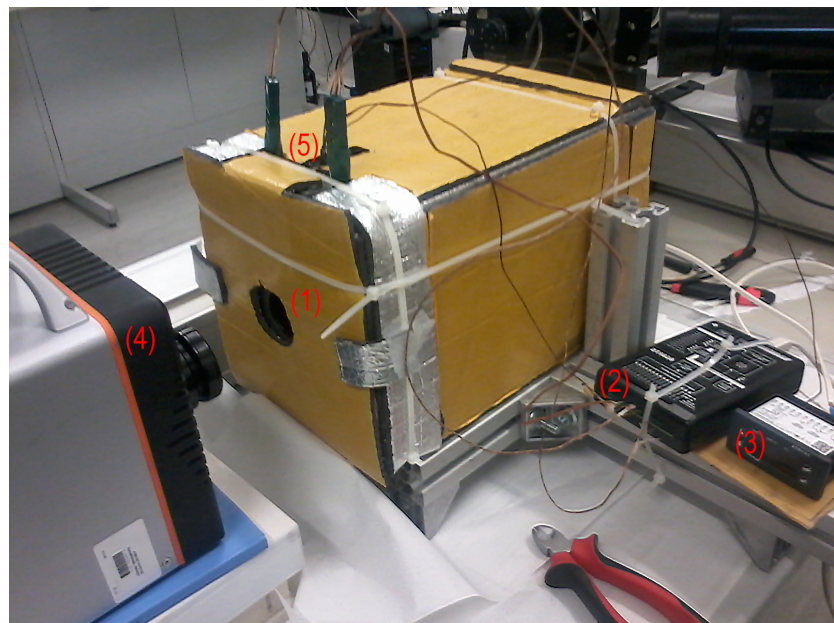


Figure 4.9: Completed Blackbody Calibration Source: (1) Blackbody cavity; (2) Data Aquisition Board; (3) PID controller; (4) IR Camera; (5) Thermocouples (one connected to the PID, the others to the Data Aquisition Board)

tures (up to 130°C). Each set temperature must stabilize until the image of the cavity shows a uniform temperature within the entire selected area. For instance, Fig. 4.11 shows that the edges of the cavity are hotter than the remaining cavity region. This is due to different thermal properties of the materials used to assemble the cavity blackbody.

This problem is solved by the PID controller. To understand this, one can summarize the way the PID is working to control the temperature as follows: the input target temperature of the PID is compared with that read by the thermocouple connected to the controller, and it turns on and off the resistance to keep the temperature constant within a desired range (+/-1°C). The resistance is turned off just before the oil is at the desired temperature in order to account for thermal inertia of the device and for the delays in the controller.

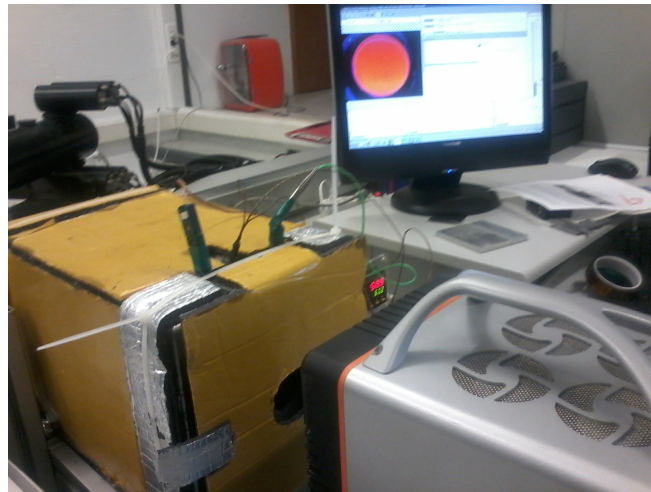


Figure 4.10: Calibration Instalation in Function

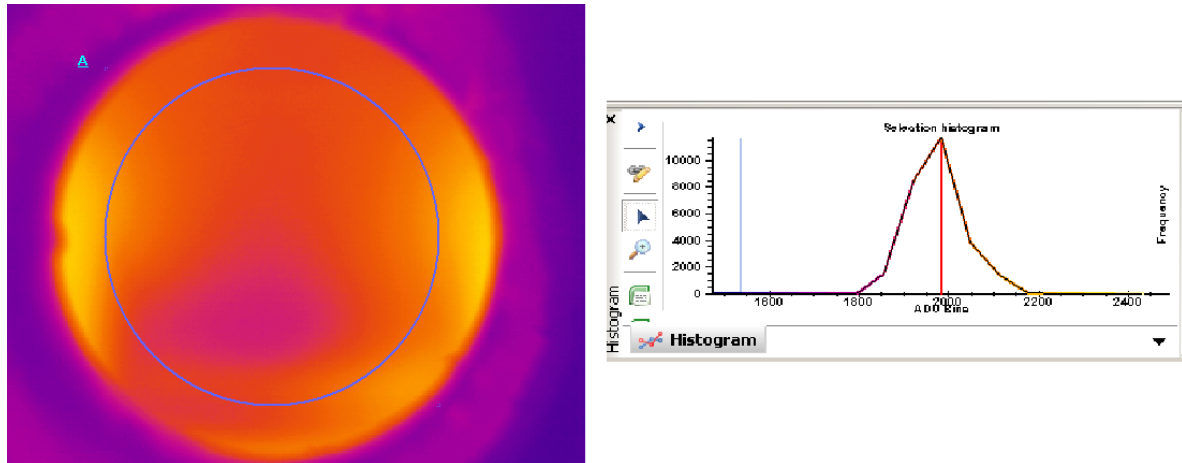


Figure 4.11: Blackbody thermal image and its respective histogram

So, when the electrical resistance is off, the thermal inertia of the oil and the good insulation of the Blackbody device allow reaching a uniform temperature in the cavity, as the device cools down. This can be clearly seen in Fig. 4.12. The histograms show perfectly the desired conditions (the peak on the right histogram contrasting with the wider dispersion of values in the left histogram in Figure 4.12).

To see what temperature corresponds to the averaged ADU value, an average of the surface thermocouple read temperatures in time was taken, with the help of the software QuickDAQ, which allows to take a data sample for a fixed amount of time. This is used to make the average between all the surface thermocouples connected to the board and the value shown in the PID. This final average is then the input for the software calibration or saved with the ADU in an excel for the second method.

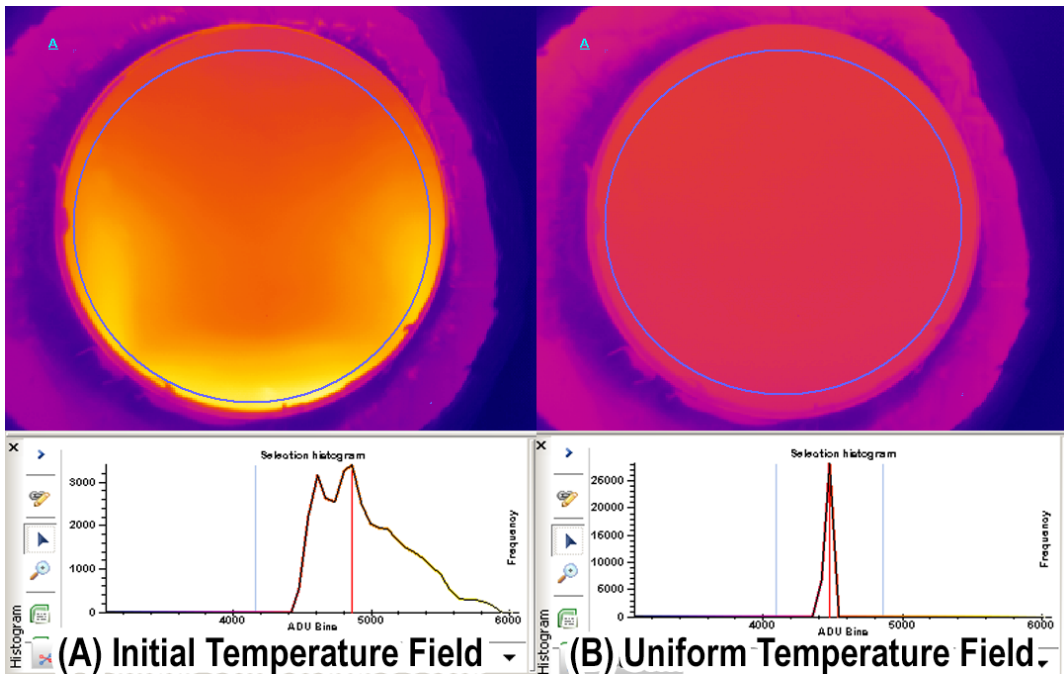


Figure 4.12: Calibration example: initial temperature field, and uniform temperature field (after ≈ 5 min)

4.2.1 Software Calibration

The Xenics' software has a camera calibration wizard (in which the offset calibration feature is included) that automatically correlates the ADU's with the temperature measured. The feature described is called "Temperature Calibration (Plank)" and can be seen in Figure 4.13. In the shown interface, the user can input the temperature measured by the thermocouples in the field (a), and then add the read value with button (b). It will then add a point to the table at the left and draw in on a graph bellow. This point has the given temperature, and the ADU measured with a spatial average of a small rectangular area in the center of the image.

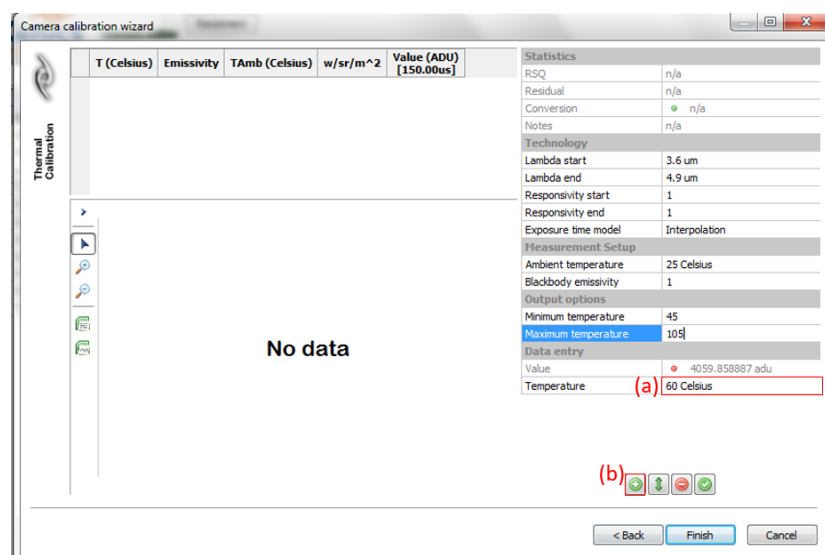


Figure 4.13: Xeneth's software - Temperature Calibration (Plank)

In the first calibration, this method was tried but because the temperature and respective measured ADU are shown it didn't invalidate the possibility to use them in the second method, our custom made calibration. In this attempt an integration time of 450 was used. The final table and graphic can be seen in Figure 4.14. On the table labeled as (a) one can see 5 columns. The first and last columns depict the read values of temperature and ADU, respectively. The second and third columns show the ambient temperature and emissivity which are actually irrelevant for the present calibration as one assumes the cavity to be a perfect blackbody, so the ambient temperature won't be used in this calibration. The fourth column is a variable, which depends on the input temperature, that the software uses to convert, together with the other inputs, the temperature, in a quantity called "Soaled Radiance", represented in the x axis of graph (b) in Figure 4.14. This variable is not explained in the manual, nor its relation with the temperature. This was one of the disadvantages of this method mainly because the software creates the "Soaled Radiance" value out of it, and it is supposed to maintain a proportional relation with the ADU's so the calibration correlation is linear. But as it is noticeable in the graph, the values do not follow the line that closely, which caused a significant deviation.

Having this variable and the "Soaled Radiance" unexplained, the only option was to take these values and use them in the other method. Another reason is that this method does a linear correlation. This may only be a vague assumption or a rough approximation, and because even if the origin of these variables was known, there would be no way to validate that linear relation.

In the end, the software creates a calibration conversion that can be selected when it is opened and used to take the data directly in Celsius. This calibration file can only be used for the specified integration time. In Figure 4.14 it's possible to see how the software approximates linearly (green line) the measured points (red line). Because this calibration didn't match the experimental values as close as desired, when the newly created calibration pack was tested it didn't work properly, so the second type of calibration was made.

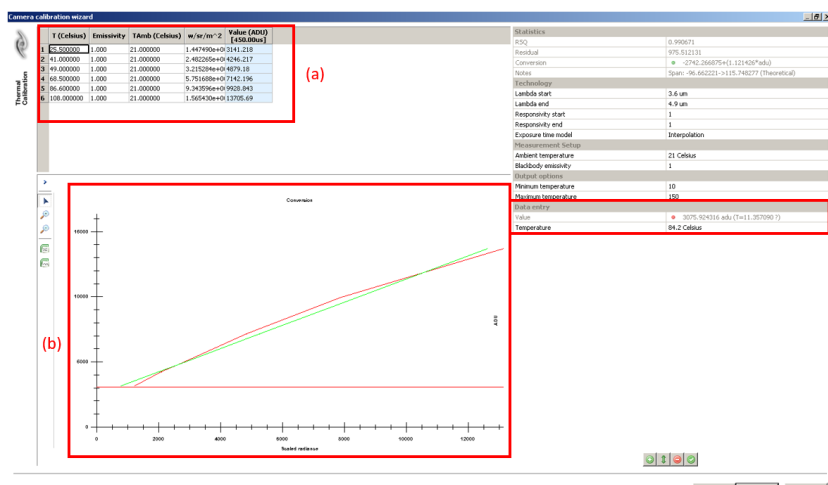


Figure 4.14: Complete Temperature Calibration (Plank)

4.2.2 Proposed Calibration

Being unable to trust the calibration method provided by the camera software, a custom made method was developed. In this method the calibration results (average ADU in a selected region) are taken directly from the software, without using the software's Calibration Wizard. They're saved in an Microsoft Excel sheet together with the average temperature read by the thermocouples. With this method the results have to be taken raw from the software and then process them with the MATLAB code that was made just for this purpose. A whole explanation of the process will be given in the next section, leaving in this section a general outline of the proposed method.

The process of data aquisition for the calibration is similar to the previous calibration. The main difference in this method is the absence of the Calibration Wizard. Instead, the Selection Panel (described in 3.2.2.B) is used to gather the average measured ADU of a circular area, similar to what can be seen in Figure 4.12. There are several advantages in this method, one being that it was now possible to adjust the temperature range (the Calibration Wizard didn't allow it), and better understand when the image saturates. Another advantage is the fact that it is possible to change integration time.

In Microsoft Excel, the measured temperatures are converted into the radiated energy using equation 2.10 (and considering the object perfectly black) and plotted against the ADU. Then Microsoft Excel's trending line function is used to extract a polynomial curve that will best approximate the data gathered in the experiments. The second and third degree polynomial approximations were compared, but in the end the third degree polynomial. This option took longer to process but the end result was significantly closer to the experimental results.

With the extracted curve a MATLAB code was made to calibrate the videos. The raw data video data (in ADU) matrix is the input of this function. This matrix has the value for every pixel in every frame, and point by point is solving the following equation:

$$A \times W_{tot}^3 + B \times W_{tot}^2 + C \times W_{tot} + D = ADU_{pixel} \quad (4.1)$$

in which A,B,C and D are the coefficients of the calculated polynomial curve, ADU_{pixel} is the pixel ADU value and W_{tot} is the wanted radiated energy. Using this radiated energy value, the pixel temperature is calculated using equation 2.11. The end result is a matrix with all the temperatures.

4.2.3 Calibration Process Details

One important fact about the designed calibration procedure is that it took a whole day to complete. This is due to the fact that there was no refrigeration system and the liquid had to cool at room temperature. Also the overheating of the device often leads to leakages due to material expansion and break down. This problem, which often would not allow to repeat the calibration process in a regular way, took some time to address.

Two calibrations were made during this work. The first was made using the software at the fixed integration time of $it=450\mu s$. The second was made using the proposed method for the integration times of $it=450\mu s$ and $it=200\mu s$. With the integration time of $it=450\mu s$ the image would saturate at around $108^\circ C$, so the correspondent results weren't suited for the experiments represented here which would reach higher temperatures.

The results of the calibrations is shown in Table 4.1. Since the results were taken for both calibrations at $it = 450\mu s$ we can use them to prove the method's consistency. The comparison is presented Figure 4.15.

Table 4.1: Calibration Results

Calibration 1			Calibration 2				
it=450us			it=450us		it=200us		
T($^\circ C$)	ADU	$W_{tot}(W/m^2)$	T($^\circ C$)	ADU	$W_{tot}(W/m^2)$	ADU	$W_{tot}(W/m^2)$
25.5	3141	450.1533	25.46	3200	449.912	1645	449.912
41	4246	551.1904	34.5	3794	506.9481	1900	506.9481
49	4879	609.5461	44.28	4666	574.5844	2285	574.5844
68.5	7142	771.1625	62.27	6287	716.4103	3021	716.4103
86.6	9928	948.1167	75.76	8270	838.8605	3890	838.8605
108	SAT	SAT	84.33	9827	924.4022	4596	924.4022
			94.54	12094	1034.669	5586	1034.669
			103.67	14078	1141.372	6690	1141.372
			114.39	SAT	SAT	8139	1276.958
			125.74	SAT	SAT	9885	1433.317

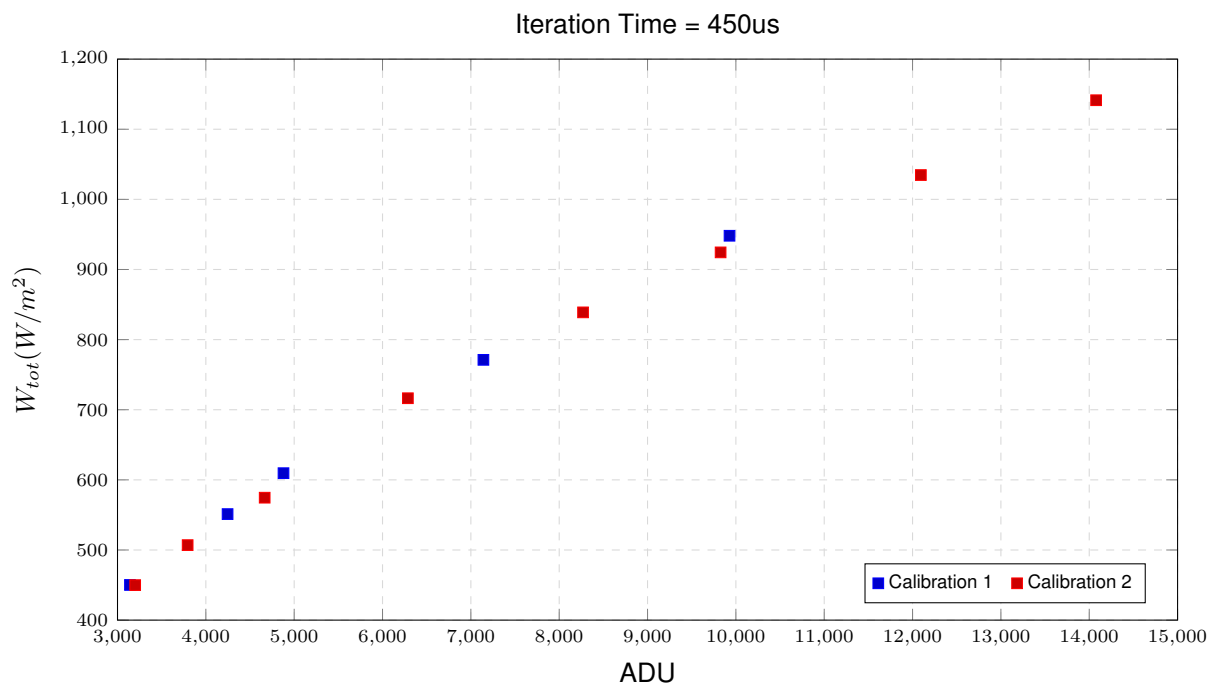


Figure 4.15: Comparison of the two calibrations at $it=450\mu s$

Next, the $it = 200\text{us}$ data has to be plotted, and a trending line calculated. The data with the correspondent trending line can be seen in Figure 4.16. The equation that is represented in the plot is the one used in the calibration code.

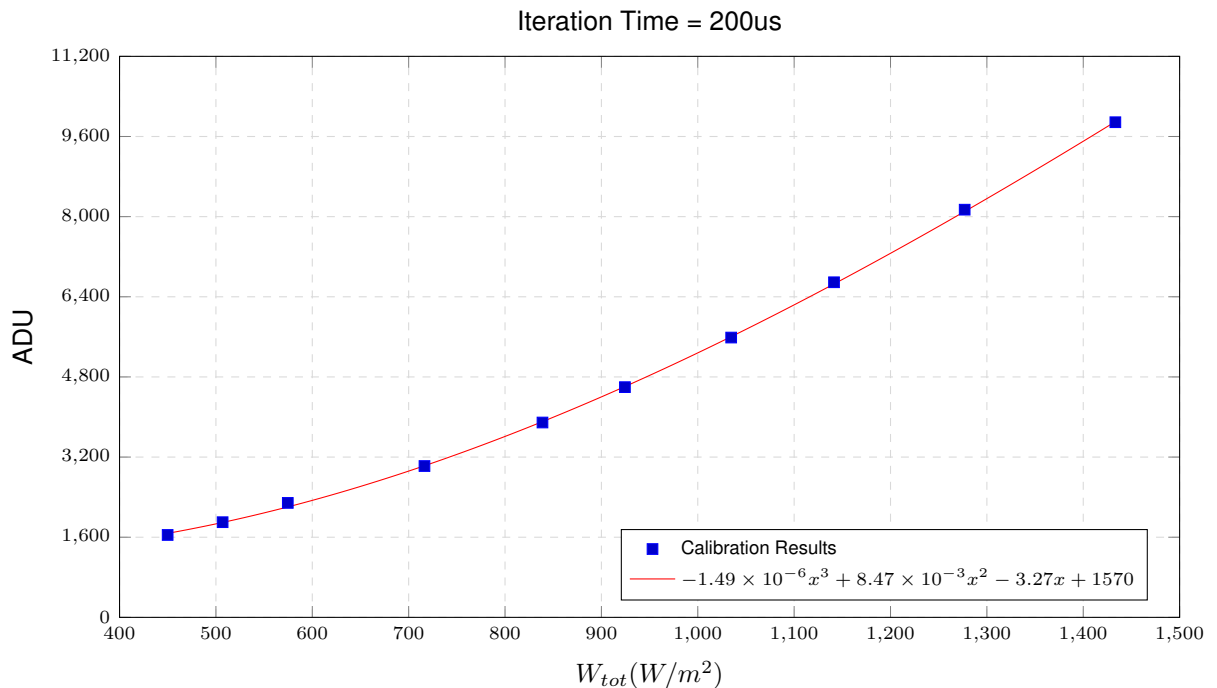


Figure 4.16: Comparison of the two calibrations at $it=450\text{us}$

The generated code is used to transform every video from ADU values to Celsius, and works only for the selected integration time. The code can also be easily adapted to the integration time of 450us. This code can be seen in Appendix A.

4.3 Data Processing Methods

The collected images, without any sort of treatment, have some random noise and unwanted patterns of noise. While the noise source is usually small differences in sensitivity or calibration of the sensors, the patterned noise has its origin mainly on the software processing. A temperature difference is always noticeable inside the region of interest. This cannot be solved so, to accurately evaluate the results, a background remove has to be performed. This also helps removing some background noise.

To be treated, the video needs to be imported to avi format, in an 8 bit, grey scale format. In MATLAB, the video is divided into frames and the grey scale value transformed to temperature, considering the temperature or ADU scale it was imported with. After this, the calibration is applied and finally the filters. In the end, the results are extracted as a MATLAB file with all values and a txt with the results from the center to the radius of the droplet with a plot option.

4.3.1 Patterned Noise

The origin of this type of noise was detected in the software's zoom function. It can result in significant errors. At constant temperature the results showed that the difference between pixels side by side was 1°C . To remove this, a filter was made that would add and subtract 0.5°C alternately. The generated pattern and the effect of the filter can be seen in Figure 4.17.

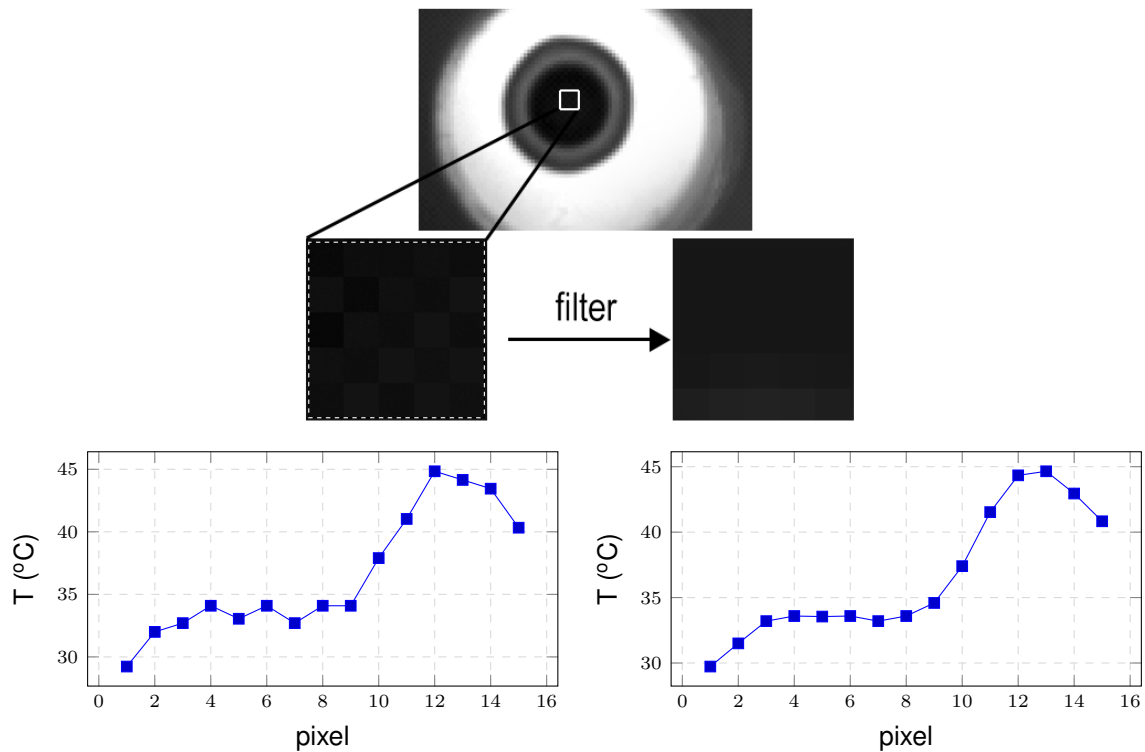


Figure 4.17: The effect of the filter in both the image and a line of point temperature values

4.3.2 Median Filter

This filter has the potential to remove random bad pixels noise from the picture. This filter is a MATLAB function that outputs the median of a 3-by-3 neighborhood of the input pixel. With this simple filter the image can be greatly improved as shown in Figure 4.18. On the right there's the image without the filter and on the left the treated image.

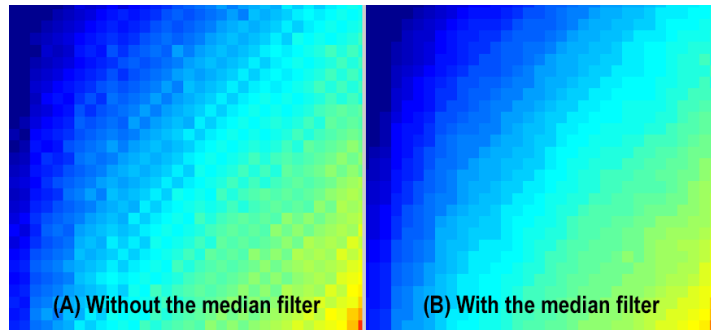


Figure 4.18: Median filter effect

4.3.3 Background Filter

The background filter serves the function of eliminating any problems related with the optics of the camera and to equalize the temperature field. Two different ways to do it were thought. Two MATLAB codes were made and tested. The first one is the simple way and is shown in Equation 4.2. The variable vid is the matrix with the temperature value for every pixel in every frame, $avTemp$ is the average temperature in the center of the hole and t_n is the number of the analyzed frame.

$$vid^*(x, y, t_n) = vid(x, y, t_n) - vid(x, y, 1) + avTemp \quad (4.2)$$

The second one is a weighted background removal and we can see it in Equation 4.3. The variables bear the same meaning, but has to be done for each pixel (x_p, y_p) . Only the code for the latter can be seen in Appendix B as the code is similar in both cases.

$$vid^*(x_p, y_p, t_n) = \frac{vid(x_p, y_p, t_n) - vid(x_p, y_p, 1)}{vid(x_p, y_p, 1)} avTemp + avTemp \quad (4.3)$$

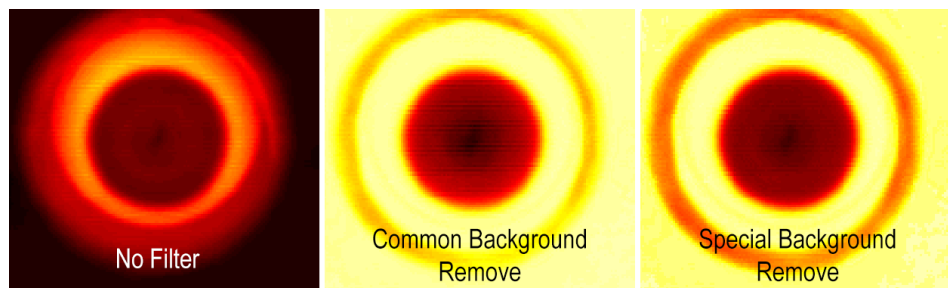


Figure 4.19: Background filter effect

4.3.4 Heat Flux computation

To evaluate and compare the heat removal capacity of the system it is very important to compute the heat flux and cooling effectiveness, mentioned in Section 2.4. This was also made with the help of a MATLAB code, that can be seen in Appendix C and D.

Starting with the computation of the heat flux the code is a discretization of Equation 2.21. This equation can be divided in three terms: the provided heat flux, the spacial term and the temporal term. This problem was addressed as being axisymmetric, so the spatial derivative becomes a one-dimensional problem. To address the second order derivative in the spatial term a backward discretization with first order precision was applied:

$$\frac{\partial^2 T}{\partial r^2} \approx \frac{T_i - 2T_{i-1} + T_{i-2}}{\Delta r^2} \quad (4.4)$$

The temporal term has a first order derivative, that was addressed the same way and discretized using a first order precision backward method:

$$\frac{\partial T}{\partial t} \approx \frac{T_t - T_{t-1}}{\Delta t} \quad (4.5)$$

To compute the cooling effectiveness, one has to solve Equation 2.25. This means integrating the flux both in time and space. This integration was approximated using the trapezoidal integration method. Starting with the spatial integration first:

$$\int_A q'' dA = \int_\theta \int_r r \times q''(r) dr d\phi \quad (4.6)$$

using integration by parts this integral and assuming the flux to be axisymmetric (no variation in θ) one can write the integral as:

$$\int_\theta \int_r r \times q''(r) dr d\theta = \left(r \int_r q''(r) dr - \int_r \frac{d}{dr} r \int_r q''(r) dr dr \right) \times 2\pi \quad (4.7)$$

To compute the integral now, one just needs to apply an trapezoidal approximation:

$$\int_r q''(r) dr \approx \frac{q''(r) + q''(r+1)}{2} \times \Delta r \quad (4.8)$$

$$\int_r \int_r q''(r) dr dr = \frac{q''(r) + q''(r+1) + q''(r+1) + q''(r+2)}{4} \times \Delta r^2 \quad (4.9)$$

Finally, the temporal integral was addressed similarly:

$$\int_t P_{diss}(t) dt = \frac{P_{diss}(t) + P_{diss}(t+1)}{2} \times \Delta t \quad (4.10)$$

This integral is solved for every timestep so that is possible to obtain a graphic of the time evolution for this parameter.

5 | Experimental Results

5.1 Introduction

This chapter explores the use of the IR camera (after taking the calibration procedures) to describe the heat transfer occurring at droplet wall interactions. The analysis focus on discussing the potential and limitations of this technique. Additionally the heat transfer processes are investigated, addressing the effect of liquid properties, surface wettability and surface temperature

5.2 Side View

This experiment served as an introductory case study to get familiar with the camera characteristics. As stated before, the geometric implications of the droplet shape in radiation prevent the extraction of quantitative results, as well as the transmissivity of the liquid to infrared, although it's close to 0 for water.

This experiment addressed two different impact velocities: 2 m/s and 0.8 m/s, and three initial foil temperatures: 60°C, 100°C and 110°C. The results obtained in this configuration are shown in Figure 5.3 and Figure 5.2, mainly illustrative results. In this figure, the x axis represents the distance between the bottom of the droplet to its top. These results show that for the same impact velocity, the temperature gradient in the droplet, from the surface to the top, evolves similarly along time irrespective of the surface temperature. The temperature at the liquid-solid interface is naturally higher than that on the bulk of the droplet. At early stages the temperature at the interface is also lower than at later stages of spreading, when the thickness of the lamella becomes thinner. As for the impact velocity comparison, the results show a bigger temperature increase at the lamella's base for the higher impact velocity profile.

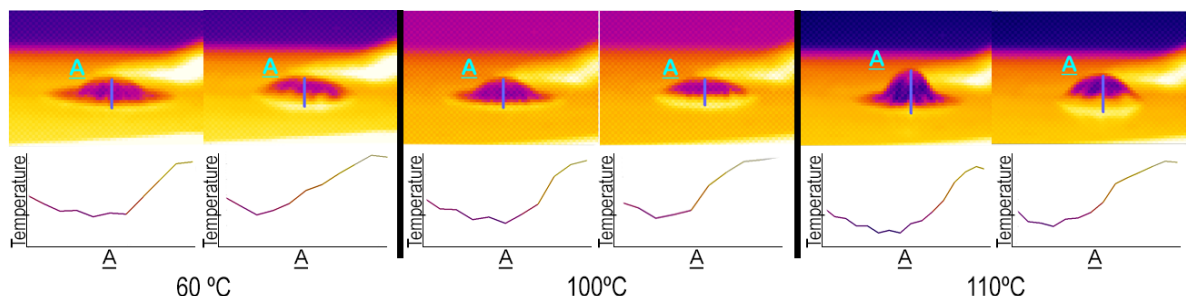


Figure 5.1: Side view of the water droplets impacting the hydrophilic foil at 2 m/s: spreading and receding phases

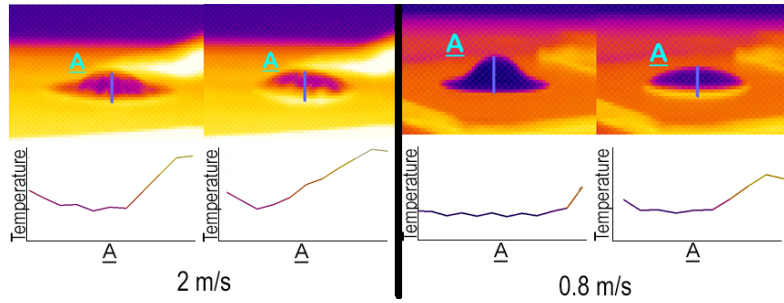


Figure 5.2: Side view Results for 60°C during the spreading and receding phases

5.3 Bottom View

The images obtained in this configuration are mainly bidimensional temperature maps of the area on the surface corresponding to the area that is wetted by the droplet. From this map one can obtain the distribution of the temperature along the droplet radius for small time steps. Further post processing of the collected data was used to compute the heat flux and cooling effectiveness (as explained in Chapter 2), to compare the results obtained in the various experimental conditions. The connection between the high-speed images, temperature map and temperature plot is depicted Figure 5.3.

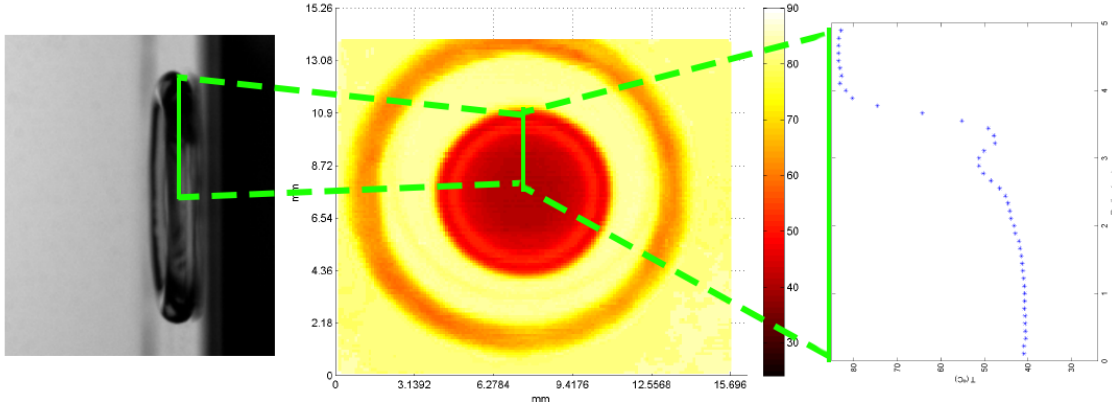


Figure 5.3: Example of the results representation

In fact various conditions were tested, namely two different impact velocities, 0.8 m/s and 2 m/s, and four initial foil temperature values, for conditions before and after the saturation point, 60°C, 80°C, 100°C and 110°C. Additionally, two different wettability conditions were compared, namely using the hydrophilic foil and the super-hydrophobic, coated foil. Finally, tests were also performed with two liquids: water and ethanol. As for each of the conditions, 5 different experiments were made, so that the repeatability of the tests could be confirmed. In Figure 5.4 the repeatability of these tests can be seen with the example of the 60°C results for 2 m/s.

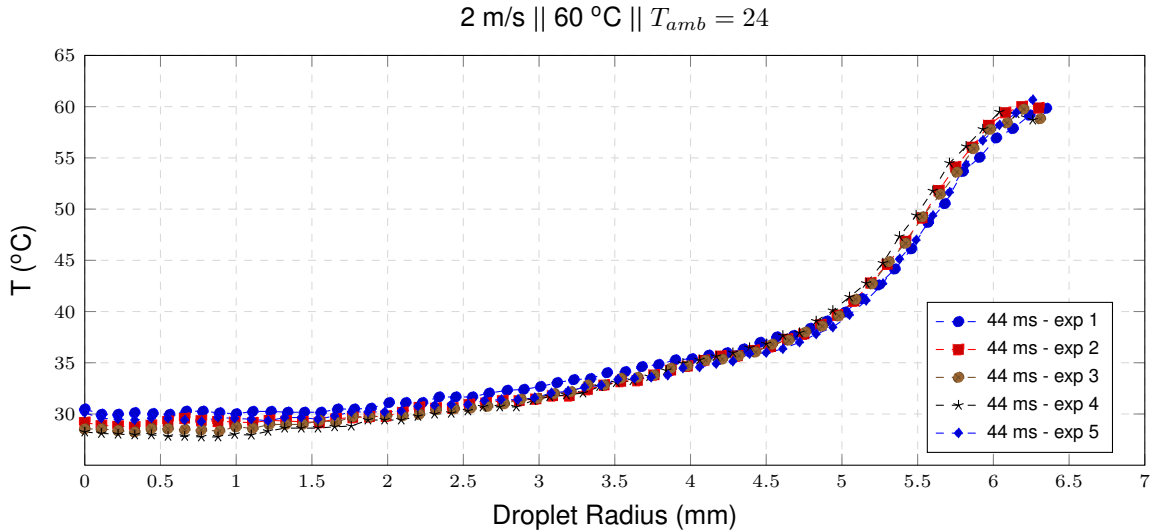


Figure 5.4: Repeatability of the experiments

5.3.1 Result of applying the custom made calibration method

Some preliminary images were taken using the camera calibration, which were then compared to those using the custom made calibration detailed in Chapter 4. To evaluate the quality of the calibration it is important to compare the results and interpret the differences. The result of applying the calibration process is discussed for the impact of water droplets at 2 m/s and 0.8 m/s, for initial foil temperatures of 60°C, 100°C and 110°C. Due to deviations in the ADU to Celsius conversion, these exact temperature values could not always be achieved, so the real working temperature is provided. Figure 5.5 compares the temperature variation on the foil as a function of the spreading droplet radius for the impact velocity of 0.8 m/s the different curves in each plot correspond to different time instants of the spreading. So, in the time instants chosen to depict impact (e.g. t=1ms) the temperature decrease of the center region of the droplet is small and swiftly recovers for the still small spreading ratio. This contrasts in the higher temperature drops at later time instants.

Before comparing the images, one should bare in mind the differences in their conditions. The results before calibration were taken at a different ambient temperature, proximity to the droplet and framerate. The average framerate of the results before the calibration is 990 fps, and 1100 after. These improvements were the result of having more experience dealing with the camera during this work. This results in better temporal and spatial resolution in the data obtained after the calibration. Hence one can only compare similar frames and differences may be accentuated by that.

One important aspect is that the apparent diameter (the diameter that one can perceive from the temperature plots, that is representative of the wetted area) is approximately the same with and without this improved calibration process. During the spreading phase (all the points before 13 ms) the new calibration and method captures a bit of the air trapping effect mentioned previously in Section 2.4. The mentioned effect is not captured in the results without the calibration. Another thing that

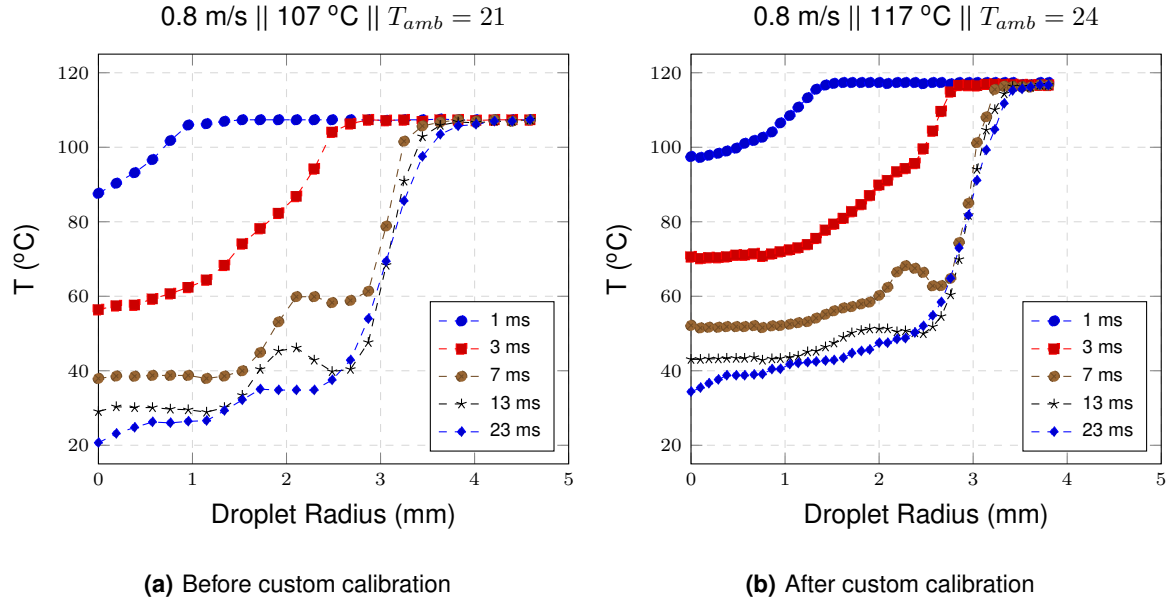


Figure 5.5: Comparison between results with and without the proposed calibration

was corrected, was the fact that the temperature at the center of the droplet ($r=0$) would drop below the ambient temperature in the Figure 5.5. This is impossible because the droplet is at ambient temperature. The cause of this is related to optical effects, that were nullified by the calibration. On the other hand the results obtained using the custom made calibration have some noise that couldn't be addressed without losing resolution. The cause of the noise is probably the improved setup that allowed higher spatial resolution. So while there are advantages using the factory calibration, the proposed calibration can better portrait the physical phenomena.

5.3.2 Simultaneous analysis of droplet dynamics and thermal processes

One of the main objectives of this work is to use the high-speed camera simultaneously with the IR Camera to compare physical phenomena with thermal phenomena. The results were put together in Figure 5.6. In this figure it is possible to see some of the stages of a droplet impact. Analyzing the images, it's observable the physical phenomena that have an impact on heat transfer. During the spreading, the lamella's rim is visible in the temperature maps, as introduced in Section 2.4, starts forming in the second millisecond. When the edge reaches maximum diameter it reverses direction and starts the recoiling phase, shown in the 12 ms images. The thickness of the water layer is smaller right before the lamella's edge. In this area there is less heat removal. So, as expected, one can see a ring of higher temperatures, and a slope in the plot. After the recoiling phase the droplet starts to stabilize, and due to its hemispherical shape the heat flux is higher at the center, so the temperature is lower in the center. Although here there is no rim in the lamella by this phase, one can clearly see the lighter ring on the IR Image. This is the cause of thermal inertia.

Another type of results can be obtained for the collected data and these are the heat flux and

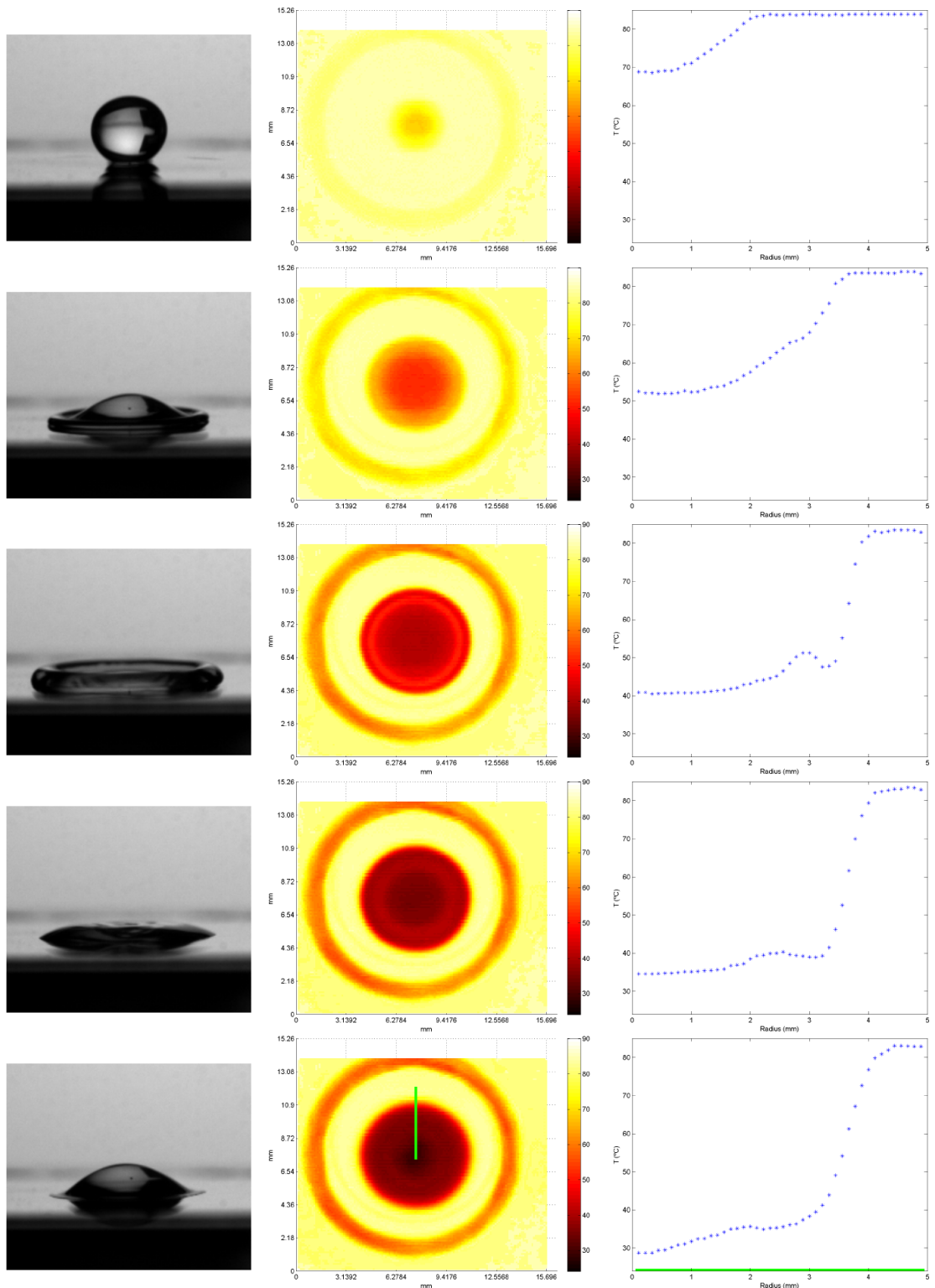


Figure 5.6: Comparison between High Speed camera images and Infra Red images for 0.8m/s and 80°C at 0, 2, 6, 12 and 22 ms after the first contact on a hydrophilic surface

cooling effectiveness. Starting with the heat flux, an example of the obtained graphic can be seen in Figure 5.7. Looking at the heat flux, one can see the expected phenomena, described in the literature [19]. There are only some comparable results between Figure 2.8 and the collected results, as the timestep of the simulation is much smaller. The contact edge heat flux peak couldn't be captured in the initial timesteps, but is clear in the posterior frames. This contact edge peak is a reflection of cold water being pushed to the edge of the lamella as the droplet spreads. In the center the spatial gradient is ignored because of the problem's axisymmetry. The highest peaks for the initial times aren't captured by the IR Camera, but the flux drop before the peak, in Figure 2.8, is visible in the 1ms and 2ms frame. The spatial dispersion of the flux in early frames is clear in the experimental results. This may be caused by thermal inertia and heat diffusion along the foil. This may also be the cause for the innexistence of a peak in the early frames. In the last frame, which, according to Figure 5.10, is already during the receding phase, the heat flux is negative after the droplet edge. This is caused by the area being no longer wetted and is now heating again. Also the heat flux drop before the contact angle peak is an indicative of the presence of the lamella's rim in that area. Also the heat flux is very small compared to other timesteps due to the droplet temperature raise.

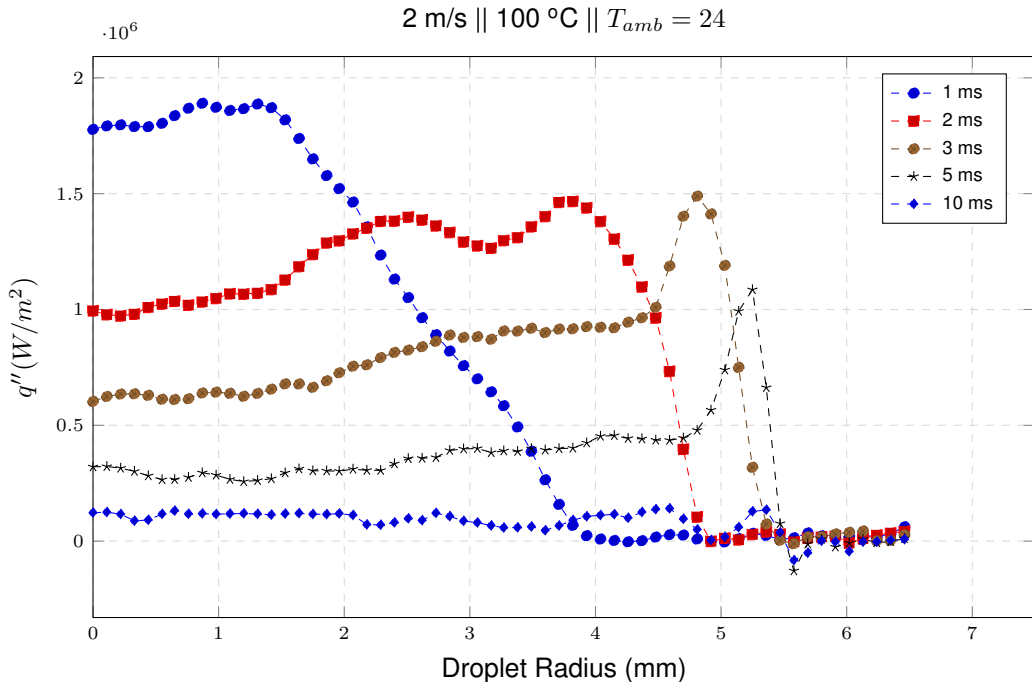


Figure 5.7: Heat Flux along the radius of a water droplet, $u_i = 2 \text{ m/s}$, Surface temperature=100°C

Observing the cooling efficiency graphic in Figure 5.8, a comparison with [19] can be made. Using this graphic as a reference a very similar evolution with time can be seen. The adimensional parameter t^* is used to consider the impact velocity in a comparison. The evolution stagnates as the droplet's temperature increases and the foil temperature decreases. The cooling effectiveness is higher in the numerical results. This may be the cause of a different initial flux or foil size. It can also be the cause of the ideal conditions assumed in the numerical simulation.

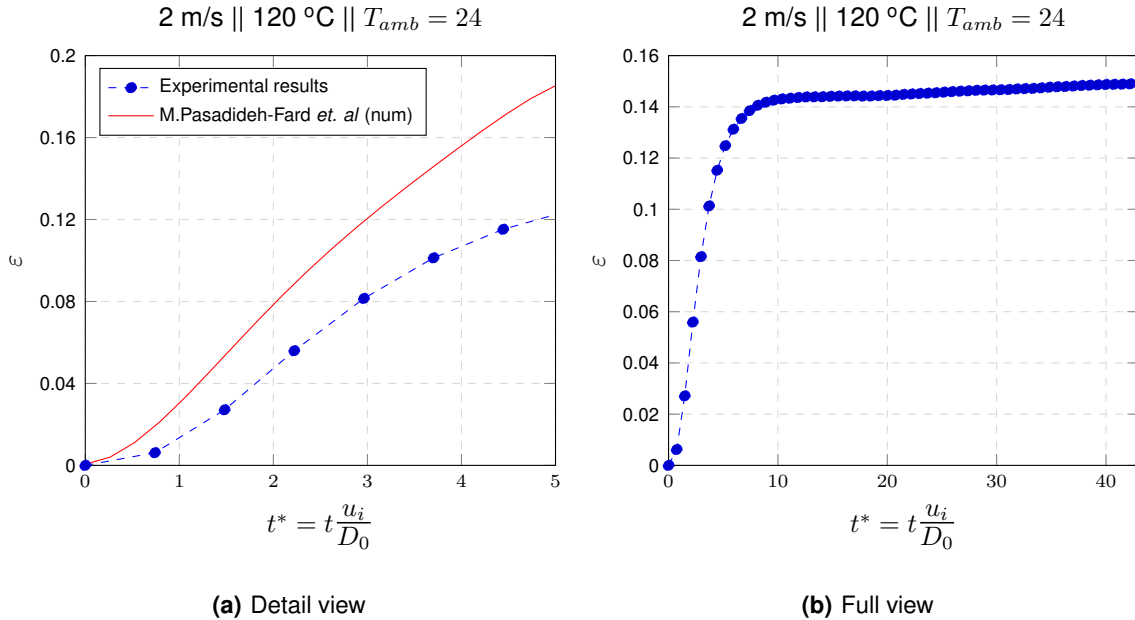


Figure 5.8: Cooling effectiveness along t^* for a water droplet impacting on an hydrophilic surface

5.3.3 Influence of the impact velocity

For an hydrophilic surface (the stainless steel foil), results were taken for different impact velocities: 0.8 m/s, 2 m/s at an initial heating of 100°C. At this temperature, boiling of the lamella is not yet observed. The two impact velocities are compared in Figure 5.9. The obvious difference is observed between the droplet spreading at different impact velocities is the spreading diameter, which is directly influenced by the impact velocity. One of the differences is the fingering, that only happens for 2 m/s (at $t=6\text{ms}$). The height of the lamella is also smaller for this velocity.

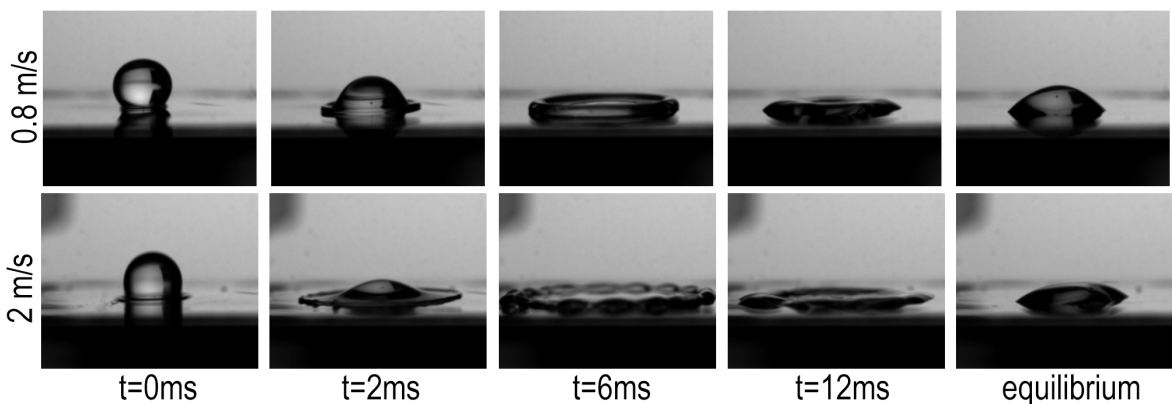


Figure 5.9: Comparison of droplet impact at 0.8m/s and 2m/s. The water droplet impacts the surface at an initial temperature of 100°C

Using the high speed camera it was possible to extract the droplet diameter for each frame, with the help of a code developed previously by Tomás Valente. The comparison between the spreading

factor of each velocity can be seen in Figure 5.10. As expected the spreading factor grows more with a higher impact velocity. In this figure the difference between the maximum diameter time can be compared. In the case of 2 m/s the time in which the maximum diameter occurs is at approximately 4 ms, and in the case of 0.8 m/s occurs at 6 ms. The spreading factor difference in maximum diameter has a relation of approximately 2.5 to 4, which is considerably larger.

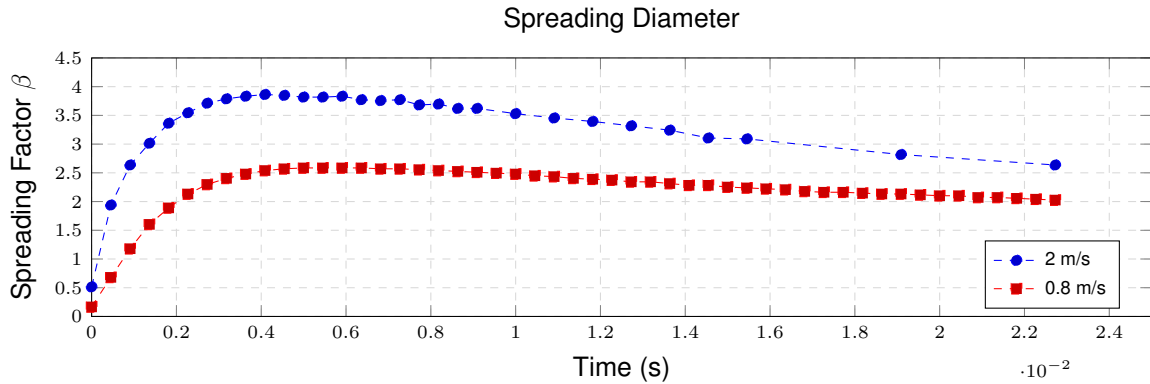


Figure 5.10: Comparison between the spreading factor of each velocity

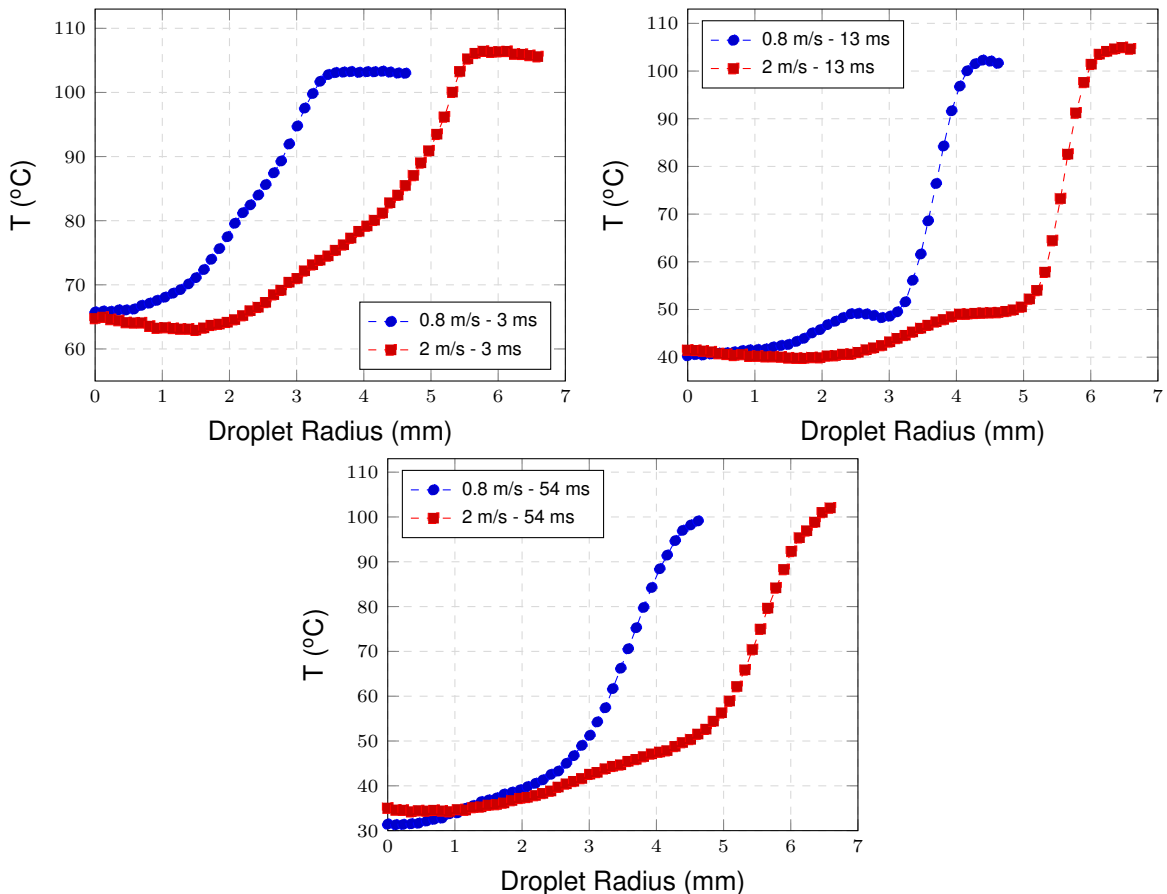


Figure 5.11: Average temperature along the radius between the 5 experiments of both velocity values at 100°C

Lets now take a look at the influence of the velocity in the temperature field. In Figure 5.11, the average of all experiments made for both velocity values at 100°C is presented for comparison. The

temperature at the center of the droplet is similar during the spreading (3ms and 13 ms). The temperature at the droplet center drops more intensely in the lower velocity. This is justified by the height difference, also noticeable in the last panel of Figure 5.6. Looking at the shape of the curves, one can observe their similarity.

The temperature fields can only give us qualitative information. To quantify cooling and compare both velocities, the heat flux and cooling effectiveness should be considered. Starting with the heat flux, the measurements made for an droplet impacting on a hydrophilic surface at initial temperature of 120°C were taken as an example. The comparison between different impact velocities is shown in Figure 5.12. For both time frames, the contact edge can be easily identified, and the same phenomena are present: the contact edge peak, the peak and drop of the flux caused by the lamella's rim and the heat flux drop in the center due to the trapped gas bubble effect. Overall the flux is higher in the 2 m/s due to the wetted area being larger. The fact that the lamella is thinner in the 2 m/s impact velocity tests, is compensated by the increase in convection heat transfer. As seen before, when reaching equilibrium, the lamella is hotter for the 2 m/s measurements. This is the cause of having a thinner lamella with greater heat flux promoted by convection, which heats the droplet to higher temperatures than in the 0.8 m/s impact velocity case study. This can be also related to the fact that even though the lamella thickness is higher in lower velocities, the heat flux is comparable or even lower, as seen in the figure.

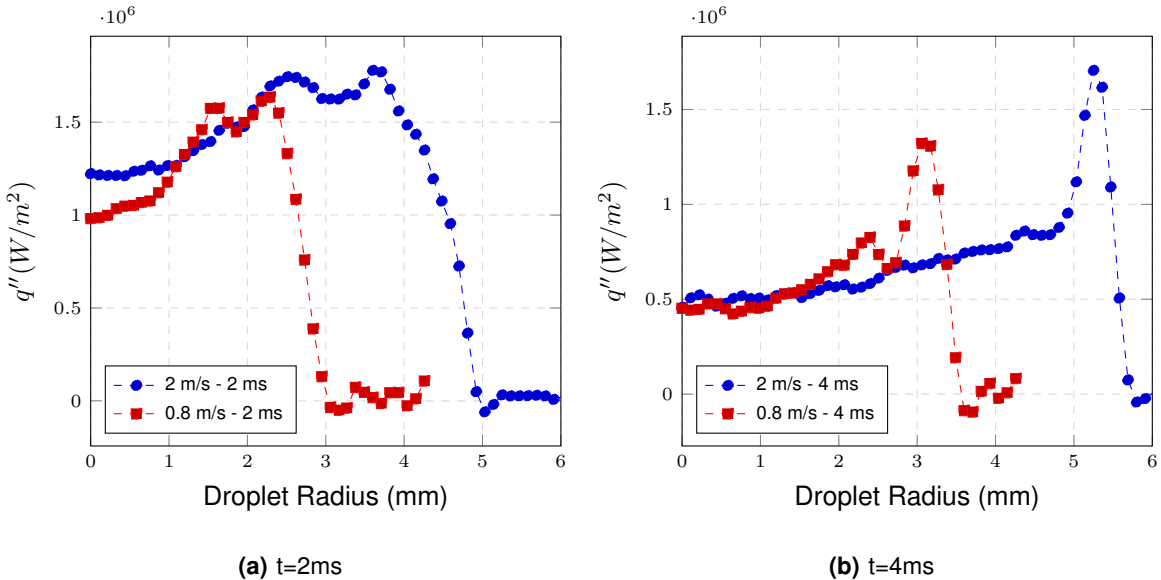


Figure 5.12: Comparison of the heat flux computed for different impact velocities. The water droplets impact the surface which is at an initial temperature of 120°C

To study the influence of the impact velocity, the results for each velocity were plotted together, using non-dimensional time. The generated plots for the temperature at 120°C can be seen in Figure 5.13. In a first analysis it is possible to see similar changes in the curves for different impact velocities

(Figure 2.9). These plots show the difference in cooling effectiveness. It is clear that the higher impact velocity impacts show more heat removal capacity than the lower velocity ones. This is not always the case though. In the first instants after impact the lower impact velocity impacts show more efficiency in removing heat. But when it comes down to the latter time steps the effectiveness more than doubles with the impact velocity.

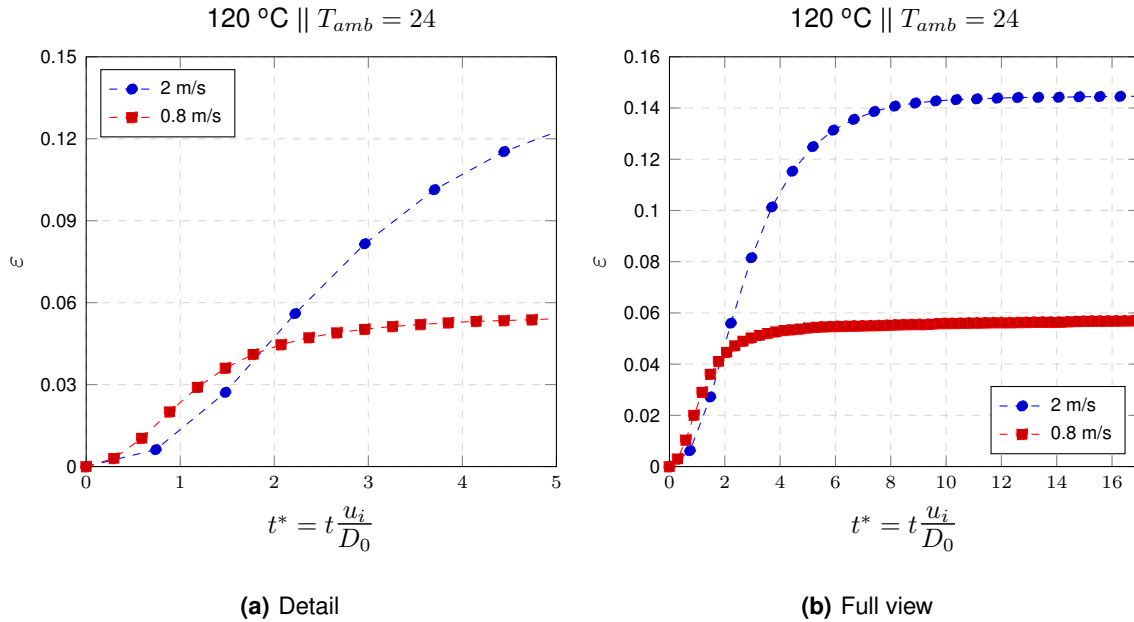


Figure 5.13: Computed cooling effectiveness comparison between two different impact velocity values for the initial foil temperature of 120°C

With these results it is possible to reaffirm what some previous authors studied. The impact velocity affects positively the cooling efficiency as the wetted area is bigger and convection heat transfer increases.

5.3.4 Influence of the initial foil temperature

This section will address the relative temperature drop in the foil for the tested temperatures. The temperatures had to be adimensionalised so that they could be compared. This analysis, for a fixed impact velocity of 0.8 m/s, can be seen in Figure 5.14. In this figure one can see that for different initial temperatures, the relative temperature drop is very similar in the center region, but has a significant difference in the edge area. This may be due to the different spreading diameters at that time (larger input velocities lead to larger spreading diameters), which can shift the curve.

This is a confirmation for the effectiveness of the weighted background test. Because there is little variation between the adimensionalised temperature maps, one may argue that the relative variation of the temperature is similar. This legitimizes the use of the weighted background removal as a mean

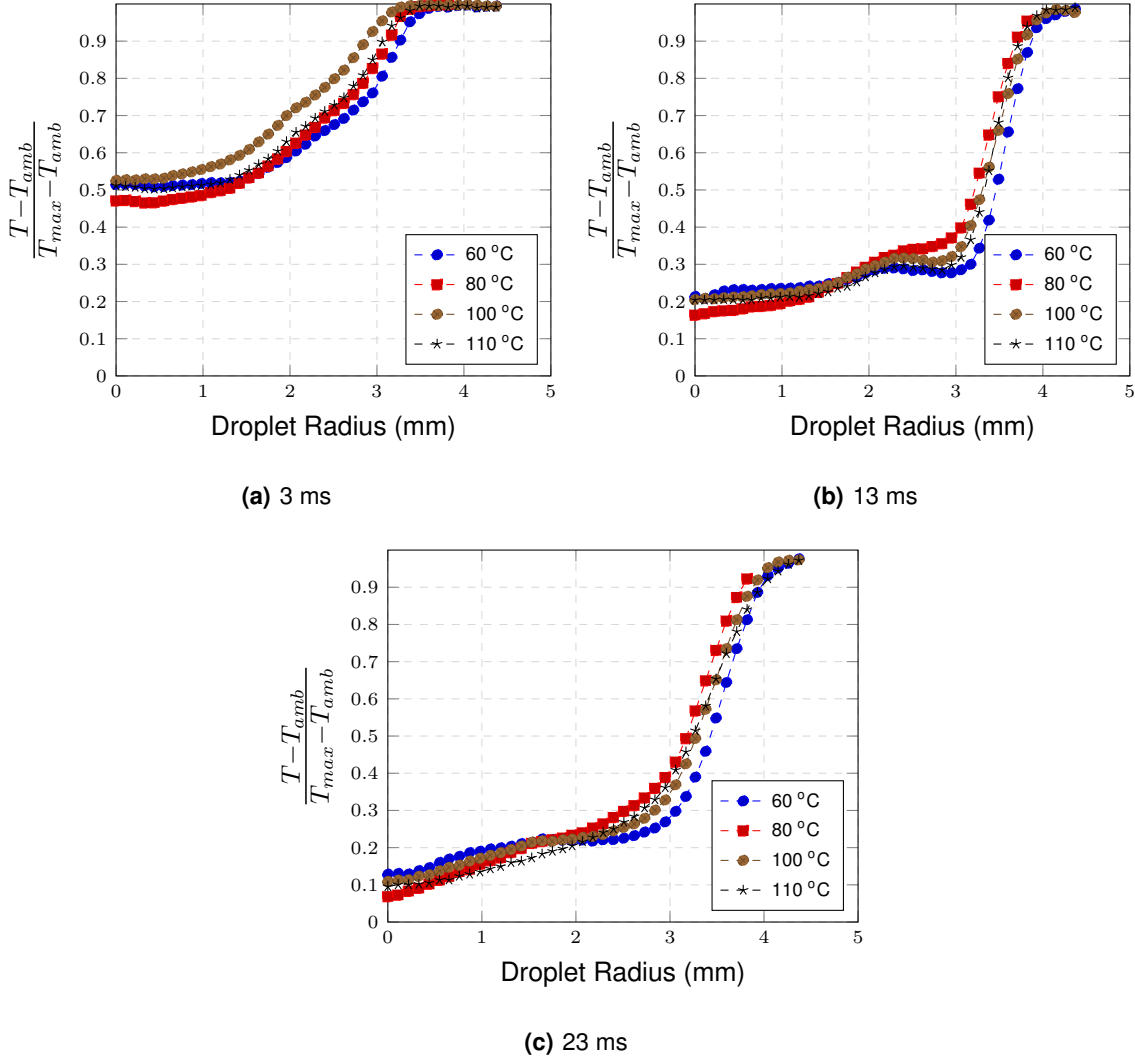


Figure 5.14: Average adimensional temperature along the radius for 4 different initial temperatures at 0.8 m/s

to obtain a uniform initial temperature.

To infer if the initial foil temperature has a relevant effect on the cooling effectiveness, one needs to plot several this parameter for several temperatures at the same impact velocity. These results are depicted Figure 5.15 and 5.16. In Figure 5.15 it's clear that all curves are close to be coincident so, the initial temperature doesn't influence the cooling effectiveness. But one needs to be careful making this statement because, for 2 m/s, in Figure 5.16, it's noticeable that the 110°C curve is not close to the others, but instead is converging to a higher cooling effectiveness. This is due to phase change of the liquid which occurs during spreading, as the lamella's thickness is thinner at $u_i = 2 \text{ m/s}$, so boiling may occur within this thin lamela.

Neither in the qualitative nor quantitative studies does foil temperature effect the performance of the liquid in cooling it. When liquid phase change occurs this may improve the cooling effectiveness, although it isn't clear if the obtained results reflect that, as the difference between this and the other

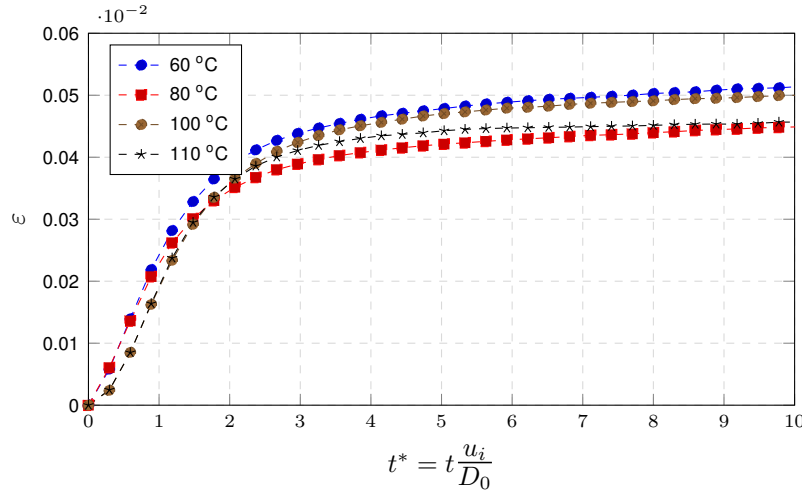


Figure 5.15: Cooling effectiveness for various initial foil temperatures with an impact speed of 0.8 m/s

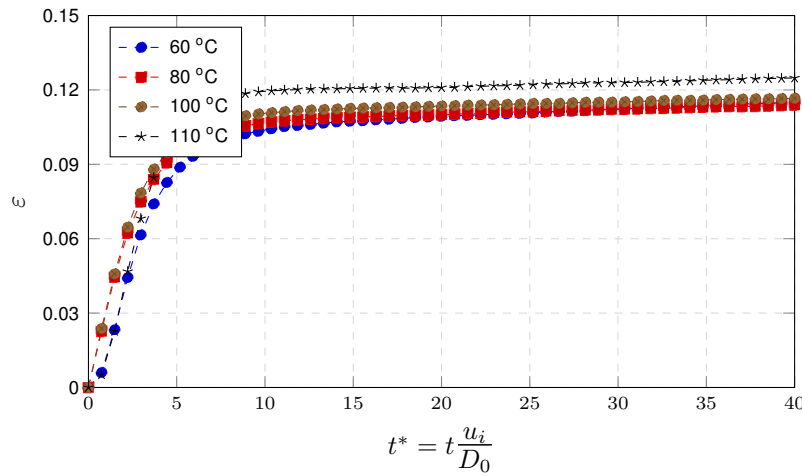


Figure 5.16: Cooling effectiveness for various initial foil temperatures with an impact speed of 2 m/s

curves is still small and one cannot see the boiling of the lamella which may be incipient.

5.3.5 Effect of liquid surface tension

The effect of the liquid surface tension is addressed here comparing the thermal processes occurring at the impact of water and ethanol droplets for initial surface temperatures below saturation.

Given the lower surface tension of ethanol, the spreading factor is much larger than that of water, so the lamella is also much thinner. This reduced thickness of the lamella of the ethanol droplet became an obstacle when performing the experiments since for initial foil temperatures above saturation ($T_{sat} \approx 80^\circ C$), the applied electrical current is very high deforming the stainless steel foil. These deformations are not relevant for the spreading of the water droplets but is enough to promote the lamella to slip away from the measurement area, being impossible to capture IR images under those conditions. Hence, the only measurements that could be performed for ethanol were obtained for the lowest impact velocity (0.8 m/s) and for initial foil temperatures of 40°C and 60°C.

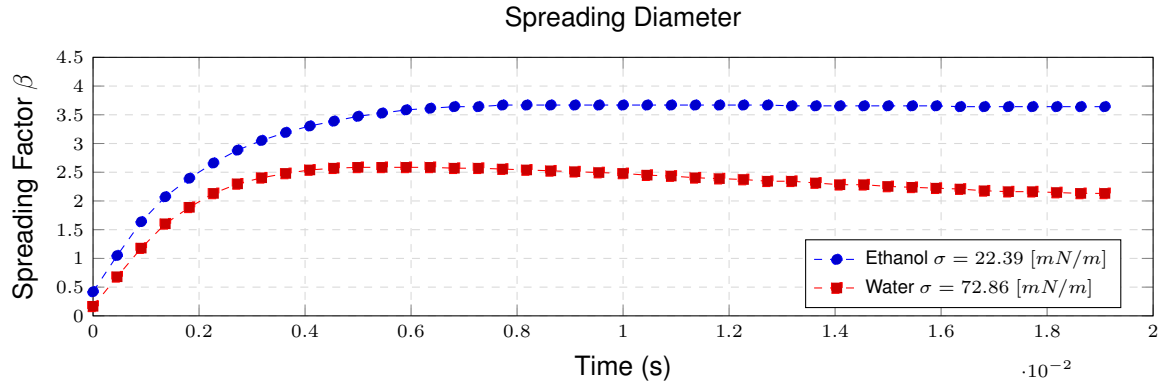


Figure 5.17: Spreading Factor along time for a water and ethanol droplet with an impact velocity of 0.8 m/s at $\Delta T = 20^\circ C$ from saturation

The spreading factor obtained for water and ethanol droplets is depicted in Figure 5.17. The maximum spreading factor is reached at 8ms after impact for ethanol and 4 ms after impact for water. Furthermore, ethanol droplet does not recoil but continues the spreading up to very later times after impact in a regime that is governed by capillarity. Naturally the wetted area of the spreading ethanol droplet is larger than that of water. Qualitative high-speed images of both water and ethanol droplets, shown in Figure 5.18 clearly show the differences quantitatively observed in Figure 5.17.

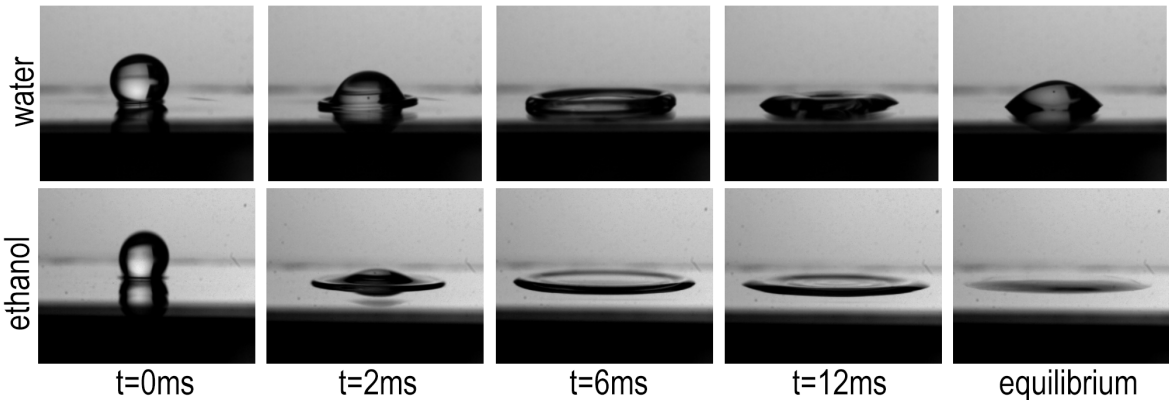


Figure 5.18: High speed images for a water and ethanol droplet impact at the velocity of 0.8 m/s

To compare the two liquids under similar conditions of initial foil temperature, the first approach was to consider the same temperature difference from the saturation temperature of each liquid. So initial foil temperatures were addressed to compare the two liquids for $\Delta T = 20^\circ C$ and $\Delta T = 40^\circ C$. However, the obtained results showed that this was not a good approach since the temperature influence is relative to the initial foil temperature (i.e. the relative percentage of temperature decay from the saturation temperature) so a new non dimensional temperature is used instead, as depicted in Figure 5.19.

The results shown in this Figure are in agreement with those reported in Figure 5.17 in the sense that they confirm the larger spreading diameter and the delay in the spreading of the ethanol droplet.

The lamella rim, previously identified for water liquids, is also less visible in the ethanol spreading. This is mainly due to the lower thickness of the lamella of the ethanol droplet. The fact that water reaches lower temperatures is mostly related to the worse thermal properties of the ethanol.

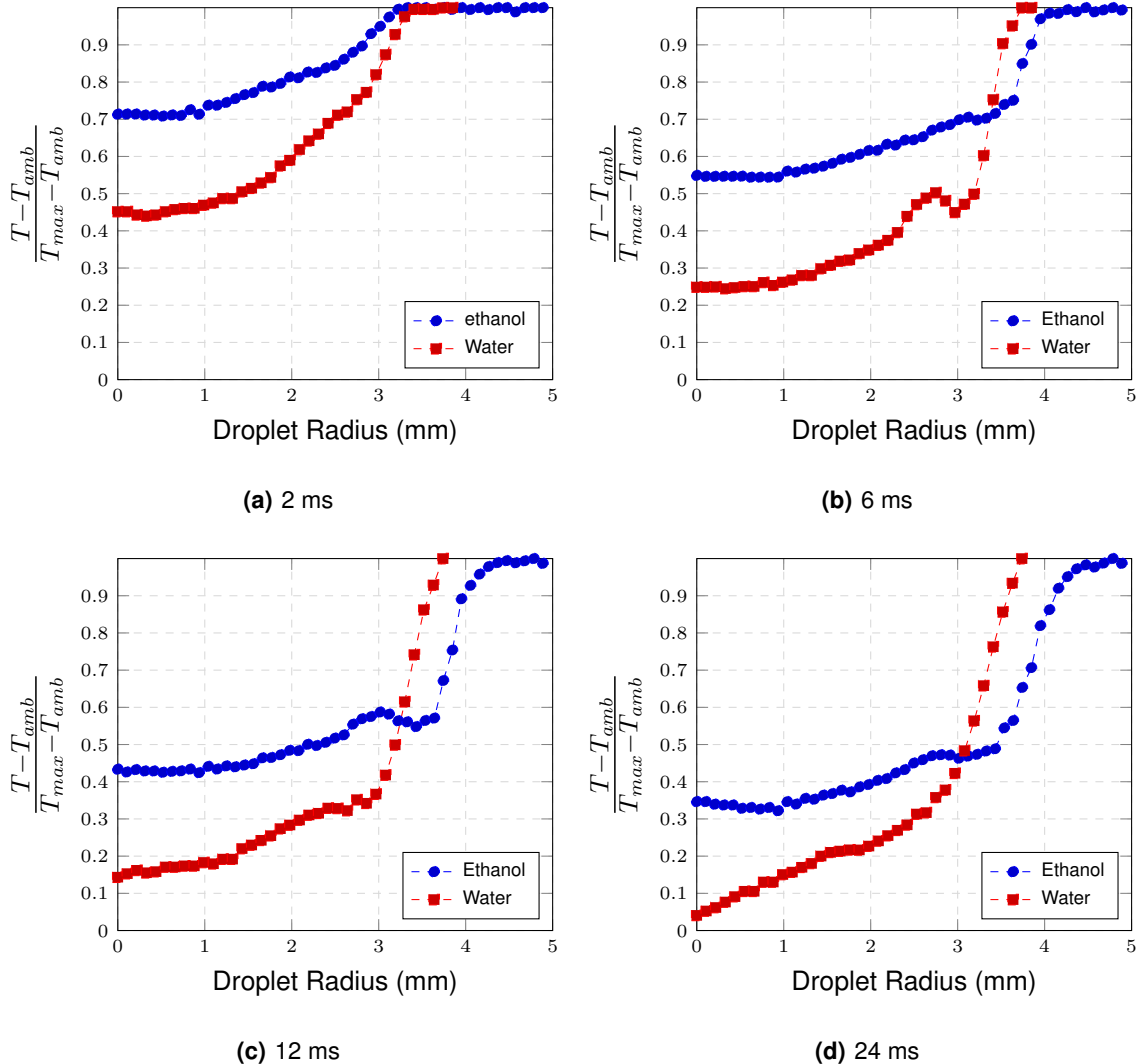


Figure 5.19: Average temperature along the radius for Ethanol and Water for a droplet impacting at 0.8m/s on a foil initially with $\Delta T = 20^{\circ}\text{C}$ under saturation

The heat flux can also be compared between both liquids. Looking at the plots in Figure 5.20, an elevated heat flux difference is visible between water and ethanol. The water droplet extracts more heat from the foil than the ethanol droplet. This trend is however affected by the slightly smaller initial diameter of the ethanol droplet ($d_0=2\text{mm}$ for ethanol and 3mm for water) and due to the aforementioned different temperature difference between the initial foil temperature and the saturation temperature which is actually much different (in percentage).

Hence heat flux isn't directly comparable between experiments, but one may compare the cooling effectiveness of both liquids as this parameter takes into account both the droplet's initial

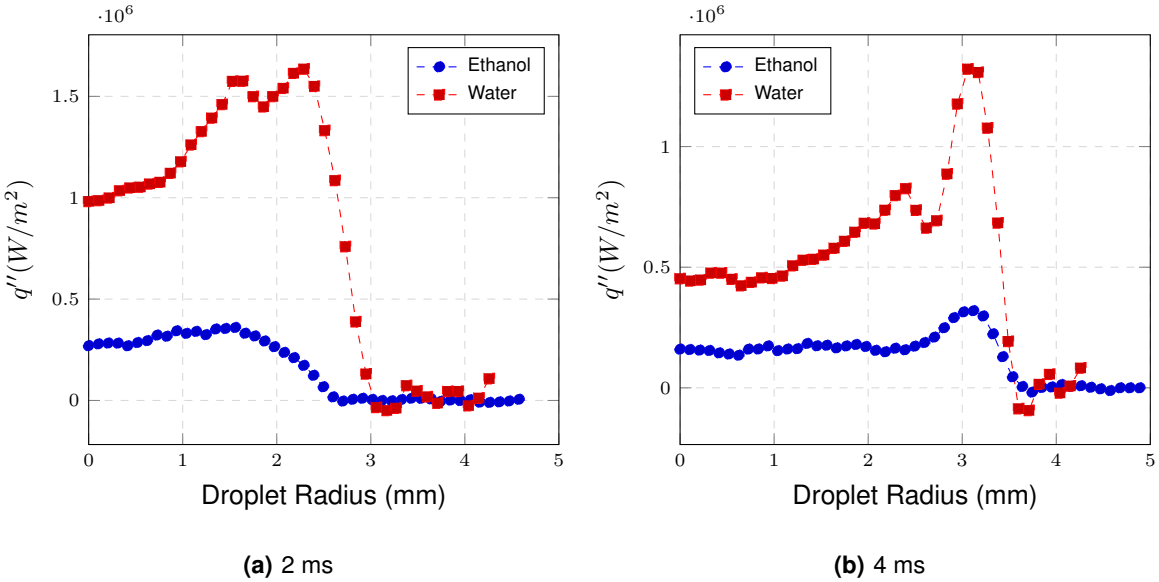


Figure 5.20: Heat Flux along the radius for Ethanol and Water for a droplet impacting at 0.8m/s on a foil initially with $\Delta T = 20^\circ C$ under saturation

diameter and thermal properties. The obtained results are depicted in Figure 5.21. The results for the ethanol experiment show a better cooling effectiveness. This may seem odd looking at the flux values, which are much lower for ethanol. However, considering the definition of the cooling effectiveness, the total heat removed is divided by the maximum possible heat removed. Since ethanol has worse thermal properties, the maximum possible heat removed is also lower than that of water, so at the end the cooling effectiveness considering the improved wetted area is actually higher for ethanol. One can't conclude that ethanol is a better alternative to water when considering droplet cooling applications. The opposite is true and deductible from observing the heat flux and temperature variation plots. Instead what can be said regarding cooling effectiveness is that low surface tensions are related with higher effectiveness. This can be related to larger spreading and wetted area for the same impact velocity, as aforementioned.

5.3.6 Effect of extreme wetting scenarios: Hydrophilic and Super-Hydrophobic surfaces

Wettability plays a big part in interface phenomena, and its effects on heat transfer can also be studied by IR thermography. With this in mind, several stainless steel foils were cleaned and coated to become super-hydrophobic in order to apply the developed techniques to different wettability surfaces. A comparison between the physical phenomena in the different droplet impact phases is shown in Figure 5.22. The main difference between this comparison and the latter two is that instead of having an equilibrium phase, the droplet rebounds off the surface. Initially, the evolution looks similar, but in the timestep of 6ms, while the droplet is already receding in the super-hydrophobic, in the hydrophilic surface, it's reaching its maximum diameter. In terms of droplet impact related phenomena, we can see that the lamella also forms a rim near the contact edge, but quickly disappears.

Figure 5.23 compares the spreading factor of a water droplet impacting on a hydrophilic and super-

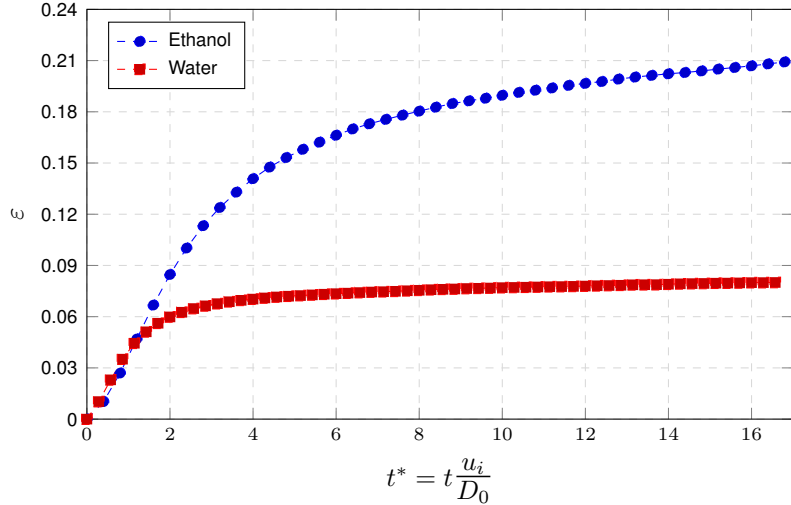


Figure 5.21: Cooling Effectiveness comparison between water and ethanol for a droplet impacting at 0.8m/s on a foil initially with $\Delta T = 20^\circ C$ under saturation

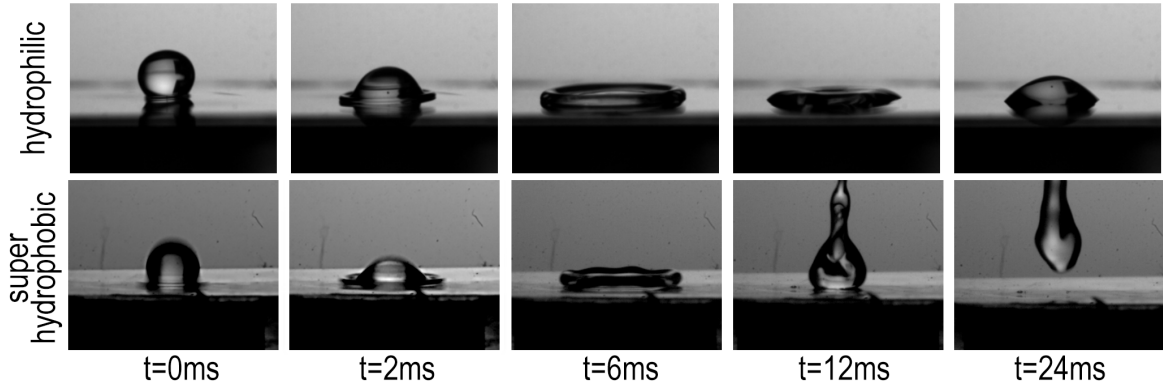


Figure 5.22: HS Images for Hydrophilic and Super-Hydrophobic surfaces droplet impact at 0.8 m/s impact speed

hydrophobic surface. The spreading factor is similar for both surfaces until reaching the maximum diameter (5 ms after impact).

However while in the hydrophilic surface the droplet recoils remaining in surface, in the super-hydrophobic foil the droplet fully rebounds from the surface (20 ms after impact). The wetted area is always larger in the droplet spreading on the hydrophilic surface, as described in Chapter 2.

Looking now at the temperature field for the initial temperature of $100^\circ C$, depicted in Figure 5.24, one can better draw conclusions about heat transfer phenomena. It is clear from the figure, that the droplet impacting on the super-hydrophobic surface removes less heat, as both the temperature drop and spreading diameter are smaller in the super-hydrophobic surface case. In the center of the droplet, a large slope is nonetheless observable in the center in the super-hydrophobic surface. This is caused by the way the droplet leaves the surface, as all liquid is concentrated in a small radius. Note that the wetted area radius is also smaller. There is no apparent temperature effect of the formed lamella rim, and some unusual curves appear near the droplet center. These phenomena can only be

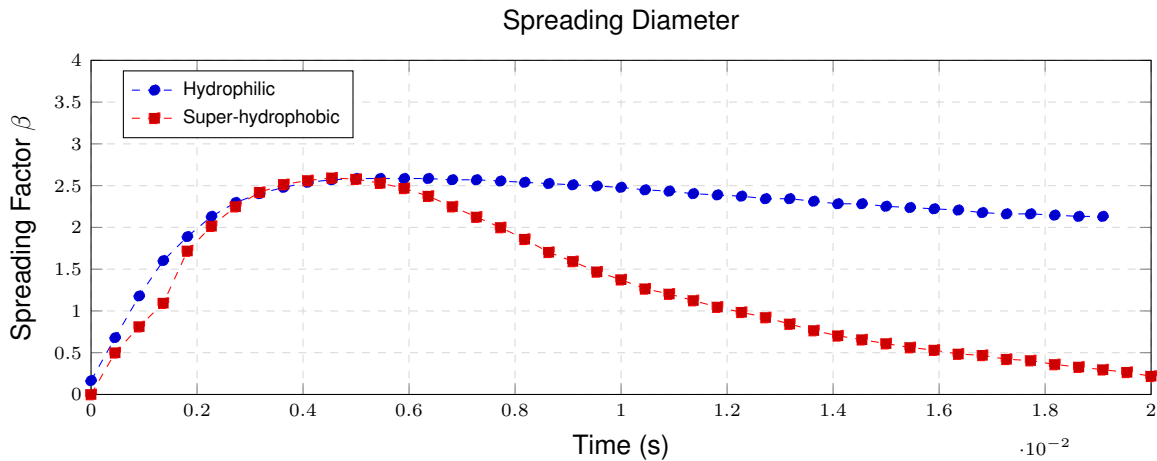


Figure 5.23: Spreading Factor along the radius for an Hydrophilic and Super-Hydrophobic

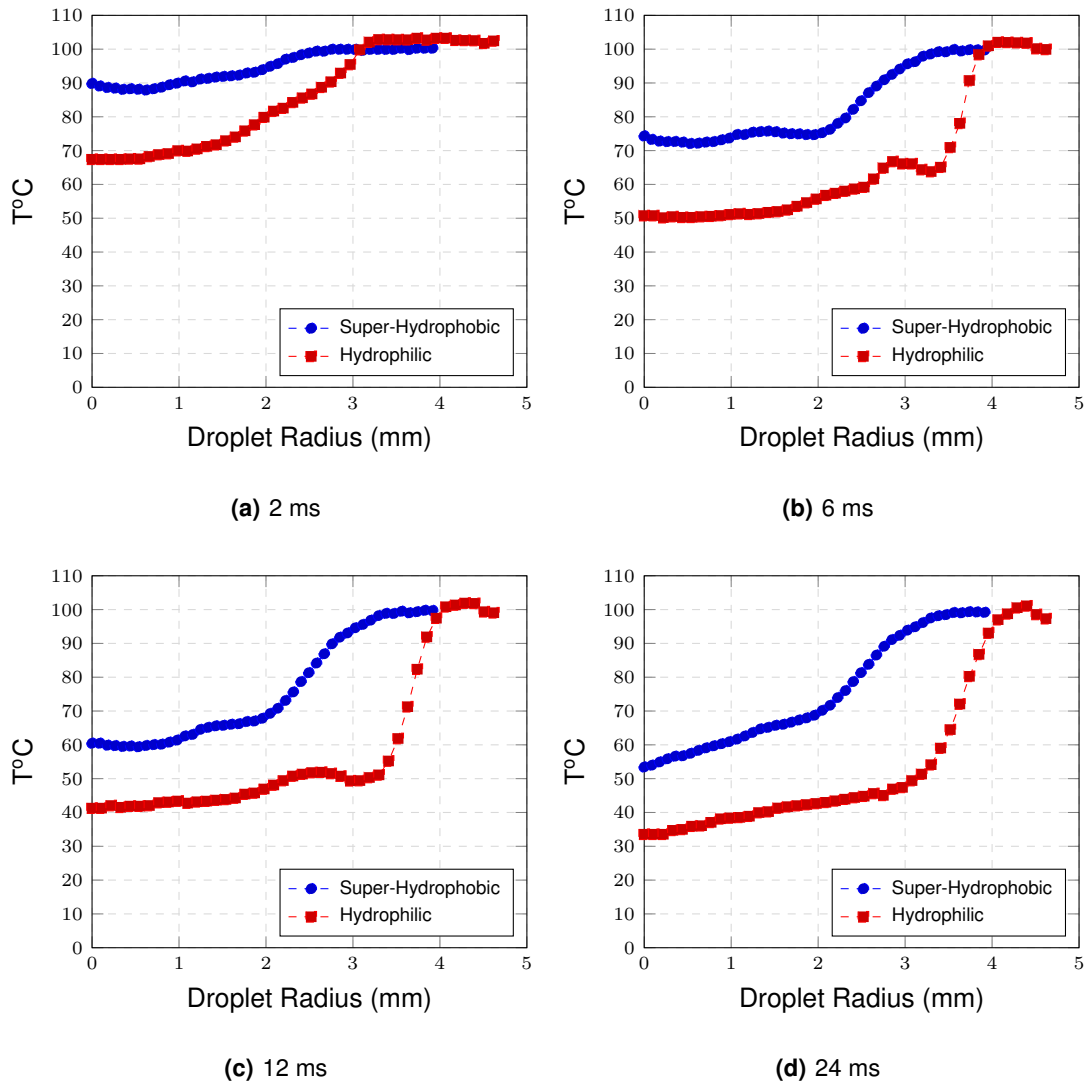


Figure 5.24: Temperature along the radius for Ethanol and Water

analyzed with the help of the images that one can obtain from the developed code. These images are shown in Figure 5.24. In the 6ms panel one can barely see the rim, but it's still visible. The colormap

for these images was shortened in order to improve the contrast, or else the lamella's rim wouldn't be visible at all. There are also some unusual spots in the image. The cause of this is the fact that, after some tests the foil's coating gets uneven and the droplet shape is affected. In the first tests this didn't happen, and the shape was more uniform. The IR Images for the first experiment can be seen in Figure 5.26. This means that the foil requires a new coating after some tests. The results for the initial temperature of 100°C are not invalidated but have should have a slightly higher heat flux than normal. The heat flux is slightly higher than expected which may be due to the aging of the surface coating

Moving on to the heat flux plots, depicted in Figure 5.27. The heat flux is considerably smaller for the super-hydrophobic surface. The heat flux peaks at the contact edge are also smaller. This is representative of a high contact angle as the liquid in the edge is above the surface but not touching it. There is a small peak in the 4 ms plot that's caused by the fact that the droplet is reaching maximum diameter as stated before. This peak is still relatively smaller to the center heat flux in the super-hydrophobic surface test. The flux at the center is very similar between both cases in this same timestep. The cause of this is related to the thickness of the droplet. The thickness is higher in the studied case, so it's expected to remove more heat. This heat flux, as stated before is also expected to be a bit higher than expected. What can also be seen is the apparently smaller diameter. This is explained by the high contact angle, as stated before.

The cooling effectiveness will describe what kind of surface is easier to cool with droplets. The comparison between both surfaces is shown in Figure 5.28. This parameter shows considerably lower values for the super-hydrophobic surface. After some timesteps, the cooling effectiveness stabilizes. This occurs because the droplet leaves the surface. From that point on there is no more heat removal, while in the hydrophilic surface, the droplet continues to remove heat. Hence the bad cooling performance obtained when using a super hydrophobic surface is not just caused by the reduced wetting area, but also due to the smaller time interval in which the droplet contacts the surface.

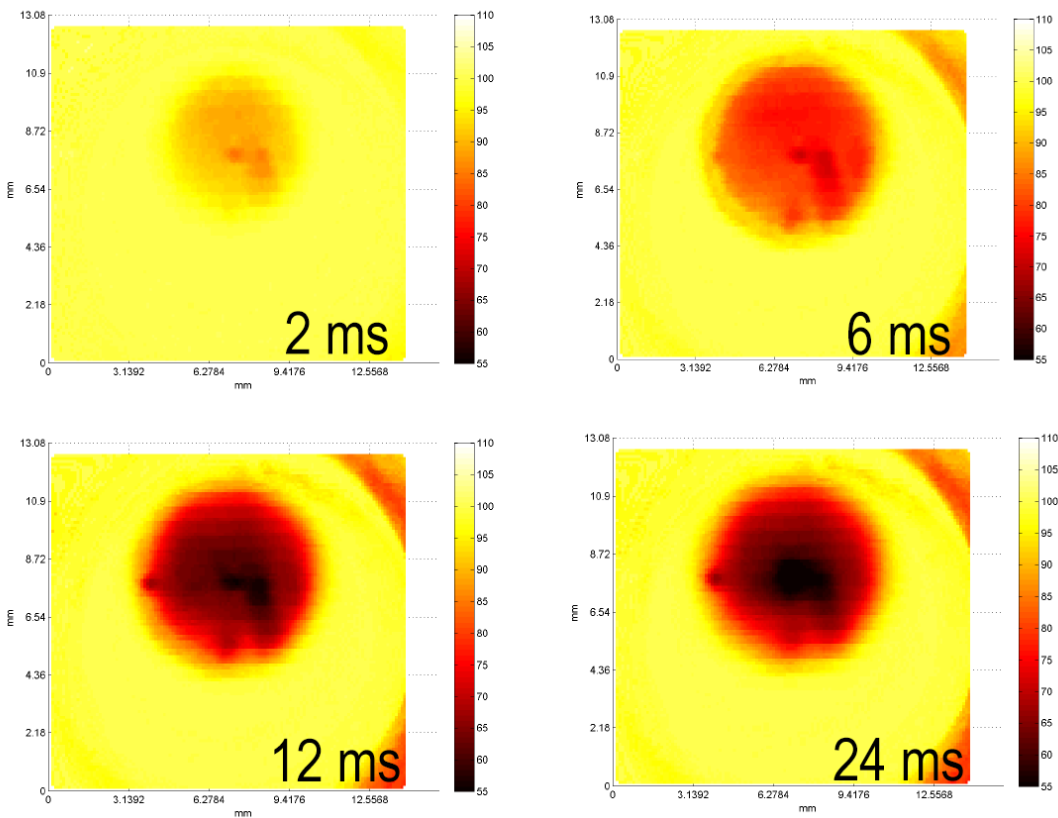


Figure 5.25: IR Images for a Super-Hydrophobic surface droplet impact at 0.8 m/s impact speed (foil initial temperature at 100°C)

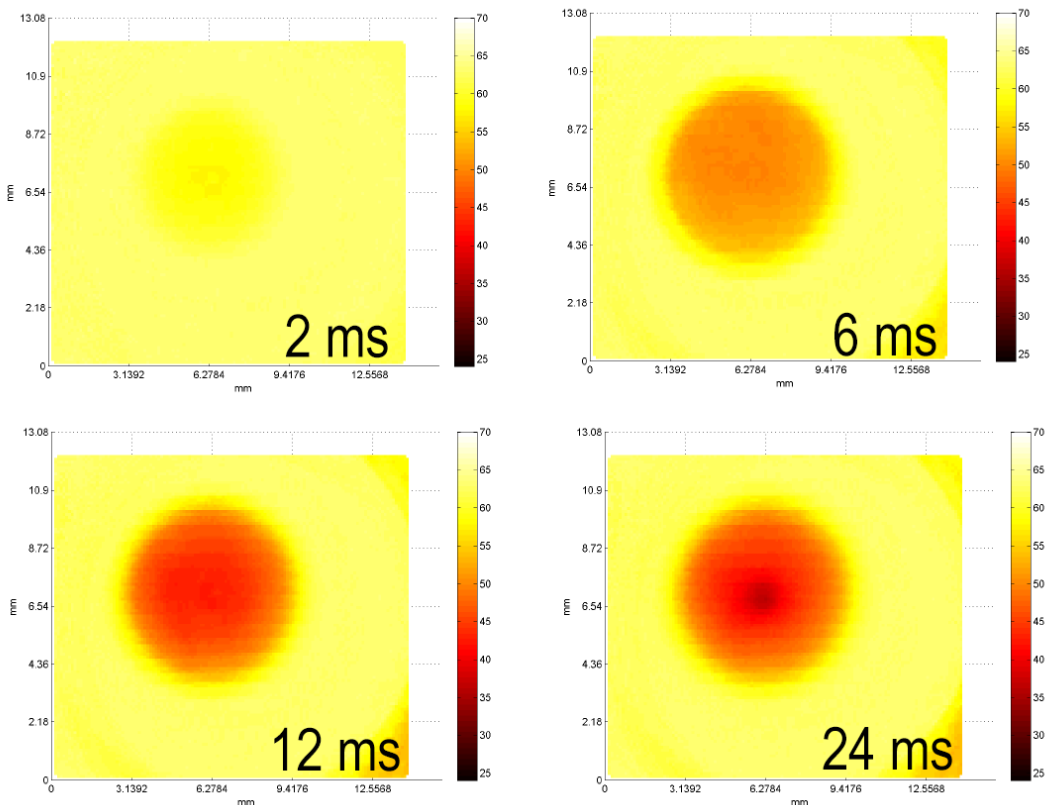


Figure 5.26: IR Images for a Super-Hydrophobic surface droplet impact at 0.8 m/s impact speed (foil initial temperature at 100°C)

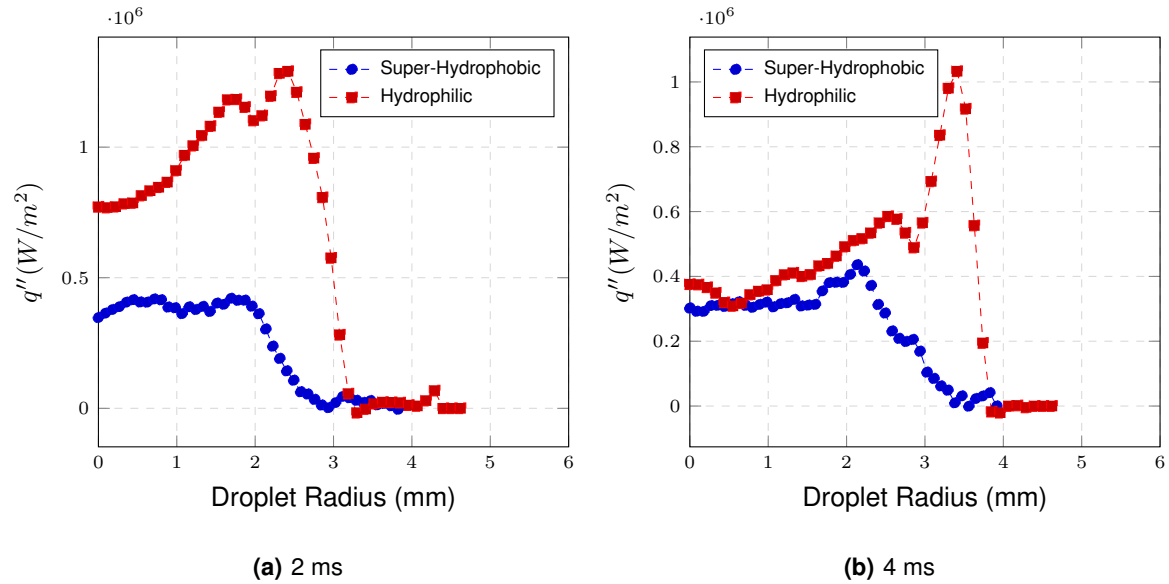


Figure 5.27: Heat Flux comparison along the radius for a droplet impact in surfaces with different wettability

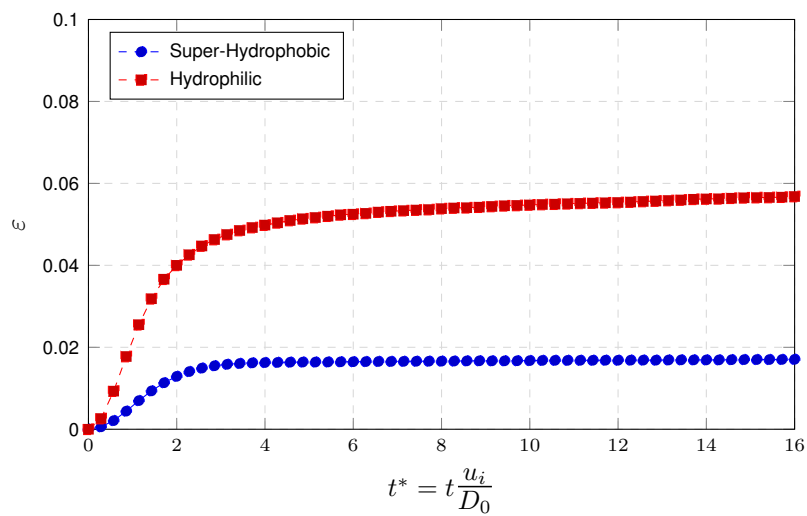


Figure 5.28: Cooling Effectiveness comparison along the radius for a droplet impact in surfaces with different wettability

6 | Conclusions and Future Work

This work aimed at exploring the potential to use time resolve infrared (IR) thermography to detail the heat transfer phenomena occurring at liquid-solid interfaces. The main focus was put on liquid droplets impacting on solid heated surfaces.

In this work, IR, namely thin (20microns) stainless steel foils.

The precision required to obtain accurate measurements within this technique applied to such demanding experimental conditions required developing a custom made calibration method and specific post processing procedures, the latter allowing to collect and process data to obtain reliable qualitative and quantitative results describing the most relevant heat transfer phenomena.

Despite this was the first approach to such a complex problem, the calibration method proved to be functional, allowing to obtain high (temporal) resolution results with noise reduction, when compared to the calibration method available in the software of the camera. This method was proved to be repeatable and the results were quite reproducible, capturing details on the temperature variation, heat flux and cooling effectiveness, in agreement with the physical processes that are described in the literature. Such details included for instance capturing the higher surface temperature observed at the center of the droplet (in the impact region) which can be related with the air entrapment mechanisms that are often referred in the literature, or the temperature variations along the droplet wetted area, which depends on the thickness of the lamella (e.g. one can identify the so called neck of the lamella).

Furthermore, IR thermal images were taken simultaneously to those obtained with a high speed camera to better understand the relation between the heat transfer processes and droplet dynamics. This approach requires some improvements as the images taken by each camera are not perfectly synchronized and similarity between frames is not always enough to achieve a precise matching between the images in early timesteps after droplet impact. In fact in the images taken within these early timesteps, the calculated heat flux depicts some irregularities caused by the lack of spatial and temporal resolution (and absent of this synchronism). This can also be caused by the thermal inertia of the stainless steel foil that is used as an impact surface. , that doesn't capture correctly the first heat transfer events's details. The ideal situation is to put the IR camera and HS camera working simultaneously. An alternative to the stainless steel foil that can be used in future experiments is a sapphire glass, transparent to infrared, and painted with a high emissivity paint.

After validating the calibration and post processing methods, infrared thermography was used to infer on the effect of the droplet impact velocity, on the liquid properties (particulalry the surface tension) and on the effect of the wettability of the surface (applying a commercial chemical coating to the foil which turn it to superhydrophobic) on droplet dynamics and on the heat transfer processes, mainly evaluating the surface temperature variation along the droplet radius, the heat flux and the cooling effectiveness. results were also satisfactory and complied with the expected. The results show that higher impact velocity velocities lead to larger heat fluxes and cooling effectiveness. It is also shown that the temperature drop in the surface region beneath the droplet is lower for smaller impact velocities. for lower impact velocities, the temperature would drop lower. This is however only observed for later timesteps after droplet impact (later stages of spreading) and does not affect the overall cooling effectiveness.

Regarding the effect of the initial surface temperature the experimental results show that the relative temperature (initial non-dimensional temperature) plots are very close irrespective to the initial temperature considered. A similar trend is observed for the cooling effectiveness. This confirms the usefulness of the weighted background removal code, as this code is based on the fact that the temperature difference is relative and not absolute as a normal background removal would addressed it. Testing liquids with different different surface tension values, namely water and ethanol showed that contarily to what was expected the liquid with smaller surface tension which is also the liquid depicting lower thermal properties actually has a better cooling effectiveness, which is associated to the larger wetting area of this droplets during spreading. One of the main difficulties of using a low surface tension liquid turned out to be the positioning of the droplet. With the electric current the foil would slightly bend, and that was enough to influence the physics of the droplet impact. A solution to address this problem is to glue the stainless steel foil to the support glass.

Finally the wettability is shown to play a major role in droplet dynamics and heat transfer. Droplet impacts on hydrophilic surfaces were shown to remove larger heat fluxes than those impacting on superhydrophobic surfaces. The spreading diameter was close in both cases for the same velocity, but the wetted area is smaller for the superhydrophobic, as well as the time the droplet is in contact with the surface.

Part of this work was submitted to the Journal of Bionic Engineering:
Teodori, E., Moita, A. S., Pontes, P., Moura, M., Moreira, A. L. N., Y. Bai, X. Li, Y. Liu (2016) Application of bioinspired superhydrophobic surfaces in two-phase heat transfer experiments.

6.1 Future Work

In the future this one intends to extend this technique, with the devised post processing methods to address other interfacial phenomena such as bubble nucleation and growth in pool boiling. When investigating pool boiling, a new calibration must be performed. In future work, a method should also

be considered to obtain perfectly synchronized IR and high-speed images.

Improvements can also be made to the calibration. The blackbody device used to perform the calibration requires an additional cooling mechanism. This will allow working with the device up to higher temperatures and reducing the time required for the temperatures to stabilize.

The post processing code can also be improved as it's currently very fragmented and the output of the results is a simple text document with all the values. A full report with both values and plots would be of great utility for future studies. To address the fragmentation of the code, this must be optimized for an efficient and automated analysis. The calibration code is also very slow when processing data, as it must solve an equation of third order. While MATLAB takes several minutes to process a video, the camera software does it immediately. With a linearization this code may be faster.

Finally, a more efficient way to fix the stainless steel foil needs to be designed. This will prevent the deformation caused by the electric current. There is a considerable temporal temperature gradient in the foil probably due to thermal inertia. This needs to be addressed as well in future works. A possible solution to minimize this problem is better insulating the foil from its base.

Bibliography

- [1] *The Ultimate Infrared Handbook for RD Professionals*. FLIR Systems Inc, 2012.
- [2] Global Digital Central, Thermal-Fluids Central. www.thermalfluidscentral.org, accessed in May 2015.
- [3] BHUSHAN, B., AND JUNG, Y. C. Natural and biomimetic artificial surfaces for superhydrophobicity, self-cleaning, low adhesion, and drag reduction. *Progress in Materials Science* 56, 1 (2011), 1–108.
- [4] CASSIE, A., AND BAXTER, S. Wettability of porous surfaces. *Transactions of the Faraday Society* 40 (1944), 546–551.
- [5] CHOI, C., AND KIM, M. *Wettability Effects on Heat Transfer*. INTECH Open Access Publisher, 2011.
- [6] CZYSZ, P., AND DIXON, P. Quantitative Heat Transfer Measurement Using Thermographic Phosphors Using Thermographic. *S.P.I.E. Journal* 7 (1969), 77–79.
- [7] DESK, E. C. Electronic warfare and radar systems engineering handbook.
- [8] DEWITT, D. P., AND NUTTER, G. D. *Theory and Practice of Radiation Thermometry*. John Wiley & Sons, Inc., 1988.
- [9] DUAN, X., PHILLIPS, B., MCKRELL, T., AND BUONGIORNO, J. Synchronized high-speed video, infrared thermometry, and particle image velocimetry data for validation of interface-tracking simulations of nucleate boiling phenomena. *Experimental Heat Transfer* 26, 2-3 (2013), 169–197.
- [10] GERARDI, C., BUONGIORNO, J., Hu, L. W., AND MCKRELL, T. Experimental observation of the dynamic micro- and macro-layer during pool boiling. *Proceedings of 2008 ASME Summer Heat Transfer Conference HT2008, August 10- 14, 2008, Jacksonville, Florida USA* (2008).
- [11] GIRARD, F., ANTONI, M., AND SEFIANE, K. Infrared thermography investigation of an evaporating sessile water droplet on heated substrates. *Langmuir* 26, 7 (2010), 4576–4580.
- [12] HARTMANN, J., HOLLANDT, J., KHLEVNOY, B., MOROZOVA, S., OGAREV, S., AND SAKUMA, F. Blackbody and other calibration sources. *Experimental Methods in the Physical Sciences* 42 (2009), 241–295.

- [13] HEALY, W., HARTLEY, J., AND ABDEL-KHALIK, S. On the validity of the adiabatic spreading assumption in droplet impact cooling. *International Journal of Heat and Mass Transfer* 44, 20 (2001), 3869–3881.
- [14] KATO, M., TANAKA, A., SASAGAWA, M., AND ADACHI, H. Durable automotive windshield coating and the use thereof, Oct. 25 2011. US Patent 8,043,421.
- [15] KIM, H., AND BUONGIORNO, J. Detection of liquid–vapor–solid triple contact line in two-phase heat transfer phenomena using high-speed infrared thermometry. *International Journal of Multiphase Flow* 37, 2 (2011), 166–172.
- [16] KOCH, K., AND BARTHLOTT, W. Superhydrophobic and superhydrophilic plant surfaces: an inspiration for biomimetic materials. *Philosophical Transactions of the Royal Society of London A: Mathematical, Physical and Engineering Sciences* 367, 1893 (2009), 1487–1509.
- [17] MOITA, A., AND MOREIRA, A. Drop impacts onto cold and heated rigid surfaces: morphological comparisons, disintegration limits and secondary atomization. *International Journal of Heat and Fluid Flow* 28, 4 (2007), 735–752.
- [18] MOITA, A. S., LAURÉNCIA, C., RAMOS, J. A., PRAZERES, D. M. F., AND MOREIRA, A. L. N. Dynamics of droplets of biological fluids on smooth superhydrophobic surfaces under electrostatic actuation. *Journal of Bionic Engineering* 13, 2 (2016), 220–234.
- [19] PASANDIDEH-FARD, M., AZIZ, S., CHANDRA, S., AND MOSTAGHIMI, J. Cooling effectiveness of a water drop impinging on a hot surface. *International journal of heat and fluid flow* 22, 2 (2001), 201–210.
- [20] REIN, M. Phenomena of liquid drop impact on solid and liquid surfaces. *Fluid Dynamics Research* 12, 2 (1993), 61.
- [21] SARGENT, S. R., HEDLUND, C. R., AND LIGRANI, P. M. An infrared thermography imaging system for convective heat transfer measurements in complex flows. *Measurement Science and Technology* 9 (1998), 1974–1978.
- [22] SCHWABE, D., ZEBIB, A., AND SIM, B.-c. Oscillatory thermocapillary convection in open cylindrical annuli. part 1. experiments under microgravity. *Journal of Fluid Mechanics* 491 (2003), 239–258.
- [23] SHEN, J., GRABER, C., LIBURDY, J., PENCE, D., AND NARAYANAN, V. Simultaneous droplet impingement dynamics and heat transfer on nano-structured surfaces. *Experimental Thermal and Fluid Science* 34, 4 (2010), 496–503.
- [24] SIELAFF, A. Experimental investigation of single bubbles and bubble interactions in nucleate boiling. *Unpublished Doctoral Dissertation TU Darmstadt* (2014).

- [25] STROLOS, G., ALEKSIS, G., GAVAISES, M., NIKAS, K.-S., NIKOLOPOULOS, N., AND THEODORAKAKOS, A. Non-dimensionalisation parameters for predicting the cooling effectiveness of droplets impinging on moderate temperature solid surfaces. *International Journal of Thermal Sciences* 50, 5 (2011), 698–711.
- [26] TARTARINI, P., CORTICELLI, M., AND TAROZZI, L. Dropwise cooling: experimental tests by infrared thermography and numerical simulations. *Applied Thermal Engineering* 29, 7 (2009), 1391–1397.
- [27] WENZEL, R. N. Resistance of solid surfaces to wetting by water. *Industrial & Engineering Chemistry* 28, 8 (1936), 988–994.
- [28] YOUNG, T. An essay on the cohesion of fluids. *Philosophical Transactions of the Royal Society of London* 95 (1805), 65–87.

A | MATLAB function: calibration.mat

```
1 function vid=calibration(vid)
2
3 L=size(vid); %extrai tamanho da matriz do video
4 x=600; %inicializacao do valor
5 Tamb=24; %temperatura ambiente
6 e=0.95; %emissividade estimada
7
8 for k=1:L(3)
9     for j=1:L(2)
10        for i=1:L(1)
11            ADU = vid(i,j,k);
12            %seguranca para excluir pixeis mortos
13            if ADU < 1000
14                vid(i,j,k) = 450;
15            else
16                %encontra Wtot para ADU de cada pixel
17                r=roots([-1.4901E-6 8.4705E-3 -3.268533 1574.11-ADU]);
18                l=1;
19                %filtra solucoes
20                while l<4
21                    fi=r(l);
22                    if fi >=300 && fi <=1500
23                        x = fi ;
24                    end
25                    l=l+1;
26                end
27            end
28            vid(i,j,k)=(nthroot((x/5.67E-8-0.05*(Tamb+273)^4)/e,4)-273);
29        end
30    end
31    k
32 end
```

B | MATLAB function: pbkgremove.mat

```
1 function vid = bkgremove(vid)
2
3 % Initializes variables
4 L = size(vid);
5 frames = L(3);
6 bkg = vid(:,:,1);
7 sum = 0;
8 aux = 0;
9
10 %% Identifies the plate hole
11 [centers, radii] = imfindcircles(im2bw(imread('frame-1.tif')),0.3),[45 47] ...
12 , 'ObjectPolarity','bright','Sensitivity',0.992);
13
14 %% Calculates the average
15 for i=1:L(1)
16     for j=1:L(2)
17         if sqrt((i-centers(1))^2+(j-centers(2))^2)>(radii -30)
18             else
19                 sum=vid(i,j,1)+sum; aux=aux+1;
20             end
21         end
22     end
23
24 av=sum/aux
25
26 %% Subtract background fraction
27 for t=1:frames
28     for x=1:L(1)
29         for y=1:L(2)
30             vid(x,y,t) = av-(bkg(x,y)-vid(x,y,t))/bkg(x,y)*av;
31         end
32     end
33 end
```

C | MATLAB function: fluxo.mat

```
1 load results.mat
2 mat=results
3 %% Variables
4 cp=477; %J.kg-1.K-1
5 k=18; %W.m-1.K-1
6 th=20*10^-6; %m
7 rho=7880; %kg.m-3
8 qi=2548; %W.m-2
9 dx=110*10^-6; %m
10 dt=10^-3; %s
11 slimit=60; %space size
12 tlimit=60; % time size
13
14
15 %% Initialization
16 q=zeros(tlimit ,slimit );
17 space=zeros(tlimit ,slimit );
18 time=zeros(tlimit ,slimit );
19
20 %% Coeficients
21 a1=0; a2=-1; a3=1; a4=0; a5=0;
22
23 %% Calculation
24 for i=3:slimit
25     for t=1:tlimit
26         if t==1
27             A1=0; A2=0; A3=mat(t ,i )*a3; A4=mat(t+1,i )*a4; A5=mat(t+2,i )*a5 ;
28         elseif t==2
29             A1=0; A2=mat(t-1,i )*a2; A3=mat(t ,i )*a3 ;A4=mat(t+1,i )*a4;
30             A5=mat(t+2,i )*a5 ;
31         else
32             A1=mat(t-2,i )*a1; A2=mat(t-1,i )*a2; A3=mat(t ,i )*a3;
33             A4=mat(t+1,i )*a4; A5=mat(t+2,i )*a5 ;
34         end
35
36         if i==1 || t==1
37             q(t ,i )=0;
38         elseif i==2
39             q(t ,i )=0;
40         else
41             space(t ,i )=k*th *(mat(t ,i )-2*mat(t ,i -1)+mat(t ,i -2))/dx ^2;
42             time(t ,i )=-rho*cp*th *(A1+A2+A3+A4)/ dt ;
43             q(t ,i )=qi+time(t ,i )+space(t ,i );
44         end
45     end
46 end
```

D | MATLAB function: fluxo.mat

```
1 % Initialization (variables from fluxo.mat)
2 L=size(q);
3 tsize=L(1);
4 Q=zeros(1,tsize );
5 Qtot=Q;
6
7 for t=1:tsize
8     for i=1:L(2)-2
9         Q(t)=((q(t,i+1)+q(t,i))*(i-1/2)/2-
10            (q(t,i+2)+q(t,i+1))/2+(q(t,i+1)+q(t,i))/2)*dx^2*2*pi ()+Q(t);
11     end
12 end
13
14 raio=(0.11:0.11:0.11*40);
15 tempo=(10^-3:10^-3:60*10^-3);
16
17 for tt=2:tsize-1
18     for t=1:tt
19         Qtot(tt)=(Q(t+1)+Q(t))*dt/2+Qtot(tt);
20     end
21 end
22
23 e=Qtot/(1000*4/3*pi()*0.0015^3*4182*(100-24));
24
25 t1=tempo*2/0.0027;
26
27 plot(t1,e,'b');
```
